FEDERAL UNIVERSITY OF SÃO CARLOS
CENTER FOR EXACT SCIENCES AND TECHNOLOGY
POSTGRADUATE PROGRAM IN CIVIL ENGINEERING

ANDRÉ VITOR BENEDITO

FLEXURAL BEHAVIOR OF CORRODED STEEL BEAMS WITH AND WITHOUT WEB OPENINGS: EXPERIMENTAL, ANALYTICAL, AND NUMERICAL INVESTIGATION

São Carlos - SP
2026

ANDRÉ VITOR BENEDITO

FLEXURAL BEHAVIOR OF CORRODED STEEL BEAMS WITH AND WITHOUT WEB OPENINGS: EXPERIMENTAL, ANALYTICAL, AND NUMERICAL INVESTIGATION

A thesis submitted to the Faculty of Postgraduate Studies in fulfillment of the requirements for the defense of the Doctor of Philosophy degree in Civil Engineering.

Advisor: Carlos Humberto Martins

Co-advisor: Pablo Augusto Krahl

São Carlos - SP
2026

UNIVERSIDADE FEDERAL DE SÃO CARLOS

Centro de Ciências Exatas e de Tecnologia
Programa de Pós-Graduação em Engenharia Civil

Folha de Aprovação

Defesa de Tese de Doutorado do candidato André Vitor Benedito, realizada em 24/04/2026.

Comissão Julgadora:

Prof. Dr. Carlos Humberto Martins (UFSCar)

Prof. Dr. Emerson Alexandro Boladim (UNESP)

Prof. Dr. Gustavo de Miranda Saleme Gidrão (UTFPR)

Prof. Dra. Monique Cordeiro Rodrigues (UERJ)

Prof. Dr. José Julio de Cerqueira Pituba (UFCAT)

O Relatório de Defesa assinado pelos membros da Comissão Julgadora encontra-se arquivado junto ao Programa de Pós-Graduação em Engenharia Civil.

ACKNOWLEDGEMENTS

First and foremost, I thank God, whose sustaining grace upheld me when I could no longer stand on my own and who remained by my side through the most difficult moments of my life.

To my beloved family, my mother, Suely Dalabilia, my father, José Benedito, and my brother, Tiago Benedito, I offer my deepest gratitude for your unconditional love, constant prayers, and unwavering support. Your strength carried me forward and gave me courage in moments of hardship.

To my girlfriend, Letícia Martins de Lima, I express my heartfelt gratitude for your love, patience, and steadfast support. Your presence gave me strength in moments of doubt and encouraged me to keep moving forward through the most challenging times.

To my lifelong friends, Cassio Jandrey, Mikael Milan, and Pedro Niza, as well as to those who became family along the way, Vinicius Brother and Vinicius Moura, I am sincerely grateful for your friendship and support. I also remember with special affection the friends I made in London, Arthur, Sebastian, Luiza, and Patrick, whose presence transformed a foreign land into a home.

To my co-advisor, Prof. Pablo Krahl, I express my deepest gratitude for your encouragement, for a friendship that extended beyond academic boundaries, and for believing in me even when I doubted myself. Your support was essential throughout this journey. To my advisor, Prof. Carlos Humberto Martins, I am profoundly grateful for your trust, patient guidance, and continuous support.

My sincere gratitude also extends to the laboratory technicians at PUC-Rio, Euclides, Jhansen, Rogério, and Marques, for their invaluable assistance during the long experimental days that made this research possible. I also wish to acknowledge Prof. Rabee Shamass, Prof. Flávio Silva, and Prof. Daniel Cardoso for their valuable contributions to this work.

Finally, I am grateful to the companies that contributed to this research: Gerdau, for providing the steel materials, and Metalfenas, for their support.

This study was financed in part by the Coordenação de Aperfeiçoamento de Pessoal de Nível Superior, Brasil (CAPES), Finance Code 001. Additional financial support was provided by the Brazilian National Council for Scientific and Technological Development (CNPq) under Projects No. 408498/2022-6 and No. 421785/2022-5.

ABSTRACT

Corrosion is one of the most critical deterioration mechanisms affecting steel structures, since it reduces plate thickness, modifies geometric and mechanical properties, and may lead to instability, thereby compromising structural safety and load-carrying capacity. In steel beams, especially castellated beams, comprehensive studies that address the combined effects of corrosion on flexural response and local instability mechanisms remain limited, particularly regarding web-post buckling. In this context, this thesis investigates the flexural behavior of corroded steel beams with and without web openings through experimental, analytical, and numerical approaches, considering ASTM A572 Grade 50 and Grade 60 steels. The experimental program comprised tensile tests on coupons extracted from the steel profiles, three-point bending tests on solid-web and castellated beams under both corroded and uncorroded conditions, and Digital Image Correlation analyses to characterize surface imperfections, lateral displacements, and strain fields. The results showed that, in corroded solid-web beams, corrosion promoted local buckling before full cross-sectional yielding, thus changing the governing resistance mechanism. In castellated beams, corrosion significantly increased susceptibility to web-post buckling, leading to substantial reductions in load-carrying capacity of 39.05% for Grade 50 steel and 35.85% for Grade 60 steel, while the steel grade itself had no significant influence on the overall web-post buckling mode. DIC analyses further revealed localized strain concentrations around corrosion pits and earlier yielding in the tensile tie region of the web-post. Pit-depth measurements were statistically described by a log-normal distribution, with logarithmic mean and standard deviation values of 0.7951 mm and 0.3865 mm for Grade 50 steel, and 0.8918 mm and 0.4636 mm for Grade 60 steel. Based on experimental evidence, a non-empirical analytical formulation was proposed to estimate the critical load associated with web-post buckling in both corroded and uncorroded castellated beams. Compared with Steel Design Guide 31 and EN 1993-1-13:2024, the proposed model provided closer agreement with the experimental results, with lower average deviations than the code-based approaches. In parallel, a finite element model was developed in ABAQUS using a stochastic representation of corrosion based on a spatially correlated Gaussian random field. The calibration process indicated that a 15 mm mesh and a spatial correlation factor of $\rho_f = 0.75$ yielded the best agreement with the experimental load-displacement curves and successfully reproduced the corrosion-induced shift in structural behavior. Overall, the thesis advances the understanding of corrosion effects on the flexural and instability behavior of steel beams and provides analytical and numerical tools for the assessment of corroded castellated members.

Keywords: pitting corrosion; steel beams; castellated beams; web-post buckling; flexure; numerical modeling.

RESUMO

A corrosão é um dos principais mecanismos de deterioração de estruturas de aço, pois reduz a espessura dos elementos, altera propriedades geométricas e mecânicas e pode antecipar modos de instabilidade, comprometendo a segurança e a capacidade resistente. No caso de vigas de aço, sobretudo vigas casteladas, ainda são escassos os estudos que investigam de forma integrada os efeitos da corrosão sobre a resposta à flexão e sobre os mecanismos de instabilidade local, em especial a flambagem do montante da alma. Nesse contexto, esta tese investiga o comportamento flexional de vigas de aço corroídas com e sem aberturas na alma, por meio de abordagens experimental, analítica e numérica, considerando aços ASTM A572 Grau 50 e Grau 60.O programa experimental envolveu ensaios de tração em corpos de prova extraídos dos perfis, ensaios de flexão em três pontos em vigas de alma cheia e em vigas casteladas, ambas nas condições corroída e não corroída, além do uso de Correlação Digital de Imagens para caracterização de imperfeições superficiais, deslocamentos laterais e campos de deformação. Os resultados mostraram que, nas vigas de alma cheia corroídas, a corrosão promoveu a ocorrência de flambagem local antes do escoamento completo da seção, alterando o mecanismo resistente. Nas vigas casteladas, a corrosão intensificou a suscetibilidade à flambagem do montante da alma, com redução significativa da capacidade resistente, da ordem de 39,05% para o aço Grau 50 e 35,85% para o Grau 60, sem influência expressiva do grau do aço sobre o modo global de flambagem do montante. A análise por DIC indicou ainda que a corrosão provocou concentrações localizadas de deformação e antecipou o escoamento na região tracionada do montante.A profundidade dos pites foi caracterizada estatisticamente por distribuição log-normal, com média logarítmica de 0,7951 mm e desvio padrão de 0,3865 mm para o aço Grau 50, e de 0,8918mm e 0,4636mm para o Grau 60. Com base nas observações experimentais, foi proposta uma formulação analítica não empírica para estimativa da carga crítica associada à flambagem do montante da alma, válida para vigas casteladas corroídas e não corroídas. Em comparação com os procedimentos do Steel Design Guide 31 e da EN 1993-1-13:2024, o modelo proposto apresentou melhor concordância com os resultados experimentais, com desvios médios inferiores aos dos modelos normativos. Além disso, foi desenvolvido e validado um modelo numérico em ABAQUS com representação estocástica da corrosão por campo aleatório Gaussiano correlacionado. A calibração indicou melhor desempenho para malha de 15 mm e fator de correlação espacial ρ_f = 0,75, reproduzindo adequadamente as curvas força-deslocamento e a mudança de comportamento induzida pela corrosão. Assim, a tese contribui para o entendimento dos efeitos da corrosão no comportamento flexional e nos mecanismos de instabilidade de vigas de aço, além de fornecer uma base analítica e numérica para avaliação de vigas casteladas corroídas.

Palavras-chave: corrosão por pites; vigas de aço; vigas casteladas; flambagem do montante da alma; flexão; modelagem numérica.

Flexural behavior of corroded steel beams with and without web openings: experimental, analytical, and numerical investigation.

LIST OF FIGURES

LIST OF TABLES

LIST OF PUBLICATIONS

Throughout the doctoral research, several studies were developed and published in peer-reviewed journals:

1. Benedito, A. V, Krahl, P. A., Santos V. B., Oliveira V. M., Rossi A., Silva F. A., Cardoso D. C. T., Martins, C. H. (2026) *Experimental analysis and a new model to predict web-post buckling of corroded anglo-saxon castellated beams*. ***Thin-walled Structures.*** 221, 114417. https://doi.org/10.1016/j.tws.2025.114417

2. Benedito, A. V., Benedetty Torres, C. A., Silva, R. M. C.; Krahl, P. A., Cardoso, D. C.T., Silva, F. A. & Martins, C. H. (2024). *Effects of Niobium Addition on the Mechanical Properties and Corrosion Resistance of Microalloyed Steels: A Review* ***Buildings***, 14(5), 1462. https://doi.org/10.3390/buildings14051462.

3. Benedito, A. V., Vanalli, L., Krahl, P. A., Martins, C. H., Rossi, A., & Silva, F. A. (2024). *A modeling strategy for the shear and flexural performance prediction of SFRC beams without stirrups accounting for the variability of properties*. ***Structural Concrete***. https://doi.org/10.1002/suco.202300779.

4. Benedito, A. V., Milani, M. F. P., Krahl, P. A., Bianchi, B. M., Nardin, S. & Martins, C. H. (2023). *Nonlinear finite element analysis of partially encased composite columns under non-uniform moments*. ***Structures***, 58, 105519. https://doi.org/10.1016/j.istruc.2023.105519.

5. Oliveira V. M., Santos V. B., Rossi A., **Benedito A. V**., Krahl P. A., Martins C. H., Silva F. A., Cardoso D. C. T. (2025). *Steel-UHPC composite castellated beams under hogging bending: Experimental and numerical investigation*. ***Engineering Structures***. https://doi.org/10.1016/j.engstruct.2025.120012

6. Sanvezzo, R. C., **Benedito, A. V**., Ferrari, V. J. (2024) *Comportamento de pilares de concreto retangulares reforçados por encamisamento com polímeros de fibras de carbono*. ***Ambiente Construído.*** *24, e136438.* https://doi.org/10.1590/s1678-86212024000100750

SUMMARY

CHAPTER 01 - INTRODUCTION

1.1 PROBLEM STATEMENT

Corrosion represents one of the most critical challenges affecting the durability and safety of civil infrastructure. The maintenance and rehabilitation of corroded structures impose enormous economic burdens, with global corrosion-related costs estimated at approximately 2.5 trillion USD, corresponding to about 3.4% of the world's Gross Domestic Product (GDP), while the United States alone accounts for 451.3 billion USD annually (Jafar Mazumder, 2020). Corrosion in structural components further exacerbates stability concerns due to material loss, increased slenderness, and geometric imperfections, ultimately reducing the overall load-bearing capacity. This spontaneous phenomenon leads to surface damage and changes in cross-sectional properties, accelerating structural deterioration (Benedito *et al.*, 2024; Nakai *et al.*, 2004; Nakai; Matsushita; Yamamoto, 2004, 2006; Zhang *et al.*, 2024).

Recent studies have advanced the understanding of corrosion-induced degradation and its mechanical implications for steel and reinforced concrete members. Ma et al. (Ma *et al.*, 2017) experimentally quantified the degradation of bond strength between corroded steel bars and concrete, providing insights into corrosion-induced cracking and stress redistribution. Wang et al. (Wang *et al.*, 2019) proposed an analytical model coupling prestress and corrosion effects to predict crack initiation and propagation in prestressed concrete. Ma et al. (Ma *et al.*, 2021) established a constitutive relationship for corroded steel bars extracted from fatigued concrete beams, while Ma et al. (Ma *et al.*, 2020) developed a probabilistic life-prediction model considering seasonal corrosion–fatigue interaction. These studies offer valuable frameworks for understanding corrosion mechanisms and their effects on material behavior, however, they mainly focus on reinforced or pre-stressed concrete systems.

For steel structures, which are the focus of the present study, several studies concluded that corrosion critically affects both stability and ultimate load-bearing capacity. Zhang et al. (Zhang *et al.*, 2021) showed that the reduction in flange and web thickness caused by corrosion decreases local stiffness and critical buckling load, increasing vulnerability to local and out-of-plane instability under flexure. Xiao et al. (Xiao; Chen; Peng, 2024) reported a linear deterioration in the mechanical properties of corroded specimens, including ultimate strength and elongation, leading to a three-stage constitutive model. Studies (Sheng; Xia; Ma, 2018; Xiao; Chen; Peng, 2024; Zhang *et al.*, 2021) further indicated that, beyond a certain corrosion level, buckling strength becomes lower than yield strength, causing local buckling to precede yielding and altering failure modes. Regarding global stability, (Luo *et al.*, 2022, 2024) demonstrated that corrosion reduces steel's plastic deformation capacity, as evidenced by diminished elongation, smaller lateral displacements at peak load, and premature flexural–torsional buckling, thus promoting early global instability. Under compression, Zhang et al. (Zhang *et al.*, 2020) observed that corrosion reduces thickness and introduces surface irregularities, shifting the critical buckling zone from mid-span to the ends and shortening the buckling half-wavelength by up to 48%, while Xia et al. (Xia *et al.*, 2022) found similar reductions in ultimate load and stiffness, with failure transitioning from global to local–global interactive buckling. These findings collectively indicate that corrosion strongly influences instability mechanisms, suggesting analogous degradation effects in castellated beams where web-post buckling governs the ultimate behavior.

However, few studies have investigated the behavior of corroded steel beams under flexural loading, and no research has yet addressed the response of corroded castellated beams subjected to bending. This gap is particularly critical, as both solid-web and castellated steel beams are widely employed worldwide, while no design standards currently define the structural behavior or provide analytical formulations for castellated beams affected by corrosion.

This study investigates through experimental, analytical, and numerical approaches, the behavior of corroded steel beams under flexural loading, encompassing both solid-web and castellated configurations. Two structural steels, ASTM A572 Grade 50 and Grade 60, were employed to evaluate the influence of material strength on the corrosion-induced degradation of mechanical performance. The experimental programme was designed to quantify the effects of corrosion on stiffness, load-carrying capacity, and failure modes, while the analytical and numerical models were developed to reproduce and generalize the observed behavior. The outcomes of this research are expected to contribute to a better understanding of the instability mechanisms in corroded steel beams and to support the development of predictive models and future design recommendations for castellated members exposed to aggressive environments.

1.2 JUSTIFICATION

Corrosion is one of the most significant and widespread deterioration mechanisms affecting steel structures, progressively reducing the durability, serviceability, and structural safety of members exposed to aggressive environments. Through the loss of material, changes in surface condition, and potential modification of stress distribution, corrosion can substantially alter the mechanical response of steel components over time. Although the effects of corrosion on steel materials and structural elements have been addressed in several studies, the available knowledge is still concentrated mainly on conventional members and generalized forms of degradation. In contrast, the specific effects of corrosion on the strength, stiffness, and stability behavior of steel beams, particularly castellated beams, remain insufficiently understood. This limitation is especially relevant because castellated beams present a highly optimized geometry, with web openings and slender web-post regions that make their structural response strongly dependent on local stability phenomena. As a result, corrosion-induced thickness loss may have a more severe impact on these members than on solid-web beams, particularly by intensifying instability mechanisms and accelerating the reduction in load-carrying capacity.

The importance of this topic is further reinforced by the widespread use of both solid-web and castellated steel beams in modern civil engineering structures, including industrial buildings, bridges, warehouses, and long-span floor systems, where structural efficiency and reduced self-weight are essential design advantages. Despite these practical applications, current design provisions do not adequately address the deterioration caused by corrosion in such members, particularly in relation to instability-sensitive responses. This lack of guidance represents a significant technical and scientific gap, since engineers still have limited tools to evaluate the residual performance of corroded beams or to predict how corrosion affects the transition from bending-dominated behavior to instability-controlled failure. In this context, understanding the influence of corrosion on stiffness degradation, ultimate strength, displacement response, and failure mode is fundamental for the development of reliable predictive models and for the establishment of more rational inspection, maintenance, and rehabilitation strategies.

To address this gap, the present research adopts an integrated experimental, analytical, and numerical approach, allowing the problem to be examined from a complementary perspective. The experimental investigation provides direct evidence of the structural response and failure mechanisms of corroded beams, while the analytical component contributes to the formulation of simplified predictive models capable of representing the observed behavior. In parallel, the numerical analyses enable a more detailed assessment of the role of local thickness loss, realistic pit distributions, material degradation, and geometric instability in the overall response of the members. By combining these approaches, the study seeks to provide a comprehensive understanding of how corrosion modifies the flexural and stability performance of steel beams, with particular emphasis on castellated beams. Therefore, this research is justified not only by its potential to advance the scientific understanding of corrosion effects on steel members, but also by its direct practical relevance for the future development of analytical formulations, assessment procedures, and design recommendations for castellated beams operating in aggressive environments.

1.3 OBJECTIVES

The overarching aim of this study is to conduct flexural tests on solid-web beams and castellated beams both before and after corrosion. Based on this overall aim, the following specific objectives are defined.

1) Conduct an experimental program involving flexural tests on solid-web and castellated steel beams before and after corrosion, in order to evaluate the effects of corrosion on load-carrying capacity, stiffness, displacement response, strain distribution, and failure modes;
2) Develop a Finite Element Model (FEM) using the ABAQUS program to accurately represent the behavior of uncorroded beams and the subsequent behavior of the beams after corrosion;
3) Following numerical validation, use the FEM to assess the influence of the random spatial distribution of pits and pit depths with statistical correlation.
4) Using Digital Image Correlation (DIC), determine the mean values and standard deviations of the surface imperfections on the regions analysed;
5) Develop an analytical formulation capable of predicting the failure load governed by Web-Post Buckling (WPB) in both corroded and uncorroded castellated beams.

Consequently, this study aims to enhance the understanding of corrosion effects on the flexural and instability behavior of steel beams. Additionally, the ultimate goal is to provide the technical community with an efficient analytical method for predicting the resistance of castellated beams affected by corrosion.

CHAPTER 2 - LITERATURE REVIEW

This chapter presents the scientific background that supports the present study. This chapter reviews the main studies developed to date at the structural scale, highlighting experimental, numerical, and analytical investigations on the effects of pitting corrosion on the behavior and resistance of structural members. The objective is to establish the current state of knowledge, identify the main advances and limitations in literature, and provide the basis for the development of the present research.

2.1 LITERATURE REVIEW OF BEAMS UNDER THE EFFECT OF CORROSION

Steel beams are widely used in structures, and their moment capacity is a crucial factor in determining overall structural performance. However, corrosion can diminish this capacity by reducing the cross-sectional area of the steel components, thereby weakening their bearing strength and ultimately shortening the service life of the structures (Hosseinzadeh; Kontoni; Babaei, 2023; Xin *et al.*, 2022; Zhu *et al.*, 2023). Pitting corrosion is an unavoidable issue for steel structures during their service life, characterized by localized attacks that result in the formation of small holes or pits on the metal surface (Nyby *et al.*, 2021; Pedeferri, 2018).

This type of corrosion is particularly problematic as the pits can grow quickly and penetrate deep into the material, compromising structural integrity (Bhandari *et al.*, 2015; Van Orden, 1989). The likelihood of localized corrosion, such as pitting, is strongly influenced by the chemistry of the surrounding environment, particularly the presence of aggressive anions like chloride ions. Factors that facilitate pitting corrosion include the breakdown of protective passive films, the creation of occluded cells, and the presence of impurities or inclusions in the metal (Jia *et al.*, 2009; Obeyesekere, 2017). Figure 0*1*a and

01b illustrate the effect of pitting on the web surface of the same steel beam before and after corrosion.

Figure 01 - Surface of non-corroded and corroded beam

(a) Surface of non-corroded beam (b) surface of corroded beam.

Source: The author (2026).

Corrosion, as a form of surface geometric damage, reduces the plate thickness, alters the section properties, and creates a complex corroded surface morphology. These changes can affect the plate's buckling behavior and, consequently, diminish the flexural capacity of the structural members.

In this context, the degradation of steel's mechanical properties can be analyzed using various methodologies. Generally, the literature reports more studies on small specimens. However, research on large-scale specimens, such as beams (Chen; Zhang; Yu, 2021; Kuang *et al.*, 2014; Luo *et al.*, 2022; Sheng; Xia; Ma, 2018; Tzortzinis *et al.*, 2021, 2022; Wang; Xu; Li, 2020), columns (Nie *et al.*, 2020), beam–column joints

(Wang; Huang; Zheng, 2018; Wang *et al.*, 2021; Wang; Kong; Xu, 2024; Zhang; Zheng; Zhao, 2023), and frames (Zhang; Zheng; Zhao, 2020)(Xiao *et al.*, 2021).

The techniques used to induce corrosion can be categorized by the environment in which corrosion occurs, such as indoor (Bao *et al.*, 2021) or outdoor (Zakowski *et al.*, 2014; Zhang; Zheng; Zhao, 2020; Zhu *et al.*, 2020) environments. In outdoor environments, steel is exposed to actual corrosive atmospheric conditions (Zakowski *et al.*, 2014; Zhu *et al.*, 2020). Uncorroded specimens can also be subjected to in situ corrosion conditions. For instance, Zhu et al. (2020) studied the corrosion behavior of stainless steel and Ni-alloy samples immersed in the South China Sea. Additionally, the corrosion resistance of previously corroded elements and structures can be evaluated. Tzortinis et al. (2021) examined the mechanical behavior of corroded I-beams from two steel bridges that had been in service since 1939.

The corrosion rate is another variable used to classify corrosion, which means that the corrosion can be induced naturally Tzortinis et al. (2021), as in the case of most outdoor corrosion, or induced in an accelerated process (Xiao *et al.*, 2021; Zhang; Zheng; Zhao, 2023). The outdoor natural corrosion is advantageous since it is possible to know the real steel corrosion resistance in a specific environment. However, the test duration may become excessive (Morcillo *et al.*, 2013) since corrosion is time-dependent.

According to (ISO 9223, 2012), the environments are classified into six categories based on their ability to induce corrosion in steel and other metals. Specifically, the ISO-C3 and ISO-C4 categories, defined in the standard ISO 9223, detail corrosion rates of 25–50 μm/a and 50–80 μm/a, respectively. Zhang et al.(2020) report that 18.1–36.3 years of corrosion typical of an ISO-C3 environment can be simulated by 20–120 days of accelerated corrosion using an NaCl solution spray with a concentration of 50 ± 5 g/L and a pH of 6.5–7.2. Similarly, the same conditions can simulate 11.3–18.1 years of corrosion in an ISO-C4 environment. Under laboratory conditions, the degradation process can be accelerated through several techniques, such as immersion in chloride solution, without (Ranji; Zakeri, 2011)or with an imposed electric current (electrochemical accelerated corrosion) (Chen; Jiang; Jin, 2014; Peng *et al.*, 2019), immersion in an acid solution (sulfuric) (Nam; Kim, 2010), and exposure to salt spray through cabinets (Zhang; Zheng; Zhao, 2023). Although the accelerated corrosion tests do not reproduce the real conditions of the corrosive atmosphere, they allow for an evaluation of the corrosion resistance in a short time (Dražić; Vaŝĉiẑ, 1989).

As corrosion damage progresses, the depth distribution of the pits widens. Moreover, the variation in cross-sectional area can affect the beam's slenderness ratio, potentially altering the classification of the flange and/or web. This may also influence the design approach and failure mode. For instance, local buckling of the compression flange could shift to a web buckling failure (Zhang *et al.*, 2021).

In Zhang's (2021) study, the influence of corrosion on the flexural buckling behavior of steel beams was investigated through an accelerated corrosion test on steel members. H-section steel members, made from common Q345 grade Chinese structural steel with a yield strength of 345 MPa and a tensile strength of 470–630 MPa, were selected for an outdoor artificial accelerated corrosion test. Five groups of H-section steel beams with varying degrees of corrosion were examined every three months, and these specimens were labeled B-1 through B-5. The 4-point bending test, as shown in Figure 02a, was used for the experimental setup. The dimensions of the steel beam sections are presented in Figure 02b.

Figure 02 - Experimental and section size of steel beam.

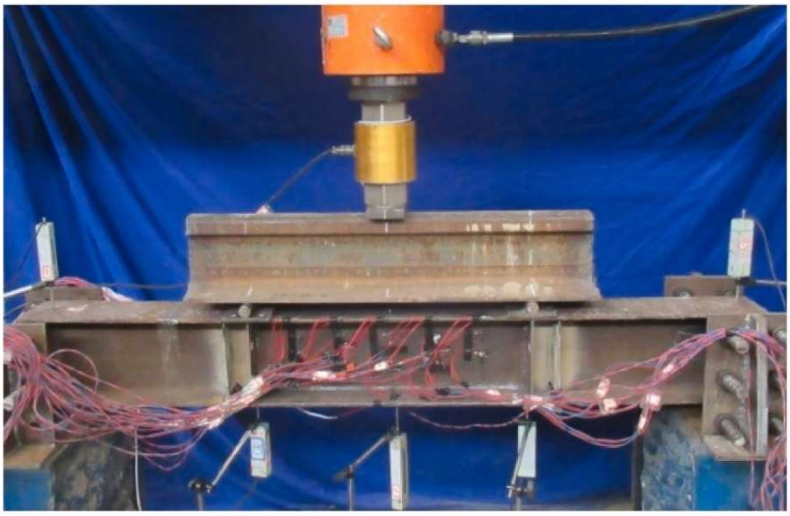

a) Experimental setup.

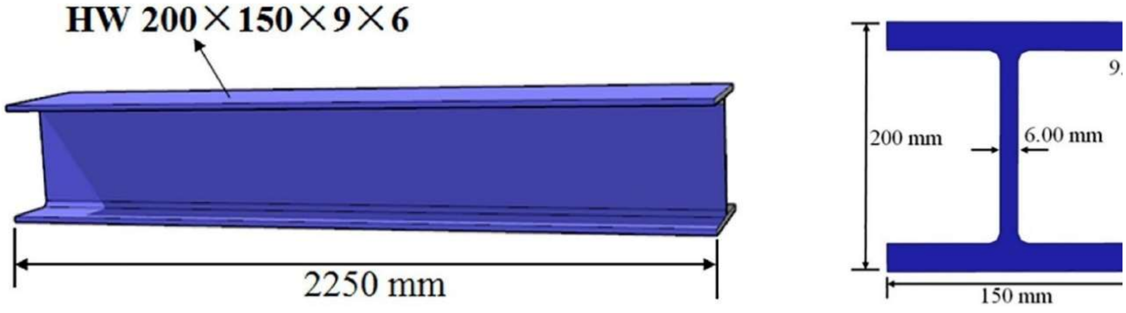

b) Section size of steel beam.

Source: Zhang et at. (2021)

To assess the different behaviors after corrosion, a section classification was performed. This is the fundamental method used in current international codes to account for the effects of local buckling. Based on the width-to-thickness ratio of the plate, the AISC 360–10 specification classifies sections into three categories: Compact, Non-compact, and Slender. According to NBR 8800:2024, these sections are characterized as follows:

- **Compact section**: this type of section reaches full plasticity, allowing for large plastic rotations in its structure.
- **Non-compact**: in this section, local instability occurs after partial plasticity has developed, but without allowing significant rotations.
- **Slender section**: in this case, local instability occurs before the onset of plasticity, preventing this stage from being reached.

In this context, Figure 03 shows that as the degree of corrosion increases, the thickness of the flange and web of the specimens decreases continuously, leading to an increase in the width-to-thickness ratio of the plate. For specimen B-1, the width-to-thickness ratios of the flange and web are 8.33 and 30.33, respectively. According to the section classification in AISC 360–10, this corresponds to a compact flange and compact web. After 12 months of corrosion, the width-to-thickness ratios for the flange and web of specimen B-5 increase to 9.65 and 36.10, respectively, reclassifying the section as non-compact flange and non-compact web. Thus, corrosion reduces the cross-sectional thickness, alters the section classification, and affects the plasticity development of the section, inevitably decreasing the flexural capacity of steel members. Therefore, it is crucial to understand the degradation of flexural capacity in corroded steel members and to develop a design method for the flexural buckling capacity of existing corroded steel structures.

Figure 03. Section classification of steel beam with different degrees of corrosion.

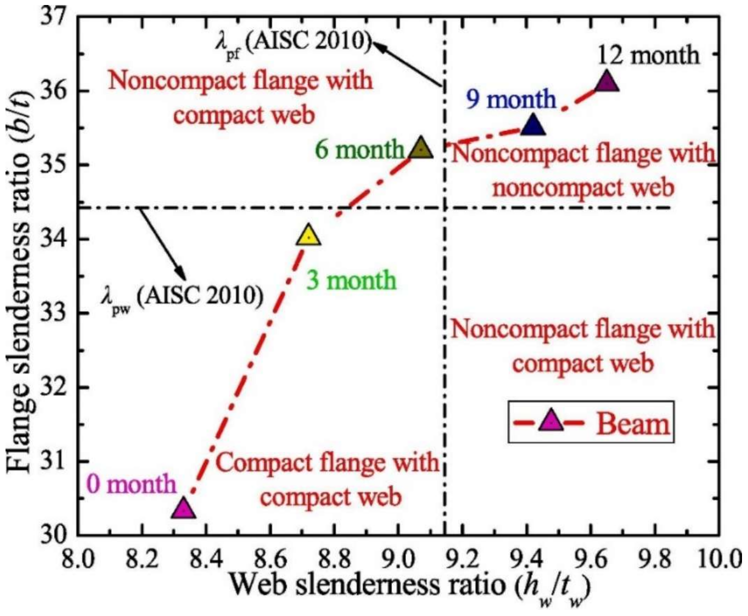

Source: Zhang et at. (2021)

Additionally, Figure 04 presents the load–displacement curves of the corroded steel beams. As the degree of corrosion increases, the ultimate loads of the specimens gradually decrease, and the corresponding deflection values decrease significantly. Corrosion diminishes the steel beam's capacity for inelastic deformation, which leads to a reduction in rotational capacity, as noted by Zhang (2021). For instance, the ultimate load of the non-corroded specimen B-1 is 601.23 kN, with a corresponding mid-span deflection of 60 mm. However, when the corrosion ratio reaches 16.88%, the ultimate load of specimen B-5 drops to 429.3 kN, and the corresponding mid-span deflection reduces to just 28 mm. As the corrosion level increases, the ultimate load and mid-span deflection are reduced by 30% and 50%, respectively.

Figure 04. The load–displacement curve of the corroded steel beams.

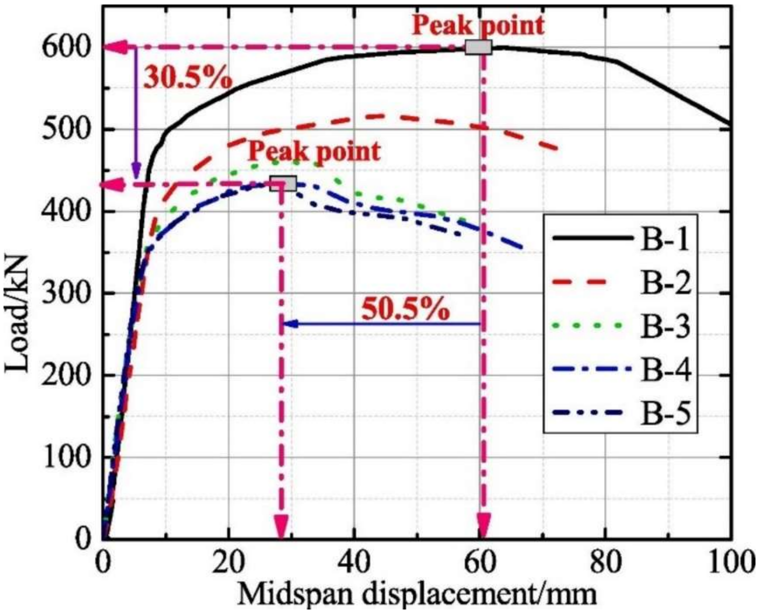

Source: Zhang et at. (2021)

Another study that analyzed the influence of corrosion on beams was conducted by (Xiao *et al.*, 2023), who investigated experimentally and numerically the degraded mechanical behavior of coastal high-performance steel beams subjected to local corrosion within the shear span. The study focused on welded Q460D high-performance steel beams and examined how localized corrosion affected load-deflection response, strain development, stiffness degradation, and failure mode. The experimental program comprised six specimens, including two reference beams and four beams with controlled corrosion damage produced by accelerated electrochemical corrosion. The geometry and arrangement of the beam, including the main dimensions and stiffener layout are shown in Figure 05a, while Figure 05b illustrates the accelerated corrosion procedure adopted to obtain the target damage levels. In turn, Figure 05c presents the loading configuration, boundary conditions, and instrumentation scheme used in the bending tests.

Figure 05 – Setup of Xiao et al (2023).

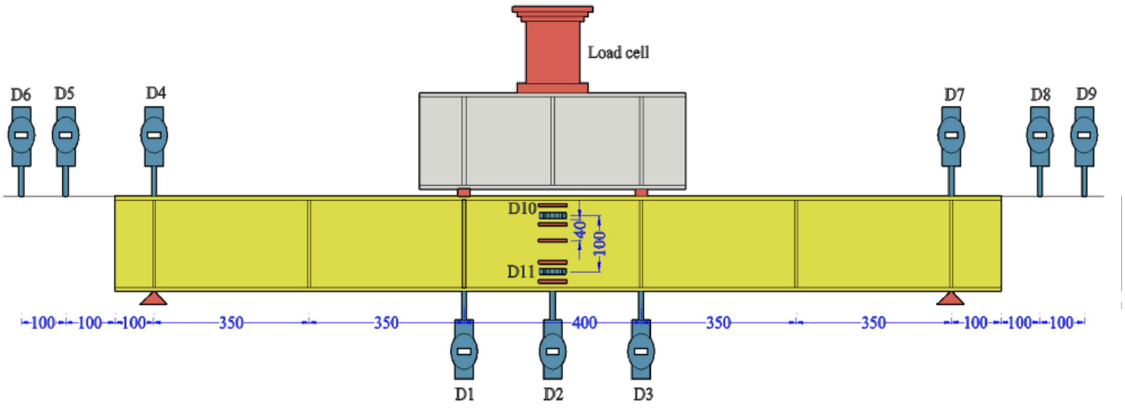

a) Dimensions and arrangements of the beam (mm).

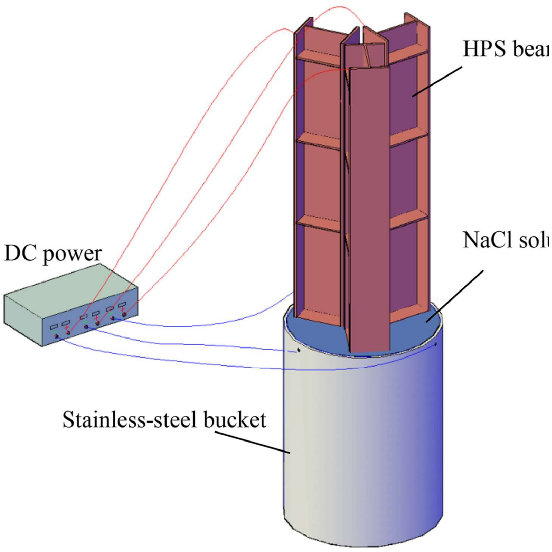

b) Accelerated corrosion test.

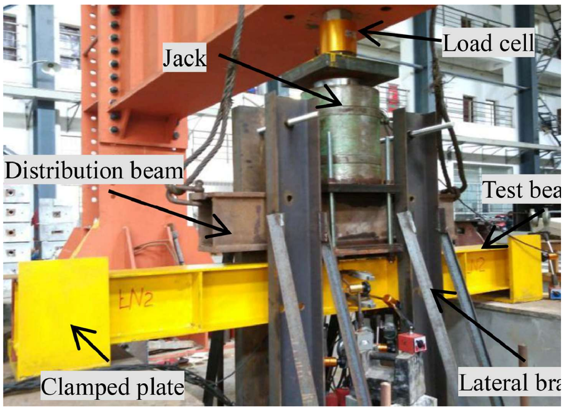

c) Setup for the tested beam.

Source: Xiao et al (2023)

(Xiao *et al.*, 2023) concludes that significant losses in strength, reaching up to 64.2%, and marked stiffness degradation were observed for corrosion levels exceeding 10%. In addition, Sheng et al. (Sheng; Xia; Ma, 2018) observed that, beyond a certain corrosion level, the buckling strength becomes lower than the yield strength, indicating that local buckling may occur before yielding and that corrosion alters failure modes, sheng also observed that strength reductions of up to 20.73% in ultimate load and 33.27% in displacement for severely corroded specimens, with corrosion rates reaching 13.07%.

This chapter presents the numerical framework developed to simulate the structural response of the steel Regarding the overall stability of steel beams under bending, (Luo *et al.*, 2022). investigated the effect of corrosion-induced section loss on the global response of rolled H-shaped members subjected to a concentrated load at mid-span. The study was carried out using Q235 steel beams with cross-sectional dimensions of 150 mm × 75 mm × 5 mm × 7 mm, aiming to examine how different corrosion levels influence the degradation of flexural stability. For this purpose, the specimens were divided into three groups according to the target corrosion rate: group A0, composed of one uncorroded reference beam; group A1, consisting of three beams with a corrosion rate of 6%; and group A2, comprising three beams with a corrosion rate of 12%. Thus, the experimental program included a total of seven specimens, allowing the authors to compare the structural behavior of intact and corroded beams under the same loading condition.

To obtain the prescribed corrosion levels, the beams were immersed in an electrified accelerated corrosion tank containing a 5% NaCl solution, as shown in Figure 06. This procedure was adopted to promote a more uniform corrosion pattern along the steel surface and to provide better control over the degradation process. In addition, steel current-conducting plates were welded to both ends of the specimens in order to reduce possible irregularities during immersion. According to the authors, this measure was necessary to avoid non-uniform corrosion that could result either from contact between the lower flange and the bottom of the tank or from the direct connection of electrical wires to the beam surface. In this way, the experimental setup shown in Figure 06 was designed to ensure a more consistent corrosion process and, consequently, a more reliable assessment of its influence on beam stability.eams investigated in this study, with emphasis on the influence of pitting corrosion on strength, stiffness, strain evolution, and failure mode. The finite element model was implemented in ABAQUS and includes the definition of mesh discretization, boundary conditions, initial geometric imperfections, constitutive modelling of steel, and residual stress patterns. In addition, a stochastic procedure based on a correlated Gaussian random field was adopted to reproduce the spatial variability of thickness loss caused by corrosion.

Figure 06. Electrochemical corrosion test.

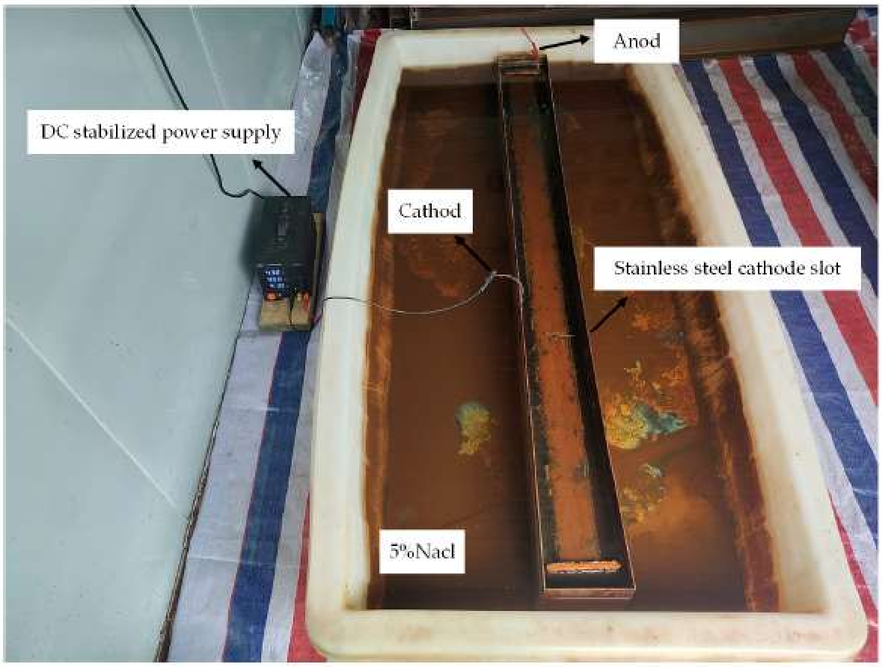

Source: Luo et al (2022)

In this study, three-point bending tests were carried out on all beam specimens, and the results showed that every specimen developed a typical global instability failure mode. According to the authors, the different corrosion rates adopted for groups A0, A1, and A2 did not alter the fundamental failure mechanism, since all beams ultimately failed by overall flexural-torsional instability. Figure 07 and 07b present the corresponding load-vertical displacement and load-lateral displacement curves, respectively, for the three groups of specimens. As shown in these figures, both the mid-span vertical displacement and the lateral displacement increased progressively with increasing load, although the response became more sensitive to corrosion as the degree of degradation increased.

During the initial loading stage, the beams exhibited a predominantly linear load-displacement response, characteristic of elastic behavior. At this stage, the vertical displacements at mid-span increased more significantly than the lateral displacements, indicating that the structural response was governed mainly by in-plane bending, with negligible out-of-plane lateral bending or torsional rotation about the z-axis. However, as the applied load increased, the beams gradually entered the elastic-plastic range, and the relationship between load and displacement became nonlinear. In this stage, the lateral displacements started to grow more markedly, revealing the onset of out-of-plane deformation and the progressive loss of overall stability, as illustrated in Figure 07.

After reaching the peak load, the beams entered the failure stage, in which the load-carrying capacity decreased while both vertical and lateral displacements increased sharply. This response indicates that the members had lost their ability to sustain additional loading and were undergoing pronounced out-of-plane torsional deformation. As a result, the final collapse of the specimens was characterized by overall flexural-torsional buckling, confirming that corrosion primarily accelerated the degradation of stiffness and stability without changing the essential mode observed in the tested beams.

Figure 07 – Curves load x vertical displacement and load x lateral displacement.

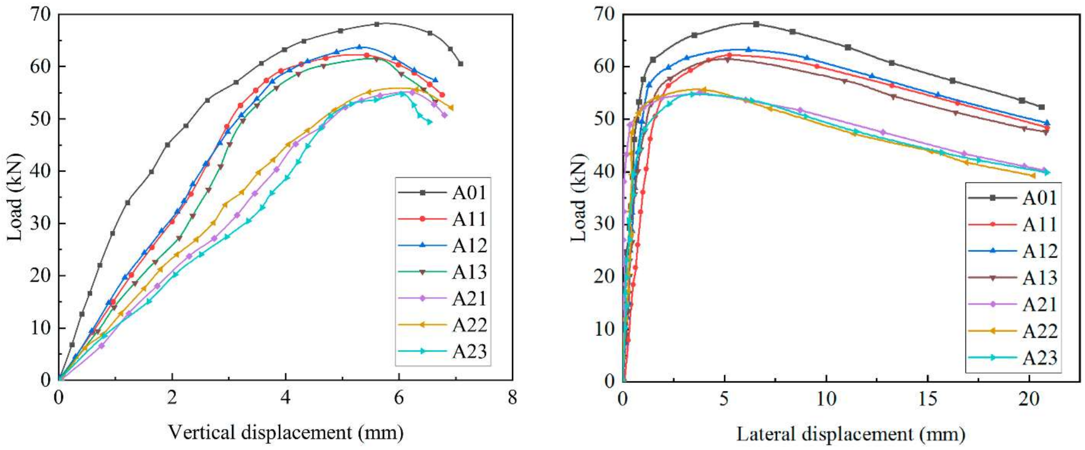

(a) Load–vertical displacement curves of the corroded steel beams.

(b) Load–lateral displacement curves of the corroded steel beams.

Source: Luo et al (2022)

As shown in the studies Zhang et al. (2021) and Luo et al. (2022) and Xiao et al. (2023) corrosion significantly affects the mechanical behavior of structural elements, altering yield strength, ultimate strength, displacement, deformations, slenderness, and failure modes. These findings are consistent with numerous other studies that have analyzed the flexural behavior of beams before and after corrosion (Bhandari *et al.*, 2015;

Chen; Jiang; Jin, 2014; Jia *et al.*, 2009; Luo *et al.*, 2022; Peng *et al.*, 2019; Ranji; Zakeri, 2011; Wang; Xu; Li, 2020; Xiao; Chen; Peng, 2024; Zhang *et al.*, 2021).

Corrosion further exacerbates these stability concerns due to material loss, increased slenderness, and geometric imperfections, thereby reducing the overall load-bearing capacity. This spontaneous phenomenon produces geometric surface damage and alters cross-sectional properties, accelerating deterioration (Benedito *et al.*, 2024; Nakai *et al.*, 2004; Nakai; Matsushita; Yamamoto, 2004, 2006; Zhang *et al.*, 2024). Accelerated corrosion is required to understand the material behavior in laboratories, as it is a long-term process. The degradation process can be accelerated using various techniques, including immersion in chloride solutions with or without applied electric current (electrochemical acceleration), immersion in sulfuric acid solutions, or exposure to salt spray in controlled chambers (Chen; Jiang; Jin, 2014; Nam; Kim, 2010; Zhang; Zheng; Zhao, 2023). Salt spray induces pitting corrosion in metals (Ayodeji *et al.*, 2021; Katona *et al.*, 2021), a complex degradation process influenced by both environmental conditions and the material's metallurgical properties. This phenomenon is particularly critical in marine environments, where the presence of chlorides significantly accelerates corrosion and compromises the structural integrity of metallic components (Xie *et al.*, 2022). In particular, pitting corrosion is a form of attack that appears as small cavities on the material surface, which form due to localized metal dissolution at points with minor imperfections, creating potential differences (Dwivedi; Lepková; Becker, 2017; Guo *et al.*, 2020). After stabilization, the pit mouth becomes covered by corrosion products, isolating its interior and creating an acidic, anoxic environment that promotes continued corrosion and deepens the pit. Eventually, pit growth experiences a slowdown and interruption in depth increase owing to potential limitations(Melchers, 2018). However, lateral corrosion continues, expanding the pit radius and leading to coalescence with adjacent pits, as the protective corrosion products evolve and modify diffusion processes (Galleguillos Madrid *et al.*, 2024; Melchers, 2018). Pit depth follows a log-normal distribution, with the logarithmic mean increasing and the standard deviation (SD) varying as corrosion progresses (Wang *et al.*, 2024; Yamamoto; Ikegami, 1998)

Against this experimental background, numerical studies have modeled corrosion using simplified representations of section loss. For example, (Zhang *et al.*, 2021) represented corrosion by thickness reduction based on measured residual profiles, which simplifies real surface irregularities, although the degradation of mechanical properties is mainly caused by the non-uniform distribution of corrosion pits (Du; Clark; Chan, 2005, 2005; Palsson; Mirza, 2002). In this context, researchers have sought more realistic approaches to simulate non-uniform corrosion. To this end, numerical models based on randomly distributed thickness fields have been developed to represent the stochastic nature of corrosion damage (Garbatov; Tekgoz; Soares, 2017; Silva; Garbatov; Soares, 2011; Wang; Wharton; Shenoi, 2014). Building on these developments, Xiao et al. (Xiao *et al.*, 2023) simulated pitting corrosion in ANSYS using SOLID187 elements by explicitly introducing randomly distributed hemispherical pits with pit depths sampled from 3D-scan–derived statistics (mean and standard deviation).

A similar assumption was adopted by Mahdavipour et al. (Mahdavipour *et al.*, 2026) in a stochastic lateral–torsional buckling study, where pit morphology was generated probabilistically by sampling pit locations uniformly over the surface and pit geometry from prescribed distributions, and corroded cases were addressed mainly through probabilistic simulations. Although these formulations capture randomness in pit geometry, pitting is frequently reported to occur in clustered bursts rather than as fully independent events, therefore treating pit occurrence as spatially uncorrelated can be a weakness because it may underrepresent realistic pit clustering and affect predicted stress localization. Notably, both studies neglected an explicit spatial-correlation model for pit occurrence (Coelho *et al.*, 2023; Lunt *et al.*, 1997; Wu *et al.*, 1997).

In this context, incorporating spatial correlation has been pursued to better reflect clustered corrosion patterns. In particular, (Woloszyk; Garbatov, 2020) and (Melchers, 2005) showed that introducing a high degree of spatial correlation in random-field models improves the representation of corrosion morphology and its influence on mechanical response, consistent with experimental evidence that deep pits tend to develop in strongly dependent, clustered patterns rather than as independent defects. Woloszyk and Garbatov (Woloszyk; Garbatov, 2020) Modelled spatially correlated non-uniform corrosion within finite element analyses using Gaussian random fields, with spatial dependence prescribed by an autocovariance function parameterised by a correlation length and discretised via a Karhunen–Loève expansion. The approach provided good agreement for low to moderate degradation levels, whereas accuracy deteriorated for corrosion levels above 15%. Teixeiras and Soares (Teixeira; Soares, 2008) represents corrosion as a spatially correlated lognormal thickness-loss random field calibrated from inspection data, with correlation prescribed by a squared-exponential autocorrelation function (correlation length) and generated via expansion optimal linear estimation. Zhang et al. (Zhang *et al.*, 2025) models corrosion morphology as a spatially correlated random field by decomposing measured surface topography via Lanczos filtering and fitting a hole-Gaussian autocorrelation function to obtain correlation length and standard deviation parameters for surface reconstruction.

Although recent studies have demonstrated that spatially correlated random fields provide a more realistic representation of corrosion morphology and its mechanical implications, most existing applications have focused on conventional steel components and on global response measures. This limitation becomes particularly relevant when considering structural systems whose resistance is strongly governed by local instability phenomena, since corrosion-induced thickness loss may interact with geometric slenderness and stress concentration in a more critical manner. In this context, castellated beams represent a particularly important case, as their perforated web geometry and reduced web-post regions make them especially sensitive to instability mechanisms. Therefore, before addressing the effects of corrosion on such members, it is necessary to examine the structural characteristics of castellated beams and the fundamental mechanics associated with web-post buckling.

2.2 CASTELLATED BEAM AND WEB-POST BUCKLING

The emergence of castellated beams is closely associated with the development of electric welding at the end of the 1920s. Literature records indicate the use of castellated beams manufactured in the early 1930s by the Skoda works in Plzeň for the structure of an industrial building in Doudlevka, Czech Republic (Grünbauer BV, 2026). The first patent request specifically related to castellated beams was filed in 1937 by

Geoffrey Murray Boyd and was granted by the British Patent Office in January 1939. For this reason, castellated beams are also referred to in some regions as Boyd beams. Following their initial development and practical application, research on their geometry and structural behavior began to appear more systematically during the mid-twentieth century. Among the earliest contributions are the analytical study of (GIBSON; JENKINS, 1957), developed in England, and the experimental program conducted by (TOPRAC; COOKE, 1959) in the United States. In the following decades, further investigations were carried out through analytical approaches (Boyer, 1964; CIMADEVILA, Francisco Javier Estévez; GUTIÉRREZ, Emilio Martín; RODRÍGUEZ; Vázquez., 2000; GALAMBOS; HOSAIN; SPEIRS, 1975), experimental studies (Grilo *et al.*, 2018; Kerdal; Nethercot, 1984; Redwood; Demirdjian, 1998; Vieira, 2015; Zaarour; Redwood, 1996) and numerical analyses (Kerdal; Nethercot, 1984; Vieira, 2015).

Castellated beams are fabricated by cutting the web of standard I-sections in a zigzag pattern and subsequently reassembling the halves in an offset configuration, creating expanded webs with a series of regularly spaced hexagonal openings (Kerdal; Nethercot, 1984). This manufacturing process also forms tee sections positioned above and below the openings, enhancing bending stiffness and improving the strength-to-weight ratio. Such a configuration allows castellated beams to span longer distances without substantially increasing their self-weight, making them particularly advantageous for large-scale applications such as industrial buildings, warehouses, and bridges (De Oliveira; Cardoso; Sotelino, 2019; Grilo *et al.*, 2018). However, the maintenance and structural integrity of such structures are issues with substantial economic implications. Therefore, despite structural efficiency and reduced material of castellated beams (Vieira, 2015), there is a need to understand the mechanical behavior of corroded elements.

Among the various castellated beam configurations, Anglo-Saxon castellated beams are characterized by a web opening angle of 60° and by a final height approximately 50% greater than the opening depth. Although these geometric modifications improve structural efficiency, they also increase slenderness and make the member more susceptible to local instability phenomena, particularly web-post buckling (WPB) (Kerdal; Nethercot, 1984). WPB is primarily associated with the action of shear forces, which generate inclined compressive stresses in the web-post region between adjacent openings. As these stresses increase, the web-post may lose stability through lateral displacement and twisting about the vertical axis, leading to a reduction in stiffness and a premature decrease in load-carrying capacity before the ultimate resistance of the section is fully mobilized (Grilo *et al.*, 2018). To illustrate, the web-post of a castellated beam is subjected to internal forces as shown in Figure 08. The shear force Facting along the welded joint induces tensile stresses along edge AB, while edge CD is subjected to compressive stresses, which may trigger buckling of the web-post. Once this instability develops, the lateral displacement is accompanied by rotation about the diagonal line xx', as also indicated in Figure 08. This collapse mechanism is commonly referred to as shear-induced web-post buckling.

Figure 08 – Web-post Buckling.

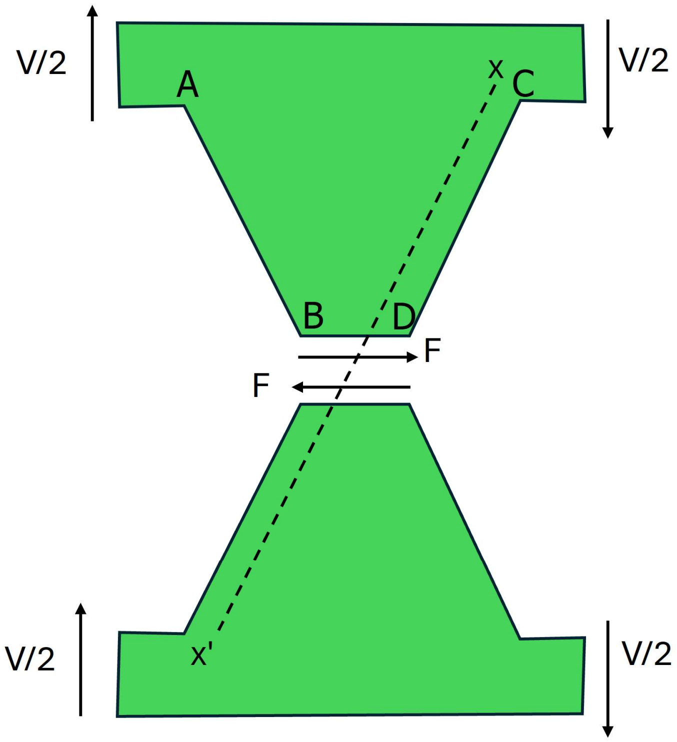

Source: The author (2026)

According to Zaarour and Redwood (1996) and Redwood and Demirdjian (1998), the susceptibility of castellated beams to WPB is strongly influenced by a set of geometric ratios

- the opening height relative to the total beam depth (h_o/d_g);
- the opening height relative to the minimum web-post width (h_o/b_w);
- the opening height relative to the web thickness (h_o/t_w);
- the minimum web-post width relative to the web thickness (b_w/t_w);
- the height of the expansion plate relative to the opening height (h_p/h_o).

From a mechanical standpoint, corrosion is expected to directly affect this instability mechanism because it reduces the thickness of the steel plates, particularly the web thickness t_w, which is one of the most relevant parameters governing WPB. As corrosion progresses, the ratios h_o/t_w and b_w/t_w increase, reducing the local stability of the web-post and potentially accelerating the onset of buckling. Therefore, even when the original geometry remains unchanged, corrosion-induced thickness loss may significantly alter the structural response and failure mode of castellated beams.

Although no specific study has yet been identified on castellated beams subjected to corrosion and failing by WPB, several approaches have been proposed to predict the shear force associated with this failure mode in non-corroded members. Kerdal and Nethercot (Kerdal; Nethercot, 1984) state that WPB in castellated beams arises from compressive forces induced by shear and can be modeled as the buckling of a column with a cross-sectional area equivalent to the welded joint and an effective height equal to the opening depth. The approach assumes that yielding of the web precedes the onset of buckling. Lawson et al. (Lawson *et al.*, 2006) developed a strut model treating the web-post as a centrally restrained strut, correlating buckling resistance with the effective length and width of the web-post in accordance with the BS5950 (BS5950, 2000) and BS EN 1993-1-1 (Eurocode 3, 2005) standards. Redwood and Demirdjian (Redwood; Demirdjian, 1998) applied plate shear buckling theory to the upper segment of the web-post, introducing buckling coefficients dependent on geometric parameters such as spacing and web-post thickness. Wang et al. (Wang *et al.*, 2016) proposed a method that calculates the vertical shear buckling strength of the web-post by treating the upper part of the web-post as a free body under a horizontal shear force, whose shear buckling strength can be determined using thin-plate shear buckling theory.

Despite the broad body of literature dedicated to non-corroded castellated beams, the influence of corrosion on WPB has not yet been examined. This gap is particularly relevant because corrosion may intensify the instability of the web-post, further reducing the shear resistance, stiffness, and overall safety of slender steel members with perforated webs. In this context, the present study investigates experimentally the behavior of corroded Anglo-Saxon castellated steel beams governed by WPB and proposes an analytical model capable of representing this behavior with improved accuracy. The study aims to examine the full WPB process in corroded castellated beams subjected to three-point bending using digital image correlation (DIC), to evaluate the statistical significance of the main parameters affecting buckling resistance, and to assess the predictive accuracy of the proposed formulation by comparison with Steel Design Guide 31 (Sameer S. Fares; Coulson; David W. Dinehart, 2016) and EN 1993-1-13:2024 (Eurocode 3, 2024). In addition, two steel grades ASTM A572 Grade 50 and Grade 60, were examined in both non-corroded and corroded conditions to evaluate whether the yield strength influences the susceptibility to WPB and the accuracy of the proposed model.

CHAPTER 03 – EXPERIMENTAL PROCEDURE

In this chapter, the fabrication process of the beams and test specimens will be presented, followed by a description of the salt spray chamber utilized and its operational procedure. The pre-conditioning steps performed on the specimens before exposure in the salt spray chamber will also be detailed. Additionally, the methodologies for the tensile tests and the three-point bending tests will be outlined.

3.1 FABRICATION OF TEST SPECIMENS AND BEAMS

This subsection describes the fabrication of the beams and specimens used in this study, with all cutting and welding processes carried out at METALFENAS, a company located in the city of Rio de Janeiro. The first step details the cutting and welding process of the castellated beams. This involves a zigzag cut along the web of an I-beam profile, Figure 09a. Afterward, the two parts of the beam are separated and then welded back together, Figure 09b. The final product is a beam with sequential hexagonal web openings, which increases height compared to the original I-beam profile, Figure 09c and 09d.

Figure 09 - Steel castellated I-beams manufacturing.

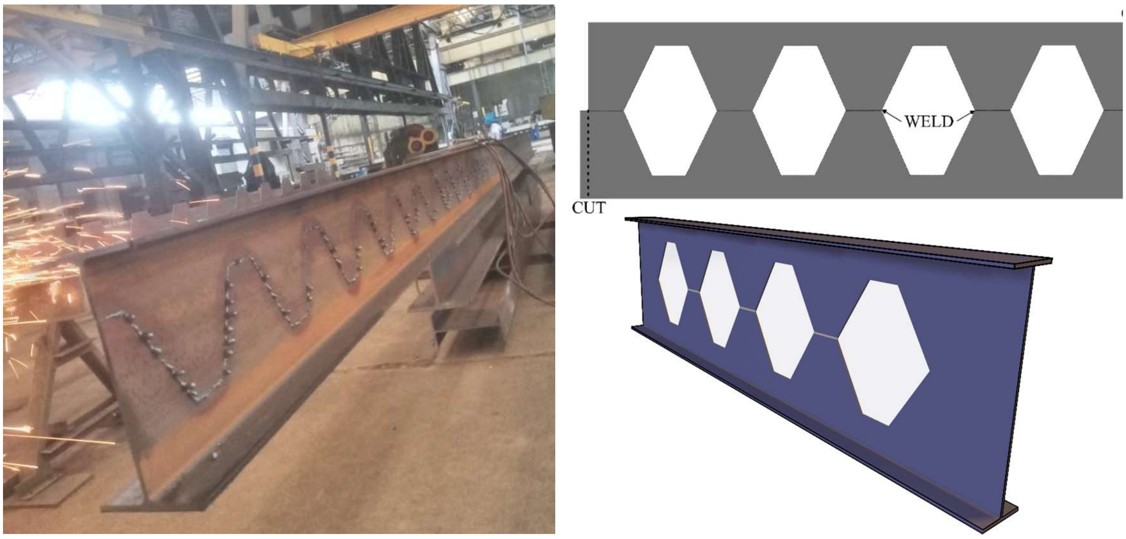

a) Thermal cutting.

b) Castellated beam after welding.

c) Manufactured steel castellated I-beams.

d) Manufactured steel I-beams.

Source: The author (2026)

Parent profiles were used to extract the dog-bones following ASTM E8. Figure 10 (a) shows the plasma-cutting process carried out on the profiles, while Figure 10(b) presents the standardized specimen dimensions.

Figure 10 - Tensile Coupon.

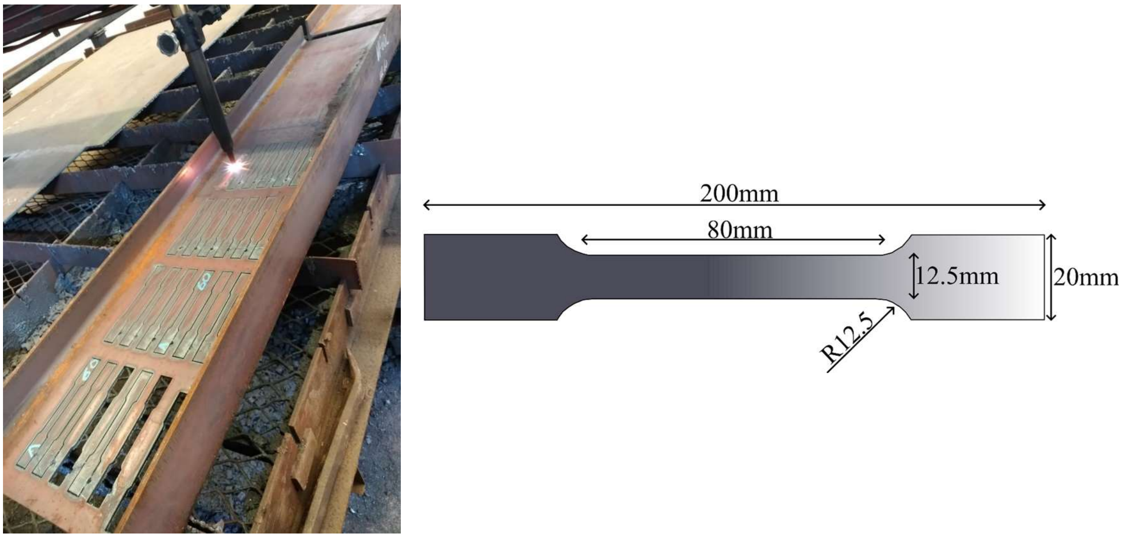

a) Plasma cutting. b) dimensions of the specimens.

Source: The author (2026)

3.2 SALT SPRAY AGEING

A large-scale chamber, Figure 11 was utilized with the aim to evaluate degradation mechanisms in specific environments at varying aging rates and collect data to predict the behavior of the beams after 6 months. The selected temperature was 55°C. The salt-spray accelerated aging tests were conducted with specimens exposed to approximately 4068 hours (6 months) of continuous aging inside salt-spray chambers.

Figure 11. Salt-spray chambers.

Source: Lopes (2023)

The ASTM B-117 and ASTM D-1193 standards were used to establish sodium chloride composition, salt spray concentrations, pH levels, and water conductivity. These parameters were monitored during the preparation and management of the tests. Table 1 outlines the parameters according to the referenced standards, while Table 1 and Table 2 details the maximum permissible impurities in the sodium chloride used for the testing.

Table 1 - Salt spray preparation parameters reference values.

Parameter	**Value**	**Observations**
Salt Solution Concentration	4-6%	
Salt Solution pH	6.5-7.2	$at\ 23\ \pm 3°C$
Water Conductivity	$< 5.0\mu S/cm$	ASTM D1193 - Type IV

Source: The author (2026)

Table 2 - Maximum allowable amounts of impurities in the sodium chloride compositions

Impurity Description	**Allowable Amount**
Total Impurities	≤ 0.3%

Halides (Bromide, Fluoride and Iodide) excluding Chloride	< 0.1%
Copper	< 0.3 ppm
Anti-caking Agents	None added

Source: The author (2026)

All beams and specimens were cleaned, measured, and weighed prior to being introduced into the chambers. The specimens were thoroughly cleaned to ensure they were as close to the base material as possible, allowing the corrosive agents to act directly on the steel. The cleaning process followed the standard ASTM G1 for cleaning specimens and beams. A grinder, Figure 12a, was used for cleaning the specimens, Figure 12b and 12c show the Coupons before and after cleaning.

Figure 12 –Coupons before and after cleaning.

a) Ferrari LCM-4X6–370W–127V-220V.

b) specimen before cleaning.

c) specimen after cleaning.

Source: The author (2026)

For the beams, an angle grinder sandpaper was used. Figure 13 illustrates the cleaning process of the beams before their placement in the salt spray chambers.

Figure 13 - Cleaning beam process.

Source: The author (2026)

The beams and specimens were weighed as illustrated in Figure 14a and 14b.

Figure 14 - Weighing coupons.

(a) HC411.

(b) M503H.

Source: The author (2026)

The positioning of both the tensile specimens and the beam specimens inside the salt-spray chamber followed the requirements established by ASTM B117, which recommends that the exposed elements must not be in contact with each other and must be arranged with an inclination between 15° and 30°. These conditions are important to ensure adequate exposure of the surfaces to the saline environment and to avoid interference in the corrosion process caused by specimen contact or inadequate drainage of the solution. In order to guarantee the correct inclination throughout the exposure period, a specific supporting device was employed, as illustrated in Figure 15. This device ensured that the specimens remained stable and consistently positioned according to the prescribed angle during the entire accelerated corrosion procedure.

Both Grade 50 and Grade 60 specimens were placed inside the chamber under a controlled temperature of 55°C, as shown in Figure 16. This elevated temperature was adopted to accelerate the corrosion process and to promote more pronounced material degradation within a practical experimental time frame. For the tensile characterization, three specimens of each steel grade were scheduled to be removed and tested every month. Considering a total exposure period of six months, this testing plan resulted in 36 specimens for Grade 50 and 36 specimens for Grade 60, corresponding to a total of 72 tensile specimens. This experimental program allowed the progressive influence of corrosion exposure time on the mechanical properties of both steel grades to be systematically evaluated.

Figure 15 - Sample positioning Chamber B.

Source: The author (2026)

Figure 16 - Beam positioning Chamber B.

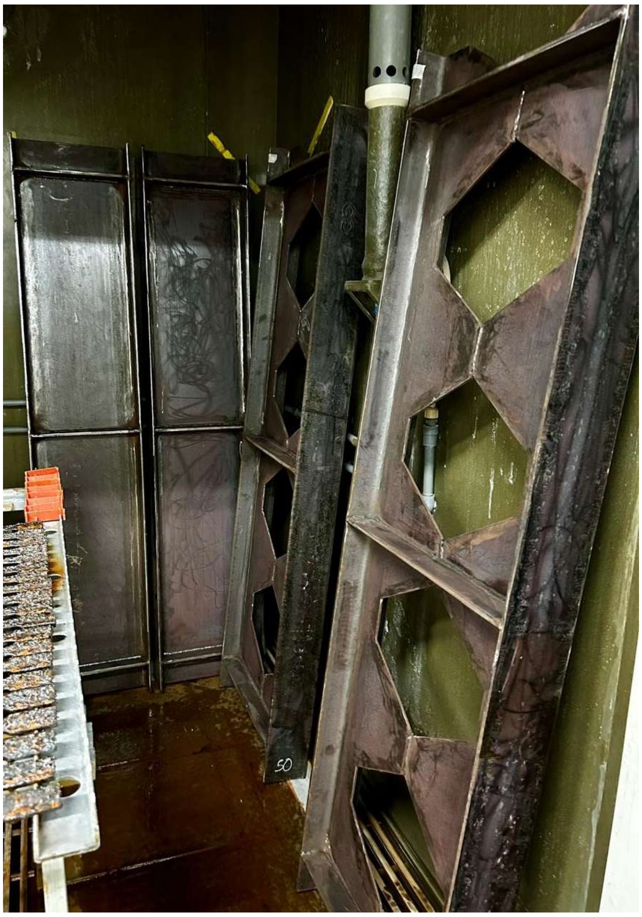

Source: The author (2026)

3.3 TENSILE TEST

The tensile tests were carried out using an MTS 311.31 universal testing machine with a load capacity of 1000 kN, as illustrated in Figure 17. The loading protocol was defined in two stages to ensure adequate control of the specimen response throughout the test. Initially, the test was performed under a crosshead rate of 0.18 mm/min until a displacement of 0.9 mm was reached, allowing a more stable and accurate characterization of the initial elastic response and the onset of yielding. After this stage, the loading rate was increased to 2 mm/min and maintained until the maximum load was reached during the strain-hardening phase. This procedure was adopted in accordance with ASTM E8, ensuring that the tensile response was obtained under conditions consistent with the standard requirements for metallic materials.

Figure 17 - MTS 311.31.

Source: The author (2026)

An MTS extensometer model 632.13F-20 was used to measure the longitudinal strain. Before the tests, grooves were made on the ends of the specimens to prevent slipping during testing, as illustrated on Figure 18.

Figure 18 - grooves on specimen.

Source: The author (2024)

The tensile test setup is shown in Figure 19. During the test, the extensometer was mounted directly on the specimen and secured using elastic bands in order to ensure stable attachment and continuous measurement of axial deformation throughout the loading process.

Figure 19 - Test setup.

Source: The author (2026)

3.4 SETUP BENDING TEST

3.4.1 Setup for solid web beams

The W360 x 32.9 profile was selected for this study. The steel strengths chosen were ASTM A572 Grade 50 and Grade 60. The load was applied at midspan using an MTS hydraulic actuator with a 1000 kN capacity. The tests were performed under displacement control at two displacement rates: 0.3 mm/min up to a displacement of 12 mm, followed by 1.5 mm/min until failure. Data were recorded at a frequency of 5 Hz.

Figure 20 illustrates the instrumentation to monitor the test. Vertical displacements were measured using three displacement transducers (D01, D02, and D03) with a gauge length of 100mm at the midspan to capture the deflection, and at both supports to capture possible rigid-body movement. One horizontal displacement transducer (D08) of 50 mm was employed to capture lateral displacement. Five strain gauges, with a gauge factor of 2.17, were fixed along the beam height at midspan to measure longitudinal strain (S01, S02, S03, S04, and S05), for analysis of the section strain distribution along the loading. Displacement transducers D01 and D02 were used to monitor support accommodation to discount rigid body movements of the central displacement (CD), which was updated using the equation $\mathrm{CD} = \mathrm{D03} - \left(\frac{\mathrm{D01}+\mathrm{D02}}{2}\right)$.

Figure 20 - Setup solid web beam.

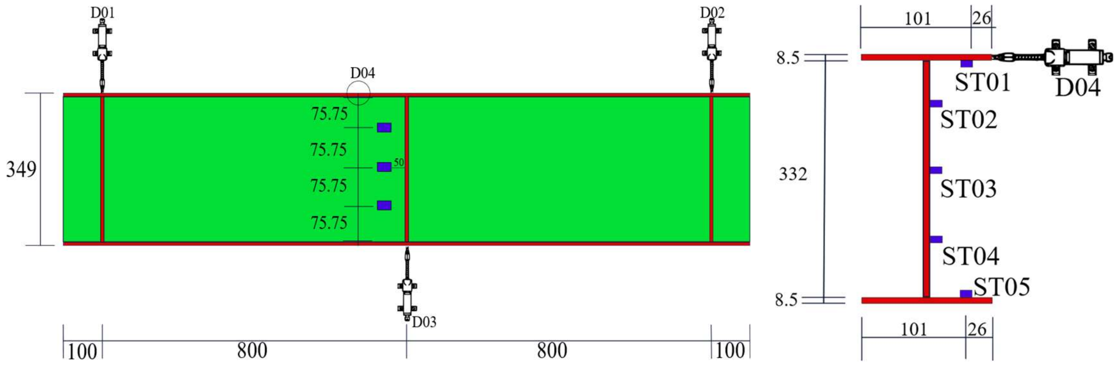

a) Longitudinal instrumentation.

b) Transverse instrumentation.

c) Beam instrumented in the laboratory.
Source: The author (2026)

3.4.2 Setup for castellated beams

Figure 21 shows the experimental setup for the three-point bending test. Vertical and lateral displacements were measured on one side using LVDTs, while midspan strains were recorded with electrical resistance strain gauges. DIC was applied to the opposite side. The castellated beams were simply supported by fork supports at both ends (De Oliveira *et al.*, 2025; Grilo *et al.*, 2018). The load was applied at midspan using an MTS hydraulic actuator with a 500 kN capacity. The tests were performed under displacement control at two displacement rates: 0.3 mm/min up to a displacement of 12 mm, followed by 1.5 mm/min until failure. Data were recorded at a frequency of 5 Hz.

Figure 21 - Test setup Castellated beam.

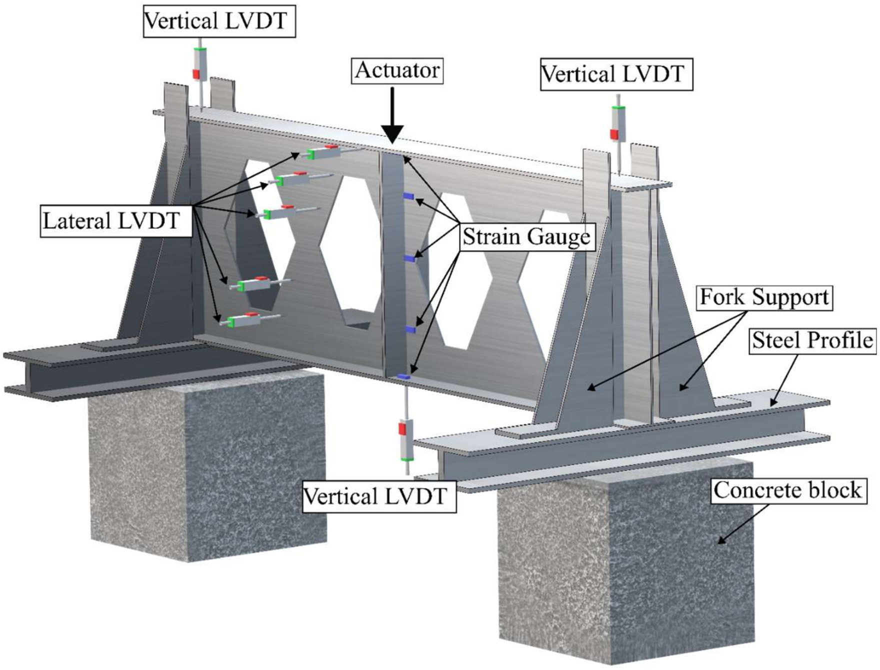

Source: The author (2026)

Figure 22a illustrates the instrumentation to monitor the test. Vertical displacements were measured using three displacement transducers (D01, D02, and D03) with a gauge length of 100mm at the midspan to capture the deflection, and at both supports to capture possible rigid-body movement. Five horizontal displacement transducers (D04, D05, D06, D07, and D08) of 50 mm were employed to capture lateral displacements, specifically the WPB formation. Five strain gauges, with a gauge factor of 2.17, were fixed along the beam height at midspan to measure longitudinal strain (S01, S02, S03, S04, and S05), for analysis of the section strain distribution along the loading. Displacement transducers D01 and D02 were used to monitor support accommodation to discount rigid body movements of the central displacement (CD), which was updated using the equation $\mathrm{CD} = \mathrm{D03} - \left(\frac{\mathrm{D01}+\mathrm{D02}}{2}\right)$.

Figure 22 - Test measurements.

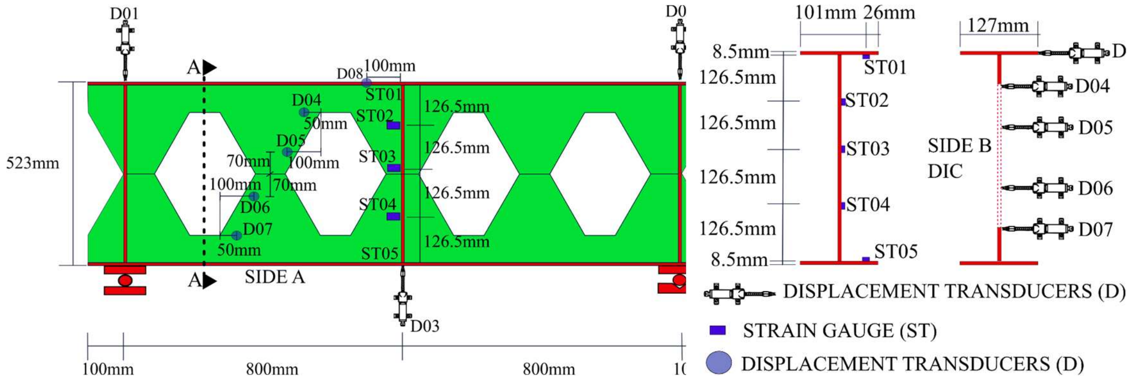

a) Test instrumentation. b) Section A–A.

Source: The author (2026)

Figure 23a and 23b shows the three-dimensional DIC setup used to monitor full-field displacements and strains throughout the loading process. Prior to testing, the surface of non-corroded beams was prepared by applying a speckle pattern using a textured roller over a white matte background, whereas for corroded beams, the pattern was sprayed with a random black speckle over a white matte coating to ensure uniform contrast on the rough surface. Two 5-megapixel charge-coupled device cameras were positioned with a convergence angle of approximately 25° under uniform LED illumination. Stereo calibration was performed using a VIC-3D target to correct optical distortions. Images were captured every 10 s and processed with VIC-3D software to obtain displacement and strain fields. The lateral displacements of the web-post were extracted along an inclined line parallel to the open edge, as shown in Figure 23c, selected due to field symmetry. To capture the variability in pit depth, 3D surface profiles of the upstream web were acquired prior to loading, from which pit depths were measured and fitted to a log-normal distribution to determine the mean and SD. This experimental procedure follows DIC practices validated by Ma et al. (Ma *et al.*, 2024) and Ma et al. (Ma *et al.*, 2020).

Figure 23 - Digital image correlation setup and analysis.

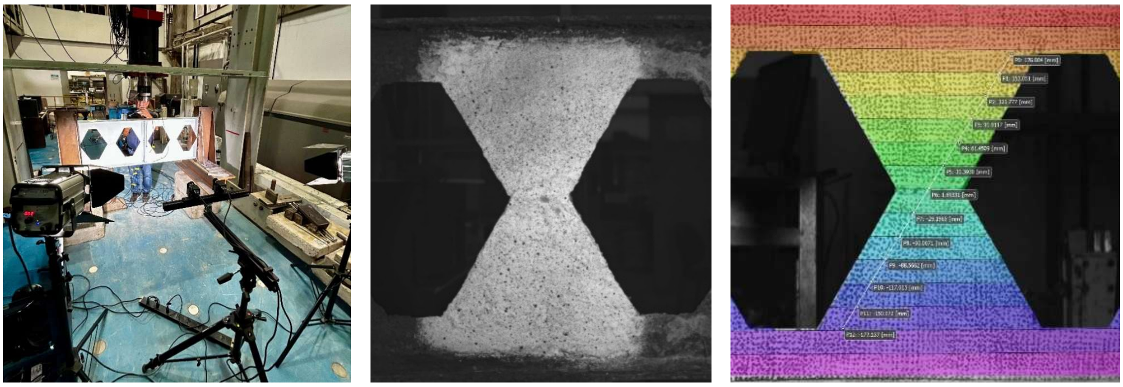

a) DIC - non-corroded beam
b) DIC - corroded beam
c) Inclined line for lateral displacement measurement

Source: The author (2026)

3.5 EXPERIMENTAL RESULTS

This section presents the experimental results obtained from tensile and flexural tests performed on steel specimens and beams, both in their non-corroded condition and after exposure to a corrosive environment. The objective is to systematically evaluate the effects of corrosion on material properties and structural behavior, establishing a direct link between the degradation observed at the material level and its implications for member performance.

The discussion is organized into three main parts. First, the tensile test results are analyzed to quantify the influence of corrosion on strength, stiffness, and ductility of the steel coupons, as well as their relationship with mass loss and stress–strain evolution. Subsequently, the flexural behavior of solid web beams is examined, focusing on load–displacement response, strain distribution, and changes in failure mechanisms induced by corrosion. Finally, the response of castellated beams is presented, with particular attention to web-post buckling and the role of corrosion in accelerating instability and reducing load-carrying capacity.

3.5.1 **Tensile test**

Tensile tests were performed to evaluate the influence of corrosion on the mechanical properties of the steel coupons, with particular emphasis on the evolution of yielding, strength, and ductility as the degradation level increased. These results complement the beam tests, since the reduction in material capacity caused by corrosion helps explain the deterioration observed in the structural response of the corroded members. In this sense, the coupon tests provide a more direct assessment of the relationship between mass loss and the progressive modification of the material stress-strain behavior. In addition, Figure 24a and 24b show the non-corroded and corroded specimens after testing, highlighting the yielding locations and providing a qualitative comparison of their post-test condition. These observations help illustrate the effect of corrosion on the tensile response of the material, particularly with respect to the reduction in deformation capacity before fracture.

Figure 24 - Tensile tests of steel coupons.

a) Non-corroded coupon after tensile test.

b) Corroded coupon after tensile test.

Source: The author (2026)

Figure 25a, 25b, and 25c present the evolution of mass loss together with the stress-strain curves obtained for the corroded coupons, with stresses calculated based on the nominal cross-sectional area of the specimens (Imperatore; Rinaldi; Drago, 2017; Ou; Susanto; Roh, 2016). The stress-strain results shown in Figure 25b and 25c correspond to the average response obtained from the tensile tests carried out for each exposure condition, while the individual results of each tensile test are presented in Appendix A. Taken together, these results provide important insight into the progressive deterioration of the steel material and help explain the mechanisms associated with the reduction in ductility observed in the corroded beam that failed by web-post buckling (WPB). In both Grade 50 and Grade 60 steels, the corrosion process led to a gradual increase in material loss with increasing exposure time. After 30 days of exposure, the measured mass loss was still relatively limited, with values close to 2.6%. At 60 days, however, the mass loss had already exceeded 4%, indicating a clear intensification of the degradation process. After 90 days, the loss reached approximately 7.8% for both steel grades, and at 180 days it exceeded 15%, demonstrating that corrosion became progressively more severe as the exposure period increased (Apostolopoulos; Michalopoulos, 2006). These values are also consistent with the mass losses measured in the beam specimens, which reinforces the representativeness of the coupon tests for interpreting the structural behavior observed at the member level.

The time-dependent variation in corrosion intensity may be interpreted as occurring in two distinct stages. In the initial stage, referred to as Mode 1, mass loss develops at a slower rate. This regime is mainly governed by oxygen diffusion, and the accumulation of corrosion products on the steel surface tends to partially hinder the access of aggressive agents to the base metal, thereby reducing the corrosion rate. As the exposure period increases, the governing mechanism changes and the process transitions to Mode 2, in which hydrogen outward transport becomes the controlling factor of corrosion kinetics (Melchers, 2018). Under this second regime, the degradation process becomes more pronounced, leading to a faster increase in mass loss and a more severe reduction in the effective resistance section. This interpretation is consistent with the progressive acceleration in material loss observed in the test results.

In addition to reducing the cross-sectional area, corrosion had a marked influence on the mechanical properties of the steel. The stress-strain curves of the corroded coupons show a clear deterioration in both strength and ductility as mass loss increased (Imperatore; Rinaldi; Drago, 2017; Ou; Susanto; Roh, 2016). For both steel grades, corrosion reduced the stress required to initiate yielding and progressively degraded the overall tensile response of the material. This behavior indicates that corrosion affects not only the geometric integrity of the steel section, but also its capacity to sustain inelastic deformation and dissipate energy before fracture. Consequently, the combined reduction in strength and deformability contributes directly to the lower structural robustness of steel members exposed to aggressive environments.

Figure 25 - Corrosion effects on steel: appearance, mass loss, and stress-strain curve.

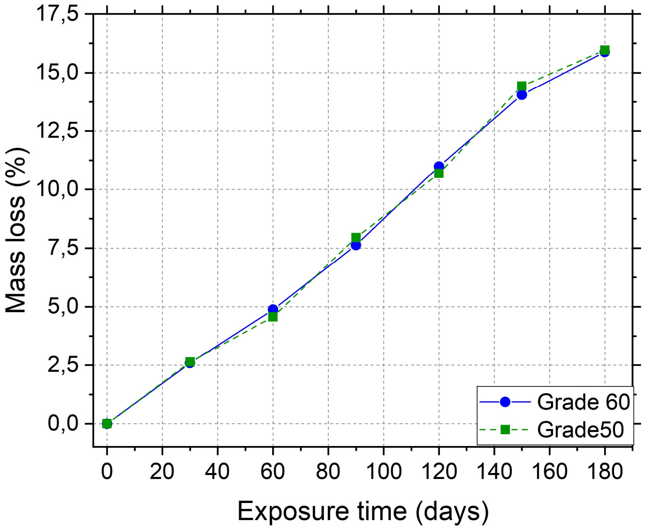

a) Impact of corrosion on mass loss.

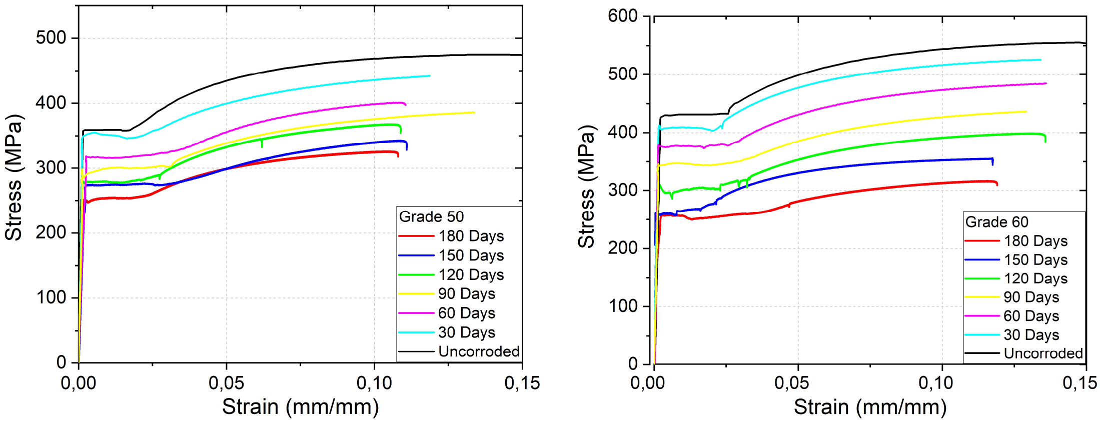

b) Stress-strain curve for Grade 50

c) Stress-strain curve for Grade 60

Source: The author (2026)

The visual appearance of the fractured coupons after testing, shown in Figure 24a and 24b, is consistent with this interpretation. The comparison between non-corroded and corroded specimens highlights the influence of corrosion on the fracture condition and provides qualitative evidence of the reduced deformation capacity of the deteriorated material. These observations reinforce the conclusion that corrosion not only reduces the resistant cross section but also compromises tensile capacity and the ability of the material to undergo plastic deformation prior to failure. In this sense, the coupon test results help clarify why corrosion may accelerate instability-related failures in structural members, especially in cases where local ductility and redistribution capacity are essential to delay the onset of collapse.

3.5.2 Solid web beams

No distinct response between corroded and non-corroded beams was observed during the early loading stage. The load–displacement curve of the corroded and non-corroded steel beams are illustrated on Figure 26, the ultimate loads decrease by 16.8% for grade 50 and 15.6% for grade 60, while the corresponding deflections decrease by 35.8% for grade 50 and 27.4% for grade 60. Once the applied load surpassed the yield load, the midspan deflection increased more rapidly and slight local buckling became evident in the compression flange.

Figure 27 presents the longitudinal strain distribution across the beam cross-section at five through-depth locations (ST01–ST05). The load levels applied to both the G50 and G60 beams were 100 kN, 200 kN, 300 kN, and 355 kN for G50, and 150 kN, 250 kN, 350 kN, and 428 kN for G60, with 355 kN for G50 and 428 kN for G60 corresponding to the yielding load of the corroded beams. Notably, for the non-corroded G50 and G60 beams, yielding strain was not reached at these load levels. When comparing the corroded and non-corroded beams at the same load levels, the corroded specimens exhibit larger deformations in the lower fibres, indicating an increased strain in the extreme fibres. This results in a reduced through-depth strain gradient, lower section curvature, and a corresponding decrease in the rotational capacity of the corroded beams (Zhang *et al.*, 2021) and (Benedito *et al.*, 2026).

Figure 26 - Load x displacement curves.

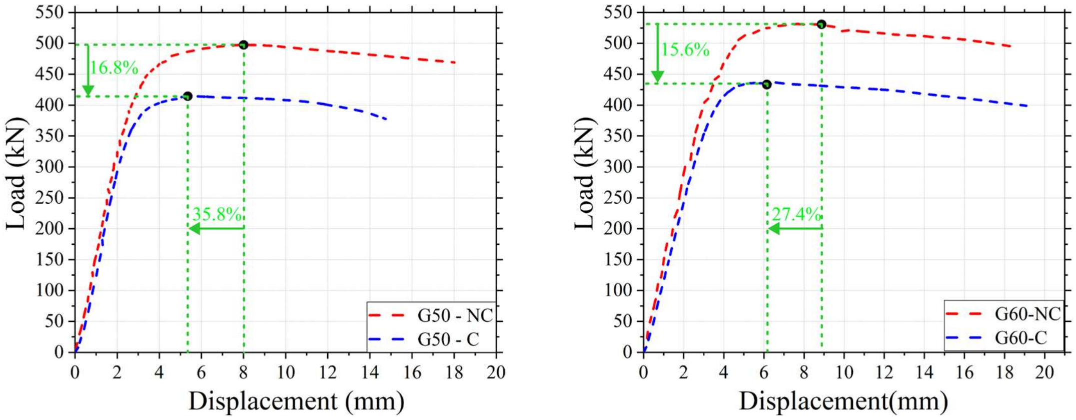

a) Curve load x displacement steel grade 50.

b) Curve load x displacement steel grade 60.

Source: The author (2026)

Figure 27 - Strain distribution along the beam section height at normalized load levels (ST01–ST05).

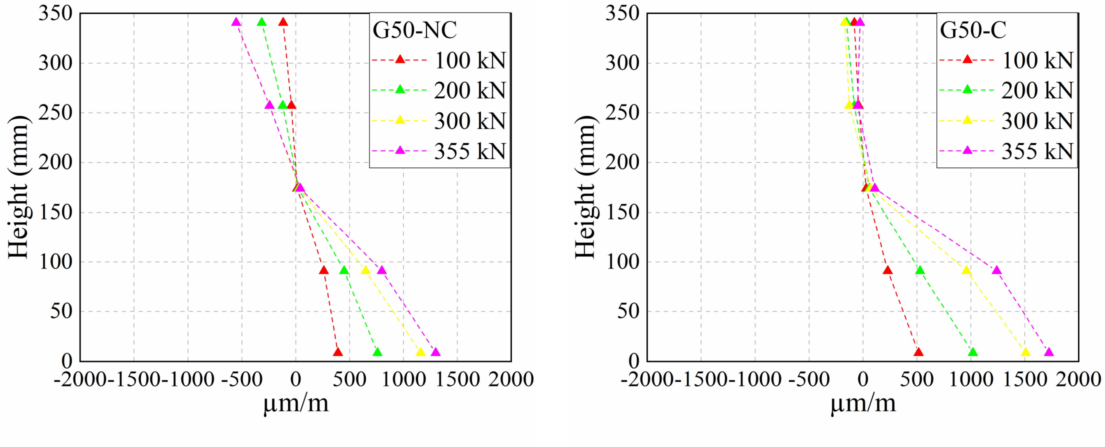

a) G50-NC: Cross-sectional strain profiles.

b) G50-C: Cross-sectional strain profiles.

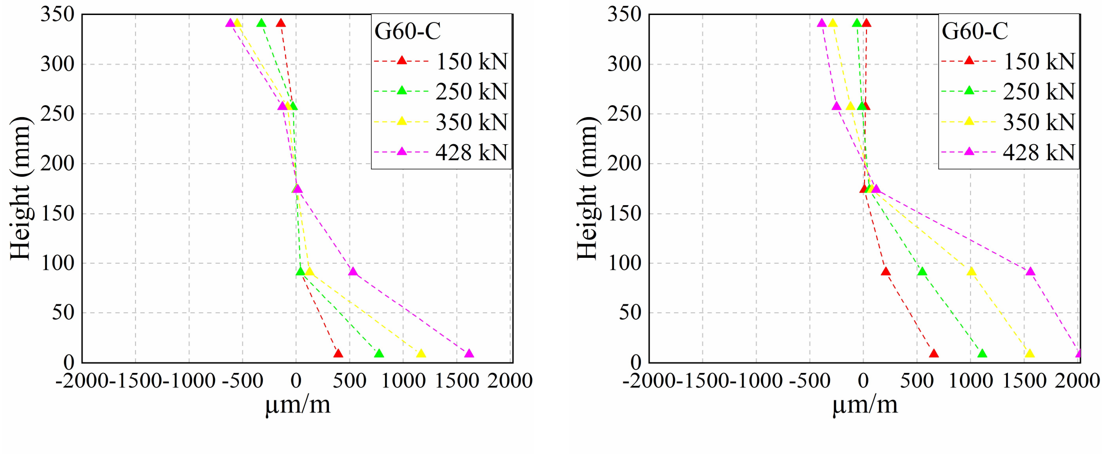

c) G60-NC: Cross-sectional strain profiles.

d) G60-C: Cross-sectional strain profiles.

Source: The author (2026)

Figure 28 presents the load–strain responses of the corroded and non-corroded beams, where negative values denote compressive strain. The inflection point of each load–strain curve is taken as the local-buckling load, indicating strain reversal. Based on the edge-fibre yielding criterion, the yield load is defined as the load at which the tensile flange reaches the yield strain, as recorded for example by strain gauge ST05. Figure 28 shows that, for both corroded beams, local buckling occurred prior to yielding, which is consistent with corrosion-driven reductions in flange thickness that increase plate slenderness, decrease out-of-plane stiffness, and introduce stress concentrations and local bending due to uneven wastage, thereby accelerating the onset of buckling and shifting the response from yielding-dominated to buckling-governed failure (Zhang *et al.*, 2021).

Figure 28 – Load x strain curves.

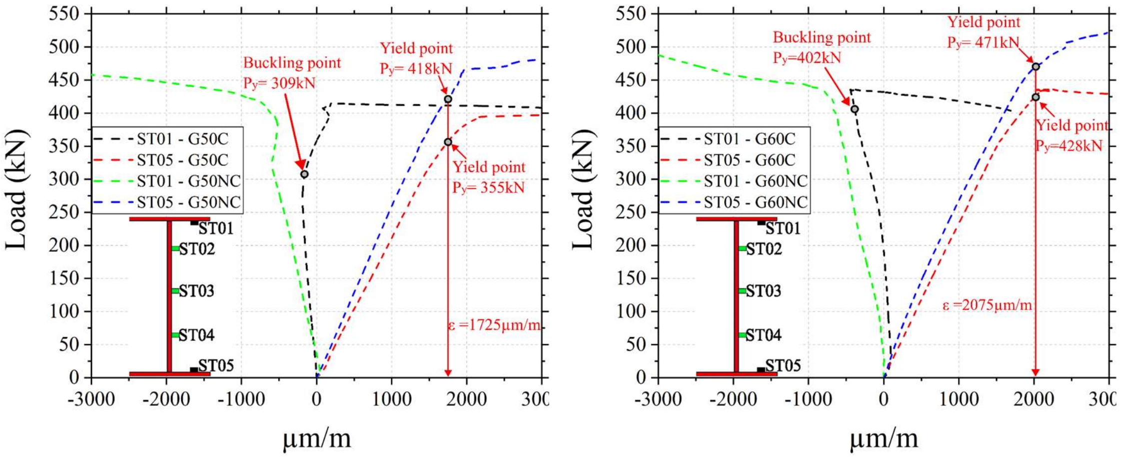

a) Strain G50-NC and G50-C.

b) Strain G60-NC and G60-C.

Source: The author (2026)

Figure 29 illustrates the observed failure modes of the non-corroded (G50-NC, G60-NC) and corroded (G50-C, G60-C) beams. In all specimens, failure is characterized by local buckling of the upper flange, but corrosion modifies the buckling pattern, leading to a distinct half-wavelength and reduced post-buckling deformation capacity. Consistent with the load–strain response, the non-corroded beams exhibit pronounced section yielding before the onset of flange buckling, whereas the corroded beams develop upper-flange local buckling prior to full cross-sectional yielding.

Figure 29 - Flange buckling on corroded and non-corroded beams.

a) G50-NC. b) G60-NC. c) G50-C. d) G60-C.

Source: The author (2026)

3.5.3 Castellated beams

Figure 30a illustrates the typical WPB mode and its deformed shape after failure, evidencing the lateral displacement δ, which is plotted in the load-displacement curves. A blue line was superimposed on the images in Figure 30 to highlight the WPB observed in both corroded and non-corroded beams, irrespective of the steel grade. The dimensions of the beams, including span and web slenderness, were chosen for WPB to be the failure mechanism, following Steel Design Guide 31 (Sameer S. Fares; Coulson; David W. Dinehart, 2016). By monitoring lateral displacements with D08, lateral-torsional buckling was ruled out, since the maximum recorded displacement at peak load was only 0.6 mm for all beams, much smaller than the corresponding web-post displacements. The failure mechanism is a result of principal compressive stresses in the web-post due to shear loading between openings (Grilo *et al.*, 2018), which is favored by the profile's high slenderness. The compressive strut typically takes the shape of a sinusoidal function for lateral displacement, a phenomenon governed by the elastic modulus of the steel and the web geometry, which is first governed by elastic buckling, not mobilizing yielding until the maximum load (Redwood; Demirdjian, 1998).

Figure 30 - WPB in corroded and non-corroded castellated beams.

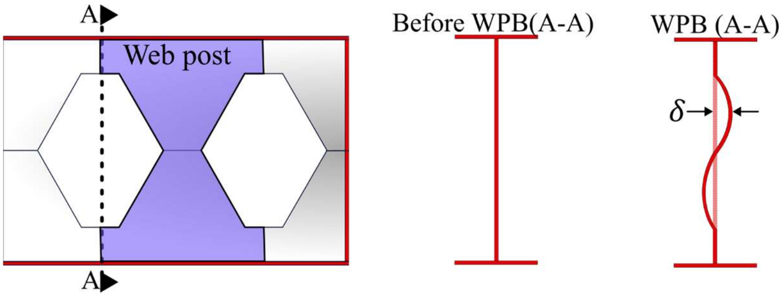

a) Schematic of the WPB mode before and after failure.

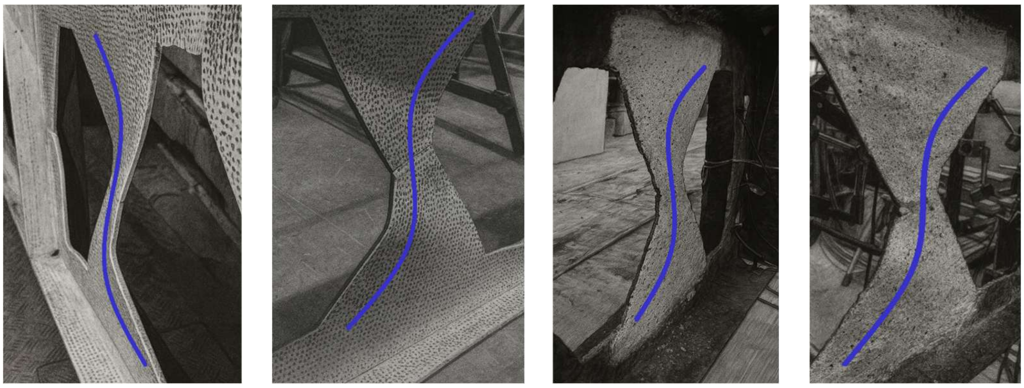

b) G50-NC. c) G60-NC. d) G50-C. f) G60-C.

Source: The author (2026)

Figure 31 presents the load-displacement curves of corroded and non-corroded beams, along with the strain measurements at midspan, for both steel Grades. Corroded beams exhibited initial flexural stiffness similar to non-corroded ones because the area of the flanges, which governs vertical displacement together with the modulus of elasticity, was less impacted by corrosion due to their higher thickness compared to the web (Zhang *et al.*, 2021). The strains developed at midspan confirm the hypothesis of WPB because no point exceeded the steel yield strain: 1725 με for Grade 50 and 2075 με for Grade 60. Also, there was no evidence of local buckling or lateral-torsional buckling at midspan. For the corroded beams, the reduction in web thickness resulted in a 39.05% reduction in beam capacity for Grade 50 steel and a 35.85% reduction for Grade 60. The corrosion pits on the steel surface create localized stress concentrations (Luo *et al.*, 2024; Sheng; Xia; Ma, 2018), making the web susceptible to local buckling failure of the beam (Zhang *et al.*, 2021). Therefore, the pit corrosion reduced the stiffness of the web strut that governs the beam capacity, explaining the significant capacity loss. This phenomenon is experimentally evidenced later in the DIC strain maps (Figure 33), which reveal strain localization and early yielding around the corrosion pits.

Figure 31 - Curve load x displacement and strain of midspan section.

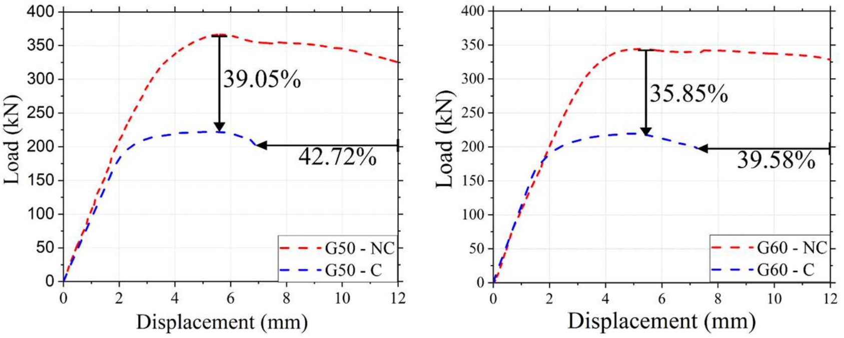

a) Load - displacement Grade 50.

d) Load - displacement Grade 60.

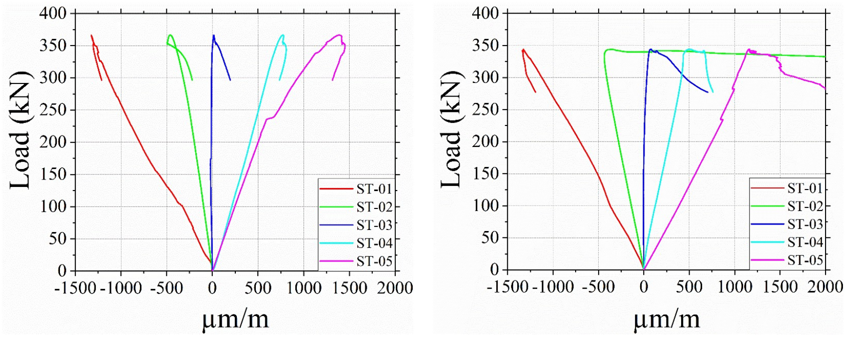

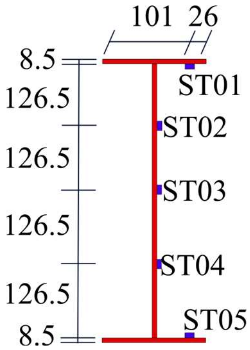

b) Strain G50-NC.

e) Strain G60-NC.

g) Strain gauge layout at midspan (unit: mm)

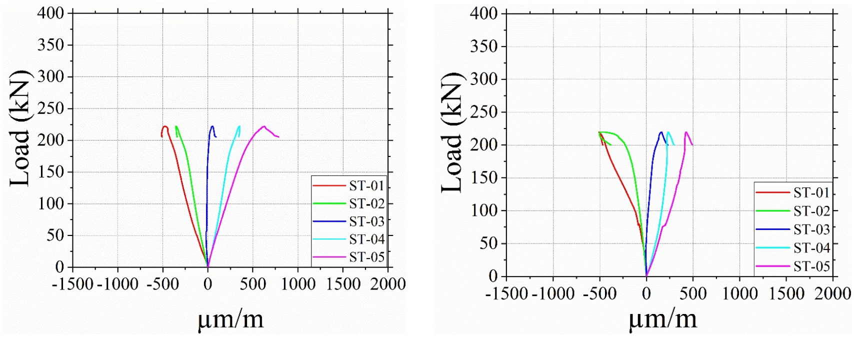

c) Strain G50-C.

f) Strain G60-C.

Source: The author (2026)

The WPB mechanism was further analyzed by comparing the lateral displacement profiles and strain fields of both non-corroded and corroded beams using DIC. Figure 32 presents the evolution of lateral displacements along the web height under increasing load levels, from 50 kN to the ultimate load, together with the corresponding DIC displacement maps and the lateral load-displacement curves. Figure 32a and 32b correspond to the non-corroded beams G60-NC and G50-NC, whereas Figure 32c and 32d refer to the corroded beams G60-C and G50-C, respectively. The DIC displacement fields confirm the characteristic sinusoidal shape of the compressed strut and show that, after buckling, the strut becomes aligned with the opening edge. The load-displacement curves indicate that the lateral displacement magnitude was considerably higher and occurred at much lower load levels for corroded beams compared with the non-corroded ones (Zhang *et al.*, 2021). This response is attributed to localized stress concentrations around corrosion pits, later evidenced in Figure 33, which reduced the web stiffness and promoted earlier yielding, leading to increased slenderness and deformation demand.

Nevertheless, the overall buckling mode remained similar, and the effect of steel grade was negligible since WPB was mainly governed by the elastic properties of the steel and the web geometry (Redwood; Demirdjian, 1998; Zaarour; Redwood, 1996). It should be noted that the rotation is free at the web mid-depth and is partially restricted when near the flange for both corroded and non-corroded beams. This strut configuration will be adopted in the analytical model.

Figure 32 - Lateral displacement along web-post height under different loading levels, DIC displacement fields, and load-lateral displacement registering the WPB.

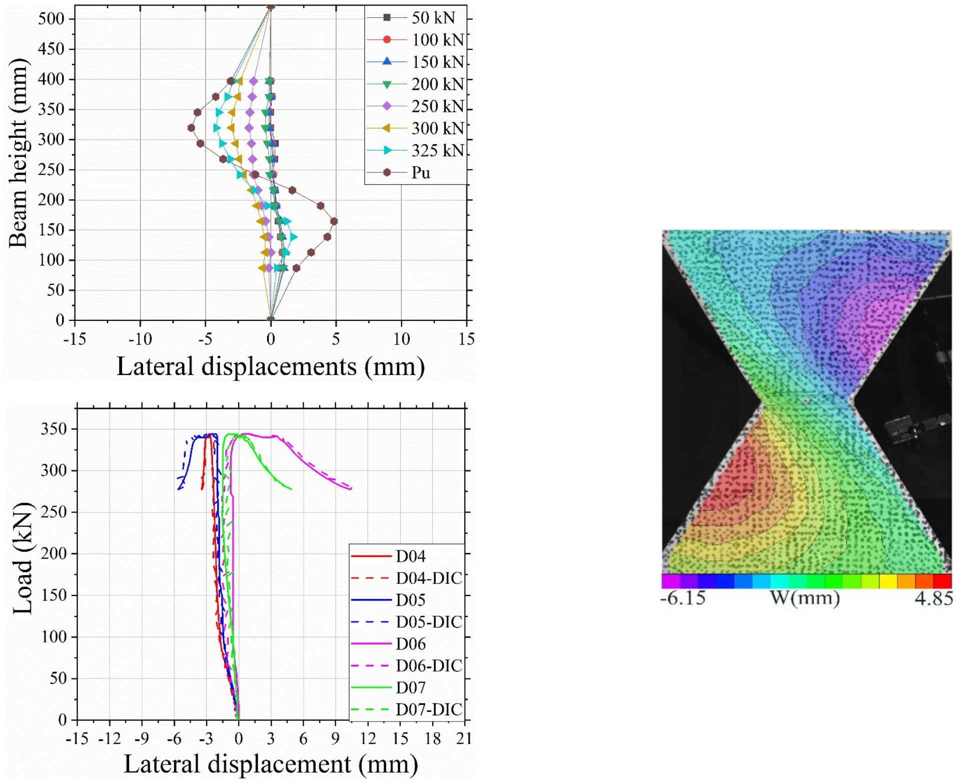

a) G60-NC

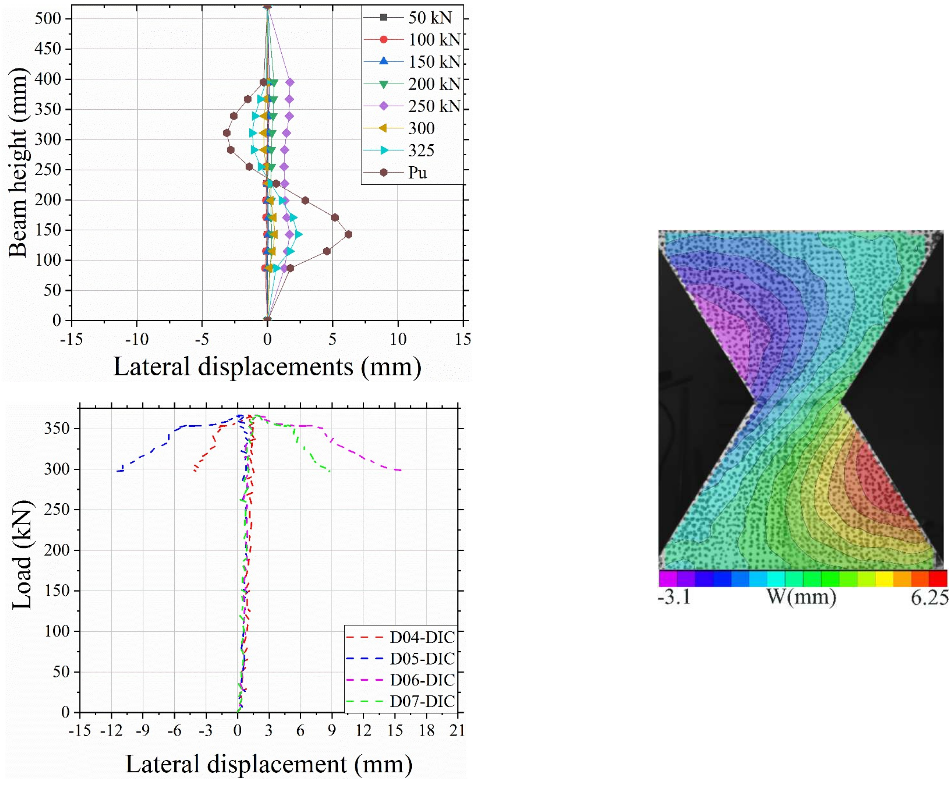

b) G50-NC

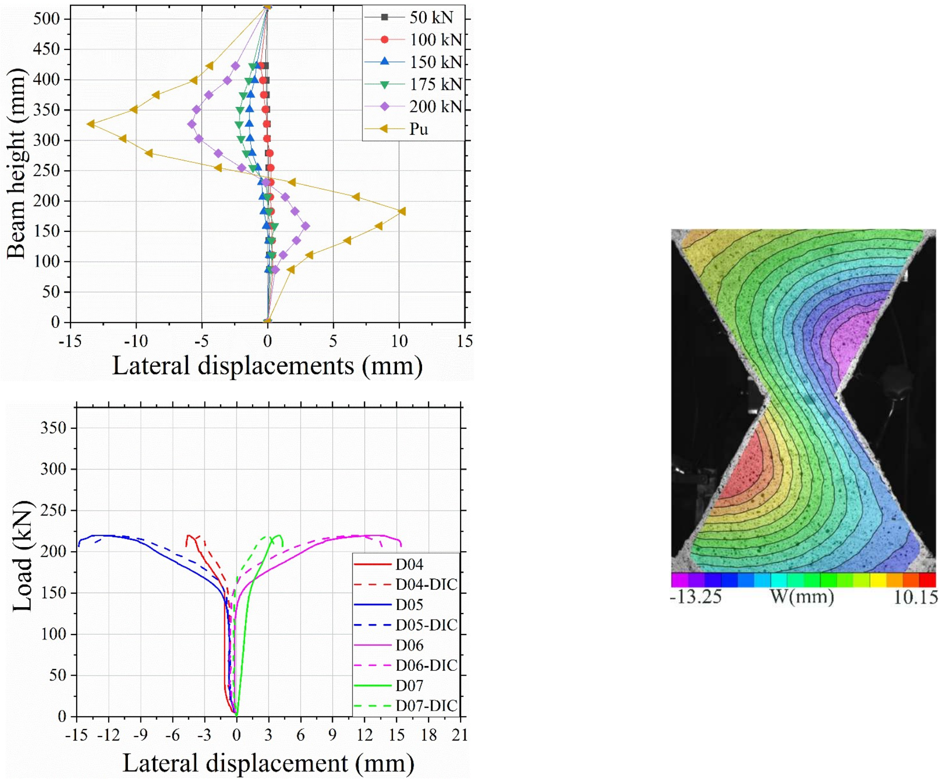

c) G60-C.

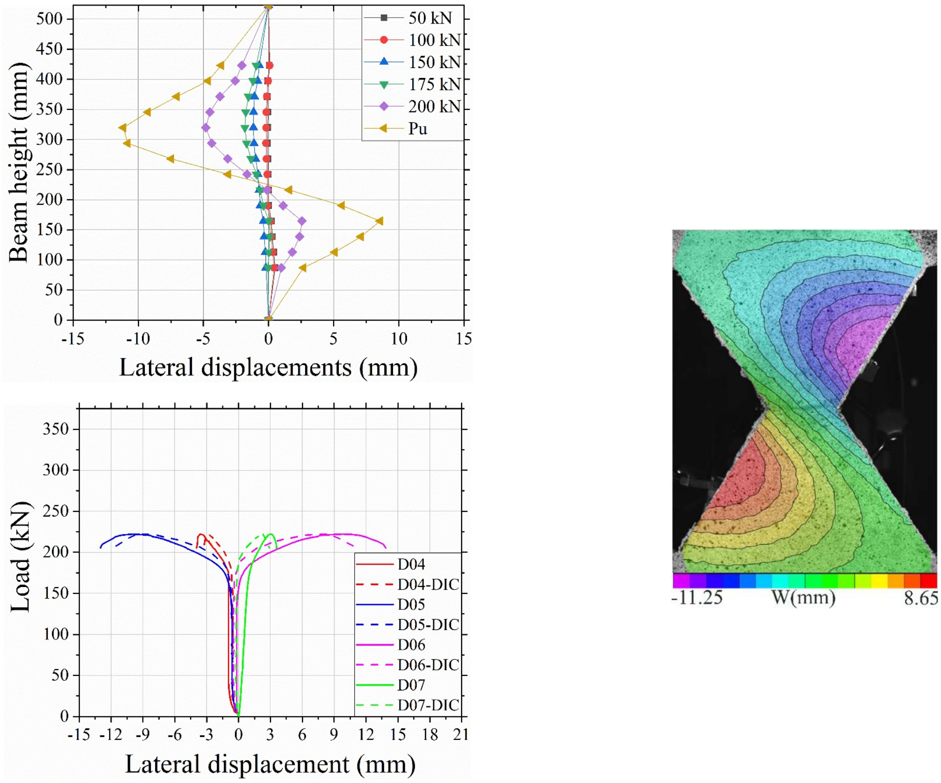

d)G50-C.

Source: The author (2026)

To further elucidate the post-buckling behavior, the principal tensile strain maps were analyzed, as shown in Figure 33, corresponding to the load levels at which yielding initiated in the web. Compressive strains were intentionally omitted for clarity, emphasizing the inclined tensile tie mechanism that balances the compressive strut. The onset of yielding occurred at approximately 245–248 kN for the non-corroded beams (G50-NC and G60-NC) and at nearly half of that load (113–117 kN) for the corroded counterparts (G50-C and G60-C), evidencing the substantial loss of load-carrying capacity caused by corrosion-induced section reduction. The strain maps confirm that steel yielding governs the ductile post-buckling response (Kerdal; Nethercot, 1984). In corroded beams, localized strain concentrations around corrosion pits highlighted with white circles in Figure 33b and d indicate stress intensification and premature yielding of the tensile tie, whose reduced cross-section limits its load-carrying capacity. Thus, the struts buckle and the ties yield earlier in corroded beams, together with smaller longitudinal strains at midspan compared with the non-corroded specimens (Xiao; Chen; Peng, 2024).

Figure 33 - Strain patterns of the web tie in the post-buckling regime and loadings.

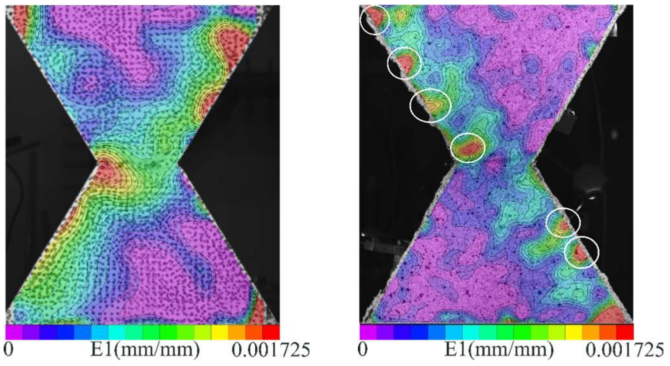

a) G50-NC; load =245kN. b) G50-C; load =113kN.

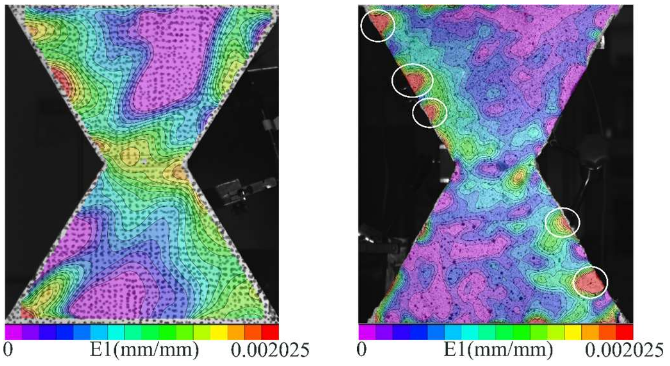

c) G60-NC; load =248kN.   d) G60-C; load =117kN.

Source: The author (2026)

Figure 34a and 34b illustrate the surface of a Grade 60 beam web-post before and after corrosion, emphasizing how pitting corrosion reduces the cross-sectional area of the beam. For the Grade 50, the total weight of the beam decreased from 77.8 kg to 66.7 kg, while for the Grade 60 beam, it reduced from 78.9 kg to 66.4 kg, corresponding to weight reductions of 14.26% and 15.84%, respectively. Also, Figure 34c, 34d, and 34e present the mass loss and the stress–strain curves for the corroded coupons, calculated based on the nominal section of the specimen (Imperatore; Rinaldi; Drago, 2017; Ou; Susanto; Roh, 2016). These results further highlight the cause of the ductility reduction observed in the corroded beam that failed due to WPB.

Figure 34 - Corrosion effects on steel: appearance, mass loss, and stress-strain curve.

a) G60-NC   b) G60-C

Source: The author (2026)

3.5.4 **Pit measurements**

Pit shape and dimensions were determined using DIC to quantify the severity of corrosion at the web prior to the bending tests. Pitting corrosion initiates at surface imperfections with localized metal dissolution, forming circular or near-circular pits with shiny bases (Imperatore; Rinaldi; Drago, 2017; Melchers, 2018). As corrosion progresses, corrosion products accumulate over the pits, isolating their interiors and creating acidic, anoxic micro-environments that promote further deepening until the electrochemical potential is depleted. The pit shape gradually evolves into a hemispherical geometry through lateral growth, and once depth propagation ceases, lateral expansion and coalescence occur, producing broader depressions with scalloped or dimpled floors (Melchers, 2018). Figure 35a presents the three-dimensional DIC surface, where the X and Y axes represent the horizontal coordinates of the analyzed surface (in millimeters), and the Z axis corresponds to the out-of-plane displacement (in millimeters), quantifying the surface elevation variations associated with corrosion pitting. The corresponding two-dimensional contour map in Figure 35b, with extraction lines (A–C) indicating the pitting patterns, illustrates this behavior, while the surface profiles along these lines, Figure 35c, reveal localized depth variations associated with individual corrosion pits. Pitting patterns observed in profiles B and C display a peak between two valleys, suggesting that during the anoxic stage lateral growth occurs. New pits may nucleate on these surfaces, leading to cyclic and stepwise depth increases. Pit depth was quantified using 16 surface profiles extracted with VIC-3D (Figure 35b), from which six representative profiles in horizontal, vertical, and diagonal directions were selected for detailed analysis.

Figure 35 - Measurement of pit depth.

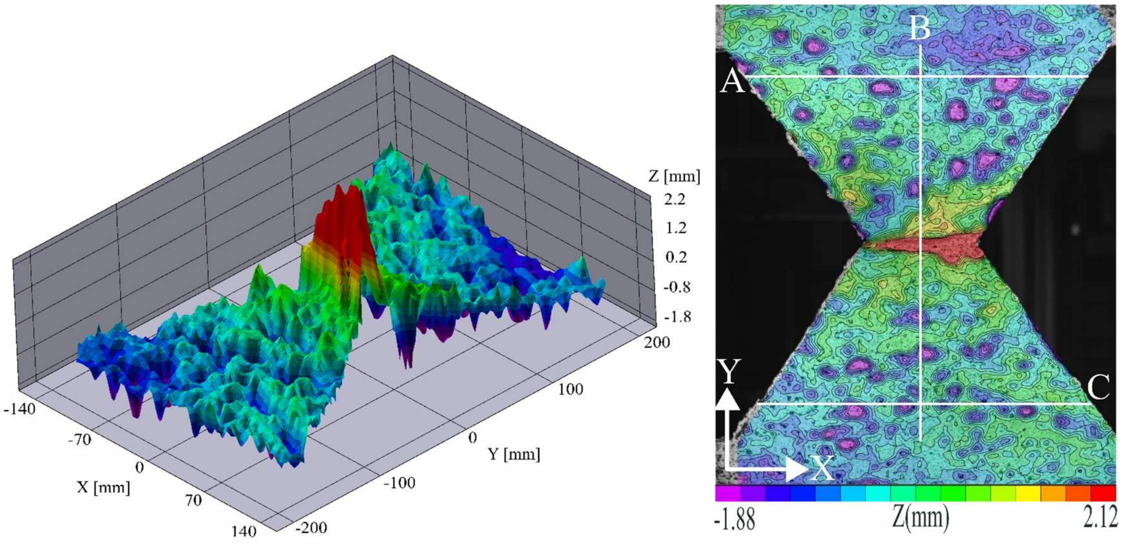

a) 3D DIC surface of G50-C

b) 2D surface of G50-C and lines (A–C)

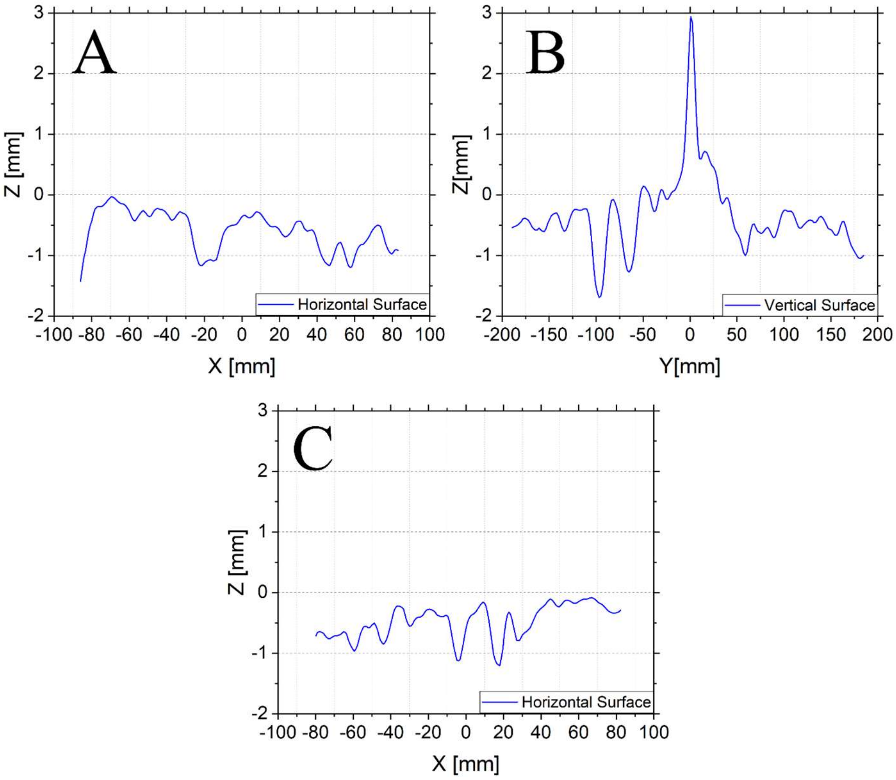

c) Surface profile showing pitting pattern (A-C)

Source: The author (2026)

The log-normal distribution of pit depth reflects the stochastic and multiplicative nature of localized corrosion processes, highlighting the progressive deterioration of the steel surface over time and the inherent variability caused by micro-environmental heterogeneities and localized electrochemical conditions (Wang *et al.*, 2024; Yamamoto; Ikegami, 1998). As shown in Figure 36a and 36b, the pit depth follows a log-normal distribution, with a logarithmic mean of 0.7951 mm and a SD of 0.3865 mm for Grade 50 steel, while for Grade 60 steel, the corresponding values are 0.8918 mm and 0.4636 mm, respectively.

Figure 36 – Log-normal distribution of pit depth for steels.

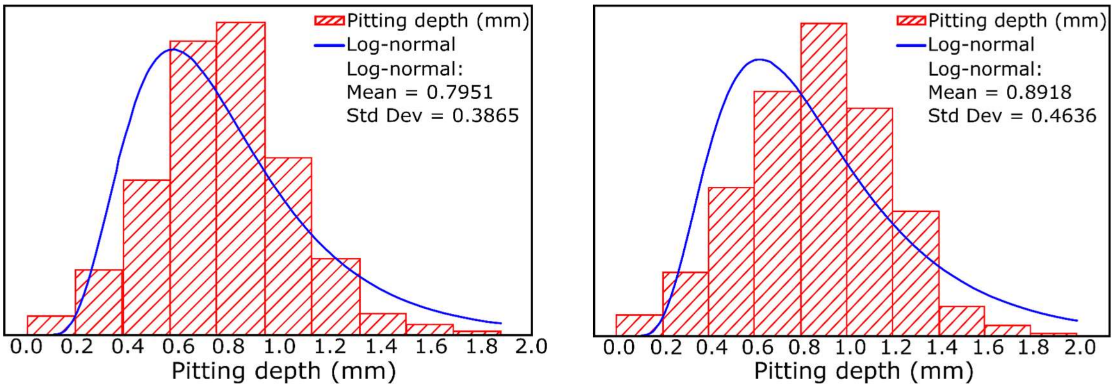

a) Log-normal distribution of pit depth – Grade 50

b) Log-normal distribution of pit depth – Grade 60

Source: The author (2026)

The statistical characterization of pit depth provides the basis for the subsequent structural modelling developed in this study. Based on the pit measurements obtained from the corroded specimens and their log-normal statistical distribution, two modelling strategies are adopted in the following chapters. First, an analytical formulation is developed to evaluate the structural behavior of castellated beams subjected to web-post buckling, explicitly considering the influence of localized thickness loss produced by corrosion pits. In parallel, a numerical modelling strategy is implemented for solid web beams using finite element analysis, in which the pit statistics are incorporated to represent the non-uniform reduction of thickness along the beam surface. These approaches allow the experimental characterization of pitting corrosion to be directly linked with the structural response of both beam configurations, enabling a consistent interpretation of the influence of corrosion on stiffness degradation, instability development, and ultimate load-carrying capacity.

CHAPTER 4 - ANALYTICAL MODELS

This section presents the proposed non-empirical equation for the WPB resistance of corroded castellated steel beams. The formula is also valid for non-corroded elements, thereby being compared against experiments and procedures based on Steel Design Guide 31 (Sameer S. Fares; Coulson; David W. Dinehart, 2016) and EN 1993-1-13:2024 (Eurocode 3, 2024).

4.1 STEEL DESIGN GUIDE 31

The Steel Design Guide 31 (Sameer S. Fares; Coulson; David W. Dinehart, 2016) adopts the approach proposed by Aglan and Redwood (Aglan; Redwood, 1974) to determine the WPB resistance of castellated beams. This methodology considers the horizontal shear force (V_{rh}) acting on the web-post between openings i and $i+1$, as illustrated in Figure 37**.** The figure presents key parameters, including the shear force at the opening ($V_{r(i)}$), axial force at the centerline of the opening ($T_{r(i)}$), bending moment (M_i), the distance from the geometric center of the tee to its welded edge (y_o), the distance between centroids of top and bottom tees (d_{effec}).

Figure 37 - Model adopted by the Steel Design Guide 31.

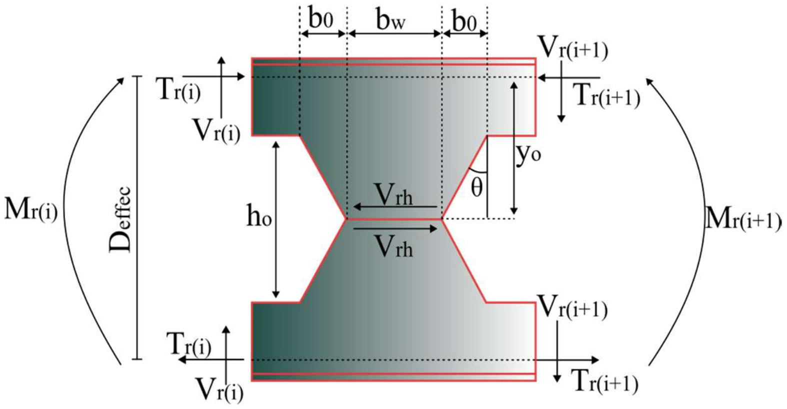

Source: The author (2026)

The horizontal shear force (V_{rh}) is determined using Equation 01.

$$V_{rh} = \left| \frac{M_{r(i+1)} - M_{(i)}}{d_{effec}} \right| \tag{01}$$

It is worth mentioning that the proposition is limited to the following conditions: $45° \leq \theta \leq 60°$, $10 \leq b_w/t_w \leq 30$, and $h_o/b_w \leq 8$. In this method, the plastic bending moment is calculated through Equation 02.

$$M_{W,p} = 0.25t_w(b_w + 2b_0)^2 f_y \tag{02}$$

For Anglo-Saxon castellated beams with an opening angle of 60°, the WPB resistance is determined using Equations 03, 04, and 05, where the ratio $b_w/t_w=10$, the $M_{W,Rk}/M_{W,p}$ is limited to 0.493. For intermediate values of b_w/t_w, interpolation between the equations is allowed.

$$\text{If } b_w/t_w = 10,\ M_{W,Rk} = M_{W,p}\left[0.587(0.917)^{\frac{h_o}{b_w}}\right] \leq 0.493M_{W,p} \tag{03}$$

$$\text{If } b_w/t_w = 20,\ M_{W,Rk} = M_{W,p}\left[1.96(0.699)^{\frac{h_o}{b_w}}\right] \tag{04}$$

$$\text{If } b_w/t_w = 30,\ M_{W,Rk} = M_{W,p}\left[2.55(0.574)^{\frac{h_o}{b_w}}\right] \tag{05}$$

4.2 EN 1993-1-13:2024

To determine the WPB resistance of steel castellated I-beams, EN 1993-1-13:2024 (Eurocode 3, 2024) presents a formulation based on the effective length of the compressed web-post, which varies according to the opening geometry. In compliance with this standard, the axial force in the web-post ($N_{wp,Ed}$) must meet the following condition:

$$\frac{N_{wp,Ed}}{N_{wp,Rd}} \leq 1.0 \tag{06}$$

Where $N_{wp,Rd}$ represent the WPB resistance. According to EN 1993-1-13:2024 (Eurocode 3, 2024), for this verification, the compressive force in the web-post ($N_{wp,Ed}$) should be assumed to be equivalent to the horizontal shear force ($V_{wp,Ed}$), which is calculated using Equation 07.

$$N_{wp,Ed} = V_{wp,Ed} \tag{07}$$

The WPB resistance ($N_{wp,Rd}$) should be taken as:

$$N_{wp,Rd} = \chi_{wp} b_w t_w f_y \tag{08}$$

The minimum value obtained by multiplying the web thickness (t_w) and the yield strength (f_y) of the top and bottom tees, considered separately, must be used. Furthermore, the reduction factor χ_{wp} should be determined using the buckling curve from EN 1993-1-1:2022 (Kuhlmann *et al.*, 2021) for all steel grades, considering the relative slenderness of the web-post (λ_{wp}), as given by Equations 09 and 10.

$$\lambda_{wp} = \frac{1.75\sqrt{2{b_w}^2 + {h_o}^2}}{t_w} \frac{1}{\lambda_1} \leq \frac{2.7 h_o}{t_w} \frac{1}{\lambda_1} \tag{09}$$

$$\lambda_1 = \pi \sqrt{\frac{E}{f_y}} \tag{10}$$

4.3 PROPOSED MODEL

The web buckling was modeled as the compression field of the web-post, considering its axis parallel to the opening edge, as shown in Figure 38a. The supports were hinged at mid-depth and semi-rigid near the flange. Corrosion was accounted for by considering a periodic variation of the web thickness (t_w), depicted in Figure 38b and 38c.

The figure isolates half of the strut length, and the minimum depth is t_w minus two times the pit depth (c). The rotational stiffness for the strut was calculated considering the web between the opening and the flange as a cantilever beam, which results in $k_\theta = E \times I / L_b$, where EI is the same as the strut and L_b is the distance between the flange and the opening. k_θ represents the rotational stiffness of a cantilever beam fixed at the flange. The dimensionless spring stiffness β is determined from Equation 11 and its value associated with the buckling mode $\beta(\varphi)$, as presented in Figure 38a, is represented by Equation 12.

$$\beta = \frac{k_\theta L_b}{EI} \tag{11}$$

$$\beta = \frac{\varphi^2 sin\varphi}{\varphi cos\varphi - sin\varphi} \tag{12}$$

The numerical solution for Equation 2, valid for $1 \leq \beta \leq 20$, is Equation 13.

$$K(\beta) \approx 0.7 + \frac{0.8}{\beta + 2.6} \tag{13}$$

Substituting β from Equation 1 in Equation 3 results in K approximately 0.9.

Figure 38 - Hypothesis for the strut at the web.

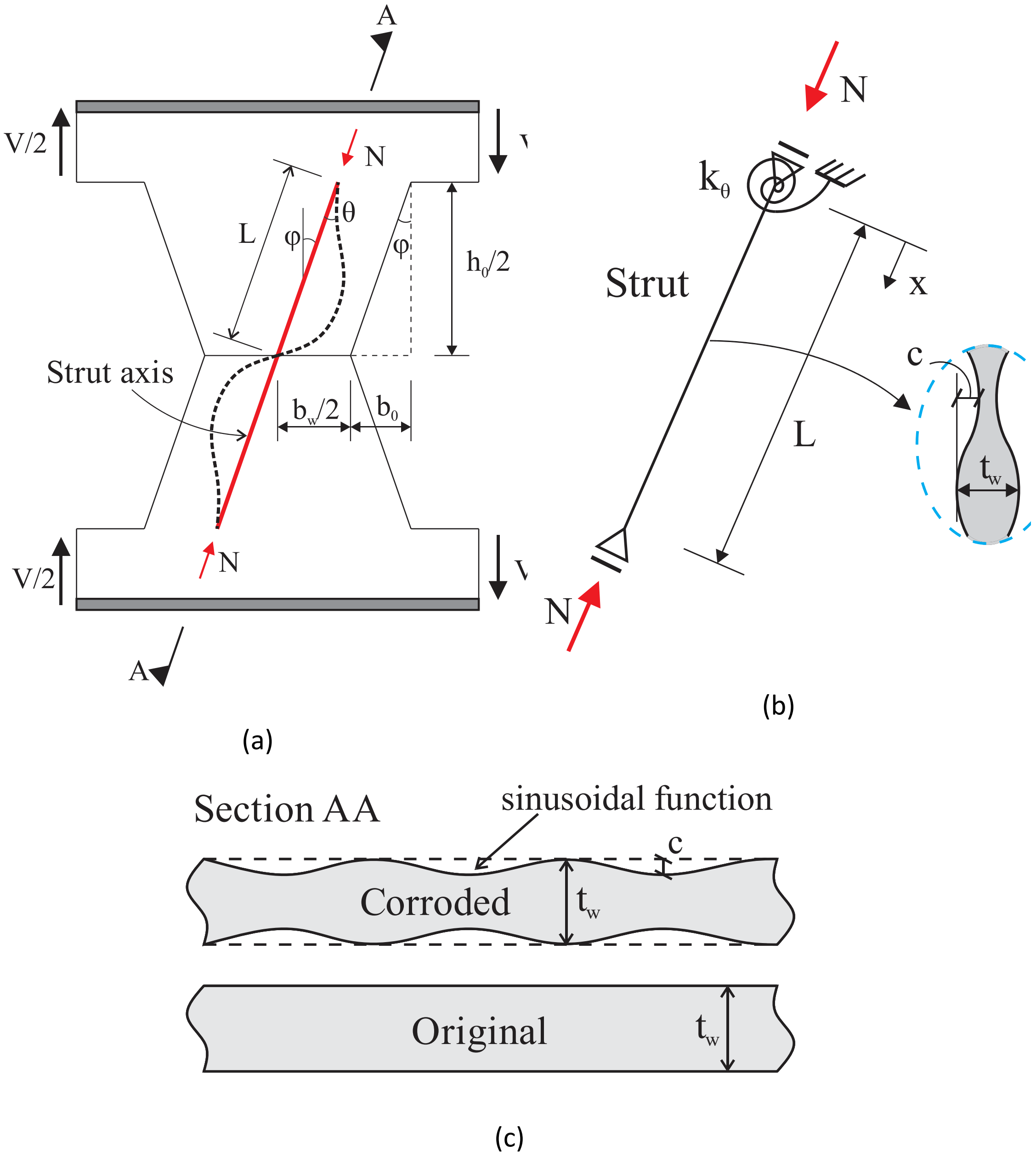

Source: The author (2026)

The compressed element was considered parallel to the edge of the web opening, with an inclination φ, as evidenced by DIC. The opening edge is about 60° for Anglo-Saxon beams. A plane stress finite element model of the web was also developed to understand the behavior of the strut. The principal compressive stresses and directions resulting from the shear load are plotted, as shown in Figure 39. The strut inclination was confirmed to be φ parallel to the web edge. Therefore, the strut length was determined by Equation 14. The value of K represents the coefficient for the buckling length.

$$L = \sqrt{\left[b_0^2 + \left(\frac{h_0}{2}\right)^2\right] \times K} \tag{14}$$

Figure 39 - Strut inclination and width adopted from stress analysis.

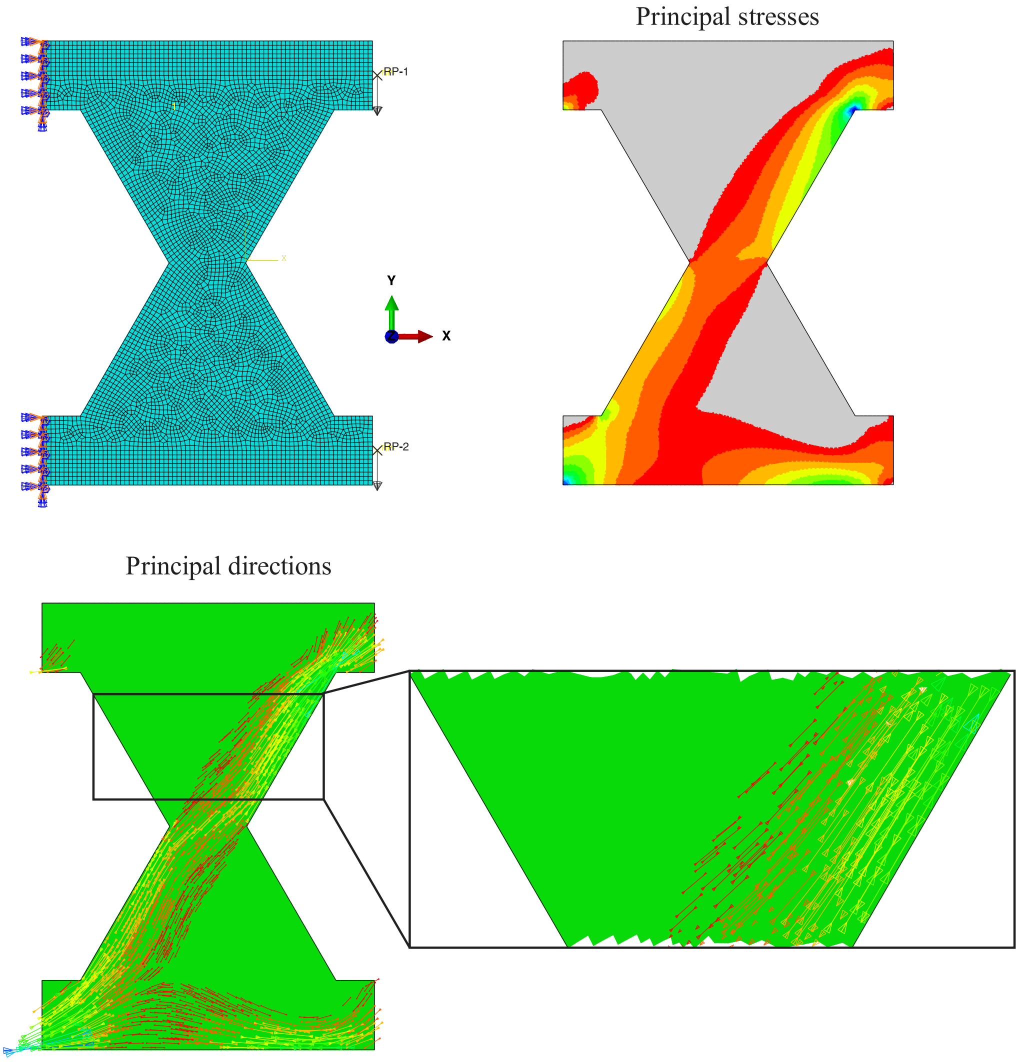
Principal stresses

Principal directions

Source: The author (2026)

The strut was considered to maintain the rectangular section, but with variable thickness, modeled as a sine function described by Equation 15, represented in Figure *38*c. Seeing the profiles of the corroded surface, Figure 35, it is a reasonable approximation considering this function, also the volume reduction considering this equation is 13.79%, which is close to the experimental reductions. The maximum value is the original web t_w, and the minimum is t_w minus two times the *c*.

$$h(x) = t_w - 2c \sin^2\left(\frac{n\pi x}{L}\right) \tag{15}$$

Obtaining the average moment of inertia, $I_m = \frac{b}{12L}\int_0^L h^3(x)dx$, results in Equation 16, dependent on the pit *c*, but independent of the period *L/n*, because the function is periodic and the average represents a uniform reduction of the web thickness.

$$I_m = \frac{b}{24}(2t_w^3 - 6t_w^2 c + 9t_w c^2 - 5c^3) \tag{16}$$

The strut width is the projection of the web-post width at the middle of the height in the direction perpendicular to the strut axis, $b = b_w \cos(\varphi)$, and the relation between the shear load V and an axial buckling load is described by Equation 17.

$$V_{crit} = 2N_{crit} \cos\varphi \tag{17}$$

The load N_{crit} was calculated considering the buckling of a simple supported column as depicted in Figure *38*. The problem is solved by minimizing the energy functional, applying the Rayleigh-Ritz method (Equation 18).

$$\begin{gathered} \Pi = U - V \\ \frac{\partial \Pi}{\partial \mathrm{a}_i} = 0 \end{gathered} \tag{18}$$

Where *U* is the flexural deformation energy, justified by the lateral displacements of the web, and *V* is the potential energy of external loads. ai are the constants of the approximation function *v(x)*, which is $v(x) = a1 \sin(\pi x/L)$, *L* is the strut length. The displacement function *v(x)* respects the boundary conditions for a simply supported column $(v(0) = 0,\ v(L) = 0)$. Solving the minimization problem with Equations 16, 17, and 18 results in the non-empirical formula of the shear load for web buckling, as shown in Equation 19.

$$V_{crit} = \frac{\pi^2 E\, b_w {h_0}^2 (2t_w^3 - 6t_w^2 c + 9t_w c^2 - 5c^3)}{3K^2(4b_0^2 + h_0^2)^2} \tag{19}$$

Where *E* is the elastic modulus of steel, and h_0 is the web opening height. It should be noted that the equation predicts the critical shear load for non-corroded beams when $c = 0$.

The Southwell equation (Krahl; Carrazedo; El Debs, 2018; Southwell, 1932) is applied to accounting for initial imperfection on the WPB.

$$\delta = \frac{\delta_0}{1 - \left(\frac{V}{V_{crit}}\right)^2} \tag{20}$$

Where δ_0 is the initial imperfection, taken as a local imperfection of L/1000 (De Oliveira *et al.*, 2025), V_{crit} is the result of equation (19), and V and δ are the ordinate and absicissa of the load displacement curve, respectively. Equation (20) provides the geometrical nonlinear response of a strut when the V_{crit} and δ_0 are known, allowing the comparison with experimental results of web lateral displacements and applied load.

4.4 ANALYTICAL PREDICTIONS RESULTS

The model variables were considered as random variables following specific code-recommended distributions for material properties, geometric parameters, and corrosion characteristics. The selected variables include the elastic modulus of steel (E), yield strength (f_y), web-post width (b_w), web thickness (t_w), opening height (h_o), and pit depth (c), the latter being zero for non-corroded beams. Coefficients of variation (CV) and probability distributions were defined based on the recommendations of the Joint Committee on Structural Safety (JCSS) (Joint Committee on Structural Safety, 2001), ensuring an adequate representation of the uncertainties inherent to physical and geometric properties. Table 3 presents the adopted variables along with their probability distributions, mean values, and CV.

Table 3 - Random variables.

Variable	Unit	Distribution	Mean	CV	Reference
E	MPa	Log-normal	200,000	4%	JCSS(Joint Committee on Structural Safety, 2001)
f_y	MPa	Log-normal	345 (Grade 50) 415 (Grade 60)	7%	
b_w	mm	Normal	87	3.2%	
t_w	mm	Normal	5.8	3.2%	
h_o	mm	Normal	349	3.2%	

c(pit)	mm	Log-normal	0.7951 (Grade 50) 0.8918 (Grade 60)	0.4636 0.3865	Present study

Source: The author (2026)

4.4.1 Non-corroded castellated beams

To evaluate the shear capacity of non-corroded beams, 500,000 simulations were performed for each design approach: EN 1993-1-13:2024 (Eurocode 3, 2024), *Steel Design Guide 31* (Sameer S. Fares; Coulson; David W. Dinehart, 2016), and the proposed model, considering the probabilistic distributions and CV listed in Table 3. The experimental shear strength V_{crit} = 133.36 kN for the Grade 50 steel beam and V_{crit} = 125.69 kN for the Grade 60 steesl beam were used as reference values for comparison. The boxplots in Figure 40a and 40c summarize the distribution of the simulated shear capacities for each approach. EN 1993-1-13:2024 (Eurocode 3, 2024) presents conservative predictions with mean values of 47.1% and 43.9% below the experimental, respectively. Therefore, *Steel Design Guide 31* (Sameer S. Fares; Coulson; David W. Dinehart, 2016) reduces this gap (31.2% and 22.1%), but still underestimates the experimental capacity. Conversely, the proposed model provides predictions closer to the experimental results (8.5% and 2.9%). Figure 40b and 40d present theoretical $V(\delta)$ curves obtained by selecting, in each case, 10 random values of V_{crit} from the 500,000 simulations, together with the experimental results. In both figures, the experimental response falls within the predicted geometric nonlinear curves using Equation (10), demonstrating that the model provides a reliable range for the expected structural behavior.

Figure 40 - Box plots of shear load predictions vs experiments.

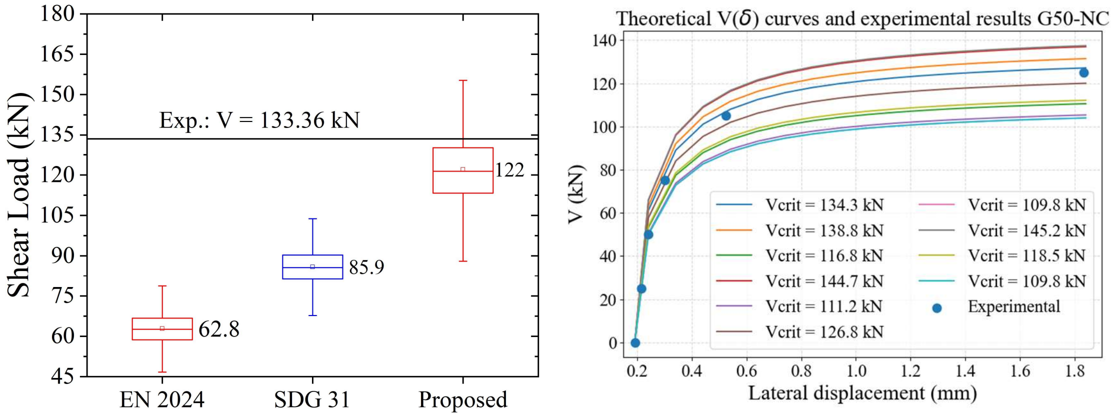

a) Boxplot G50-NC.

b) Southwell curves for beam G50-NC.

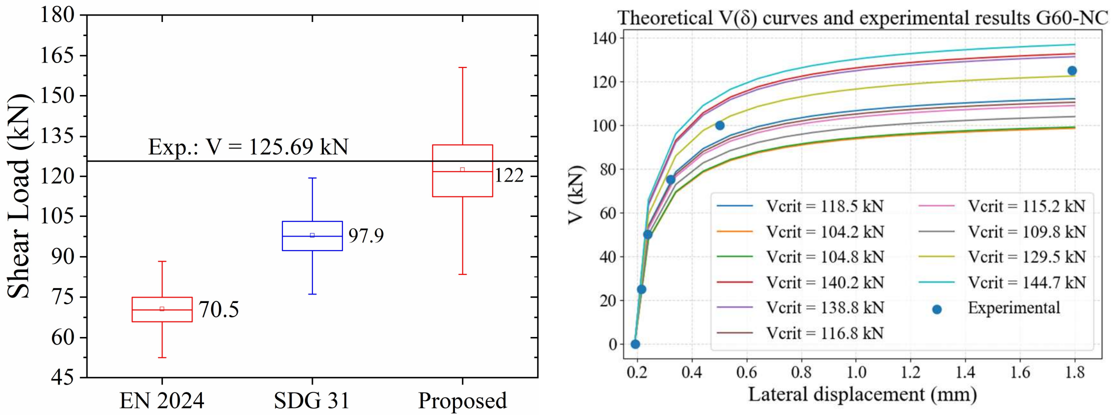

c) Boxplot G60-NC.

d) Southwell curves for beam G60-NC.

Source: The author (2026)

As expected, accounting for imperfection changes from a bifurcation problem to a nonlinear response. The curve starts at the initial imperfection (L/1000 (De Oliveira *et al.*, 2025)), the initial stiffness of the web is well predicted, and at maximum load, the pattern is asymptotic to the critical buckling load (Equation (9)), when displacement tends towards infinity. This trend means that the limit load V, obtained with the Southwell expression (Equation (10)), will be smaller than the critical load, which resulted in very good accuracy with the assumed hypothesis.

In addition, Table 4 presents a comparison with prediction formulations and experimental results reported by previous research investigations on the WPB non-corroded castellated beams investigation (Redwood; Demirdjian, 1998; Vieira, 2015; Zaarour; Redwood, 1996), all with web opening inclinations of 60°, compared with predictions from EN 1993-1-13:2024 (Eurocode 3, 2024), *Steel Design Guide 31*(Sameer S. Fares; Coulson; David W. Dinehart, 2016), and the proposed model. EN 1993-1-13:2024 (Eurocode 3, 2024) provided the most conservative predictions, underestimating the experimental results by 40.8% on average. In contrast, *Steel Design Guide 31* (Sameer S. Fares; Coulson; David W. Dinehart, 2016) tended to overestimate the critical shear load by an average of 17.4%, particularly due to its strong dependence on the yield strength. The proposed model also showed a better agreement with literature results, with predictions deviating on average by 7%. Geometric imperfections were not considered in these predictions because the web lateral displacement was not reported in references.

Table 4 - Comparison between experimental and prediction formulations.

Reference	$V_{cr,TEST}$	$V_{cr,EN\ 2024}$	$V_{cr,\ EN\ 2024}/V_{cr,TEST}$	$V_{cr,SDG31}$	$V_{cr,SDG31}/V_{cr,TEST}$	$V_{cr,\ proposed\ model}$	$V_{cr,\ proposed\ model}/V_{cr,TEST}$
10-5(a) (Redwood; Demirdjian, 1998)	46.35	25.14	0.55	68.97	1.49	46.65	0.98
10-6(Redwood; Demirdjian, 1998)	47.1	25.14	0.54	68.97	1.46	46.65	0.97
10-7(Redwood; Demirdjian, 1998)	42.2	25.14	0.60	68.97	1.63	46.65	1.08
8-1(Zaarour; Redwood, 1996)	28.4	20.67	0.73	35.99	1.27	34.18	1.20
8-2(Zaarour; Redwood, 1996)	24.91	14.74	0.59	25.45	1.02	28.97	1.16
10-1(Zaarour; Redwood, 1996)	39.5	23.03	0.59	44.19	1.12	41.03	1.04
10-2(Zaarour; Redwood, 1996)	29.36	17.13	0.58	35.29	1.20	33.67	1.15
12-1(Zaarour; Redwood, 1996)	57.28	32.66	0.57	65.45	1.14	56.05	0.98
12-2(Zaarour; Redwood, 1996)	49.15	26.56	0.54	44.26	0.90	45.87	0.93

B1(Vieira, 2015)	126.50	76.53	0.60	97.78	0.77	147.52	1.17
B2(Vieira, 2015)	89.70	55.25	0.62	82.22	0.91	101.24	1.13

Source: The author (2026)

To better understand the influence of each parameter, this study evaluates the Pearson correlation coefficient for the 500,000 input–output parameter pairs. This approach quantifies the individual influence of the variables listed in Table 3 on each standard.

Figure 41 presents the Pearson coefficients for the variables of each model. Variables shown in blue exhibit a positive relationship with V_{crit}, meaning that an increase in these parameters tends to increase the predicted resistance. In contrast, the red bar represents a variable with a negative correlation, indicating that higher values lead to a reduction in V_{crit}. In the Steel Design Guide 31(Sameer S. Fares; Coulson; David W. Dinehart, 2016), f_y resulted in a very strong positive correlation (0.7 to 0.9) with V_{crit}, and a moderate positive (0.3 to 0.5) for t_w. For Eurocode, a very strong positive correlation was found for t_w a moderate negative (-0.5 to -0.3) to h_0, and a moderate positive (0.3 to 0.5) for E. In the present study, t_w had a very strong positive correlation, followed by the modulus of elasticity with a moderate positive correlation. Notably, both the Eurocode and the present model highlighted parameters directly related to web slenderness, as t_w and h_0, which, from experimental evidence, govern the WPB behavior characteristic of castellated beams. It should be mentioned that increasing the yield strength does not increase the buckling capacity, as suggested by the model in *Steel Design Guide 31* (Sameer S. Fares; Coulson; David W. Dinehart, 2016). Additionally, b and h_0 represent the strut length, and their increase indicates greater slenderness, consistent with the negative correlation. In contrast, the web slenderness decreases as the quantities b_w and t_w increase, explaining the positive correlations.

Figure 41 - Pearson correlation of variables.

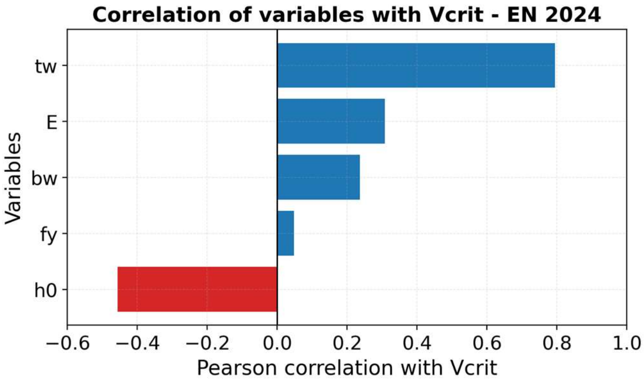

a) EN 1993-1-13:2024 (Eurocode 3, 2024).

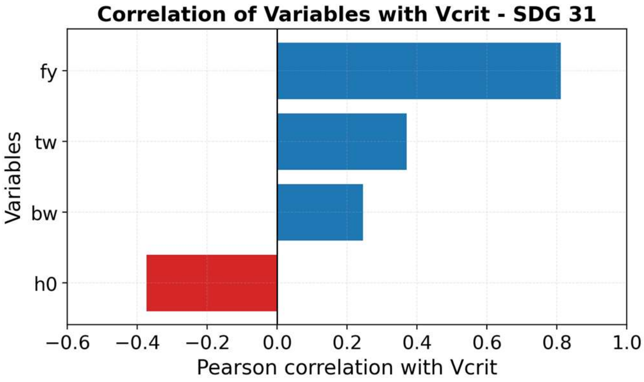

b) Steel Design Guide 31.

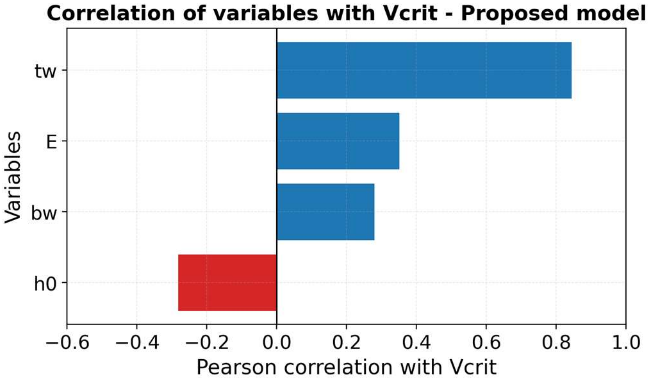

c) Proposed model.

Source: The author (2026)

4.4.2 **Corroded castellated beams**

Figure 42a presents the box plots for the shear capacity of corroded beams representing the distribution of the 500,000 simulations performed using the proposed model, and a log-normal distribution for pit depth. The experimental shear loads (V = 81.25 kN and V = 80.13 kN) were indicated by horizontal lines, for comparison. The average errors of overestimation were approximately 1.53% (G50-C) and 1.91% (G60-C). The distribution seen in the boxplots suggests that considering the maximum pit observed in the equation would result in a conservative prediction. Figure 42b and 42c present the theorical curves applying Equation (10) for beams G50-C and G60-C. For each beam, 10 V_{crit} values were randomly selected from the 500,000 simulations and used to generate the $V(\delta)$ curves.

Figure 42 - Shear load predictions: model vs. experimental results.

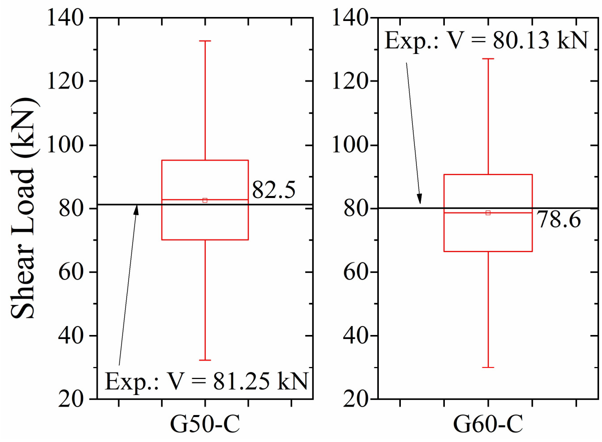

a) Boxplot G50-NC and G60-NC.

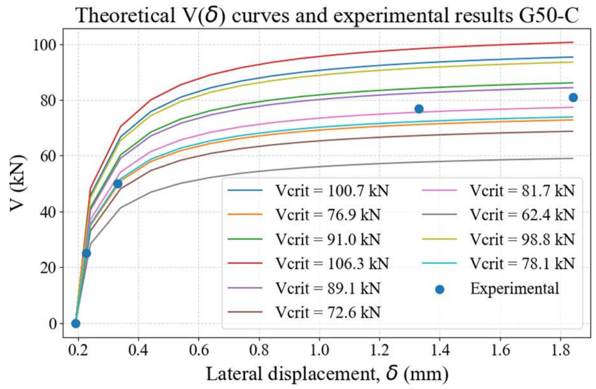

b) Southwell curves for beam G50-NC.

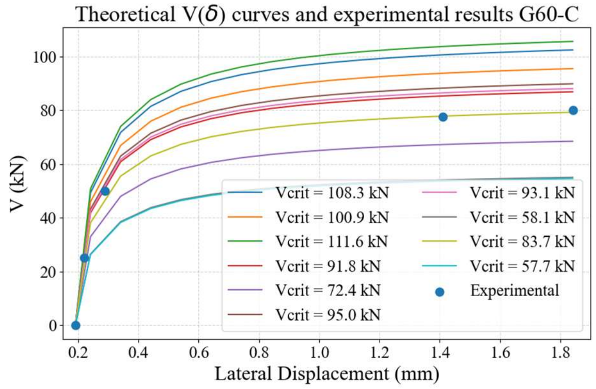

c) Southwell curves for beam G60-NC.

Source: The author (2026)

Figure 43 illustrates the influence of the variables on the prediction of corroded beams. From the simulations, pit depth has a strong negative correlation (-0.7 to -0.5) with the maximum shear load, meaning that an increase in c results in higher slenderness, making the beam increasingly susceptible to buckling, which is consistent with the experimental observations presented in this study. In both Figure 43a and 43b, it is evident that the pit has a significant impact on the WPB, of the same order of magnitude as t_w, as both establish the compressive strut section height with opposite correlation signs with the shear load.

Figure 43 - Pearson correlation of variables for corroded beams.

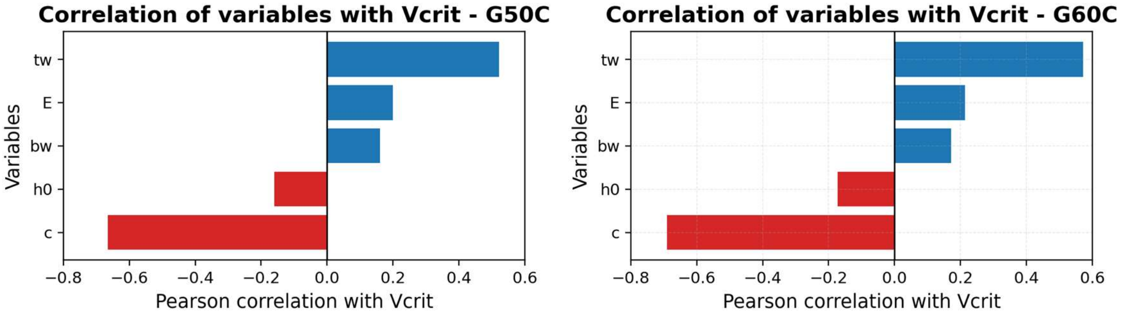

a) G50-C.

b) G60-C.

Source: The author (2026)

CHAPTER 05 – NUMERICAL MODEL

This chapter presents the numerical framework developed to simulate the structural response of the steel beams investigated in this study, with emphasis on the influence of pitting corrosion on strength, stiffness, strain evolution, and failure mode. The finite element model was implemented in ABAQUS and includes the definition of mesh discretization, boundary conditions, initial geometric imperfections, constitutive modelling of steel, and residual stress patterns. In addition, a stochastic procedure based on a correlated Gaussian random field was adopted to reproduce the spatial variability of thickness loss caused by corrosion. The chapter also addresses the calibration of mesh size and spatial correlation parameters, the comparison between numerical and experimental results for both non-corroded and corroded beams, and the validation of the modelling strategy against independent experimental results available in the literature.

5.1 MODELLING STRATEGY AND NUMERICAL ASSUMPTIONS

The numerical analyses illustrated in Figure 44 were performed using the finite element software ABAQUS. Figure 44a presents the adopted discretization, in which the beam components were meshed with a 15 mm element size using three-node reduced-integration shell elements (S3R). Figure 44b shows the preliminary eigenvalue buckling analysis used to obtain the imperfection shape; the first mode was then imposed as an initial geometric imperfection with an amplitude of $L/1000$ (Benedito *et al.*, 2023; Xiao *et al.*, 2023), and the subsequent nonlinear response was traced using the Riks method. Figure 44c summarizes the boundary conditions: fork supports were simulated by restraining the lateral displacement (U1) and the longitudinal rotation (UR3) over the stiffeners; the vertical displacement (U2) was restrained at both roller regions; and the out-of-plane displacement (U3) was additionally restrained at one support to suppress rigid-body motion. Figure 44d depicts the steel constitutive model proposed by Earls (Earls, 1999a, 1999b) with experimental strengths (Benedito *et al.*, 2026) $f_y = 365\text{MPa}$

and $f_u = 465$MPa for Grade 50 and $f_y = 425$ MPa and $f_u = 545$MPa for Grade 60 . Finally, Figure 44e illustrates the ECCS residual stress model adopted to represent residual stresses in hot-rolled profiles (ECCS European Convention for Constructional Steelwork., 1984).

Figure 44 - Finite element modelling assumptions and setup.

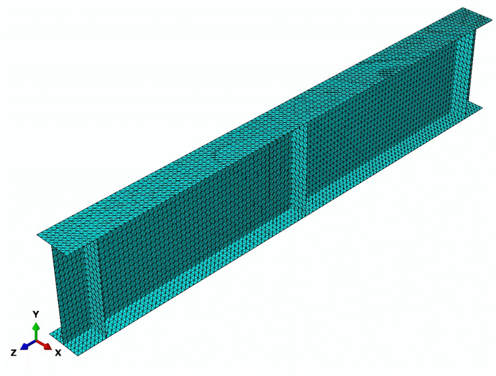

a) Finite element mesh of the steel beam.

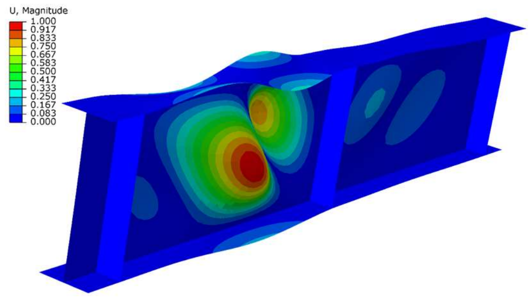

b) eigenvalue buckling analysis.

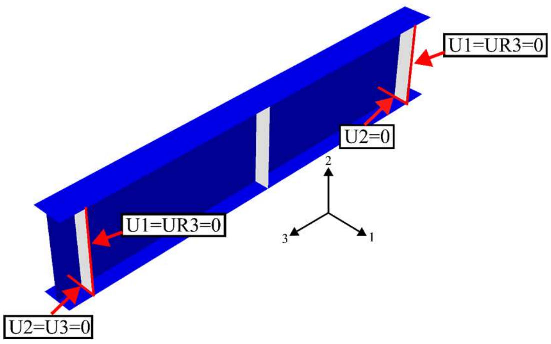

c) Boundary conditions.

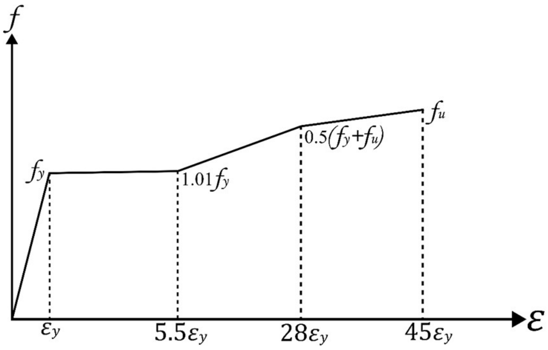

d) Stress–strain relationship proposed by Earls.

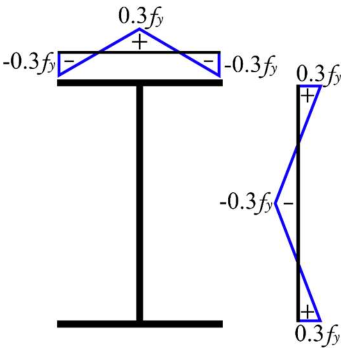

e) ECCS residual stress model (ECCS European Convention for Constructional Steelwork., 1984).

Source: The author (2026)

5.2 CORRELATED GAUSSIAN FIELD

Stochastic thickness fields were generated using a one–dimensional stationary Gaussian random field, following standard formulations for random fields in engineering mechanics as presented by (Vanmarcke *et al.*, 1986). The nodal thickness field is modeled as a correlated Gaussian random field. The nodal coordinates are arranged in the vector $\mathrm{x} = (\mathrm{x}_1, \ldots, \mathrm{x}_\mathrm{n})^\mathrm{T}$, and the distance matrix is defined in Equation 21.

$$D_{ij} = \left|x_i - x_j\right| \tag{21}$$

The spatial dependence is introduced through the exponential covariance kernel in Equation 22.

$$R_{ij} = e^{\left(-\frac{D_{ij}}{Lc}\right)} \tag{22}$$

Where L_c is the correlation length, set as 300 mm following the stochastic corrosion model calibrated by (Teixeira; Soares, 2008), who identified this value from measured thickness-loss maps of diverses corroded steel plates. Exponential kernels and their associated covariance structures are widely used in the construction of Gaussian random fields and are consistent with the classical stochastic field theory presented by (Vanmarcke *et al.*, 1986). To interpolate between uncorrelated and fully correlated behavior, the covariance matrix is blended via the convex combination in Equation 23.

$$R_f = \left(1 - \rho_f\right)I + \rho_f R \tag{23}$$

$\rho_f \in [0,1]$ denote the correlation-strength parameter, I is the identity matrix, , R the correlation matrix defined by the kernel in Equation (22), and $\mathrm{R}_f = (1 - \rho_f)\mathrm{I} + \rho_f \mathrm{R}$ the blended covariance structure used for field generation. Figure 45 schematically illustrates the effect of ρ_f on the pit-depth field, where lower ρ_f produces more irregular, node-to-node fluctuations and higher ρ_f yields smoother spatial variations with stronger continuity along the member. Setting $\rho_f = 0$ gives a fully uncorrelated field $\left(\mathrm{R}_f = \mathrm{I}\right)$, whereas $\rho_f = 1$ recovers the fully correlated structure defined by Eq. (22) $\left(\mathrm{R}_f = \mathrm{R}\right)$, and intermediate values provide a gradual transition between these extremes, consistent with stochastic field modelling practice (Vanmarcke *et al.*, 1986) and with experimental evidence of spatial dependence in pitting corrosion (Melchers, 2005). The matrix R_f is factorised by Cholesky decomposition, and correlated Gaussian realisations are generated using the tensor–vector mapping in Equation (24).

Figure 45 - Schematic illustration of spatially correlated and uncorrelated pit depth fields.

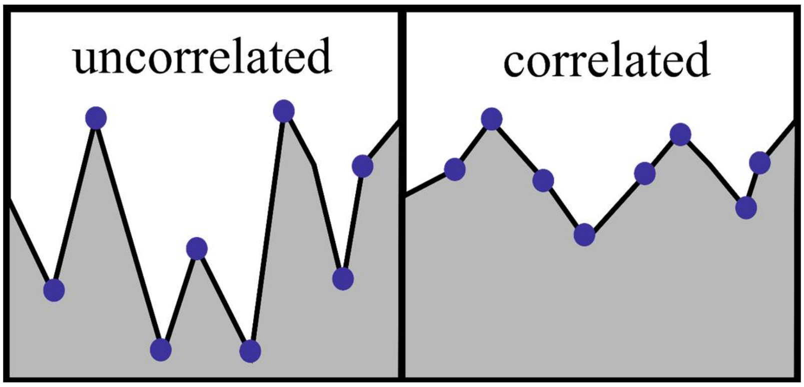

Source: The author (2026)

$$X^{(k)} = L \cdot Z^{(k)} \tag{24}$$

where $Z^{(k)}$ is an independent standard normal vector, that is, a vector of uncorrelated random variables with zero mean and unit variance. It provides the initial uncorrelated Gaussian samples that are transformed by L in Equation 24 to introduce the desired spatial dependence in the generated field. Each correlated Gaussian realization is subsequently mapped to a lognormal field using the moment-matching relations in Equations 25 and 26.

$$s^2 = ln\left(1 + \frac{\sigma^2}{\mu^2}\right) \tag{25}$$

$$m = \ln(u) - \frac{s^2}{2} \tag{26}$$

μ and σ represent the experimental mean and standard deviation of pit depths (Benedito *et al.*, 2026), respectively, and they define the statistical properties of the target lognormal field through moment matching. The corresponding pit-depth values are then obtained from Equation 27:

$$D_i^{(k)} = e^{(m+sX_i^{(k)})} \tag{27}$$

Because corrosion acts independently on each exposed surface, two lognormal fields were generated and summed to obtain the total depth, for example the thickness of the beam web, as shown in Equation 28.

$$D_i = D_i^{(1)} + D_i^{(2)} \tag{28}$$

Finally, the remaining thickness at each node is computed using Equation 29.

$$t_i = t_{nom} - D_i \tag{29}$$

where t_{nom} is the nominal (uncorroded) plate thickness and $t_i$is the local residual thickness after subtracting the total pit depth D_i. This definition provides the spatially variable thickness field used in the numerical model.

Figure 46 summarizes the correlated Gaussian random-field workflow adopted to generate spatially varying thickness loss and perform the finite element analyses. After meshing the beam with $n$nodes, nodal coordinates are used to compute the distance matrix and assemble an exponential correlation matrix defined by the prescribed correlation length (Vanmarcke *et al.*, 1986). while the parameter ρ_f blends correlated and uncorrelated components to control the intensity of spatial dependence. A standard normal vector $\mathrm{Z} \sim \mathcal{N}(0, \mathrm{I})$ is sampled and mapped to a correlated Gaussian field through $\mathrm{X} = \mathrm{LZ}$, where L follows from the Cholesky factorization of the blended covariance matrix. The Gaussian field is then transformed into a lognormal pit-depth field by moment matching using the experimental mean and standard deviation reported in (Benedito *et al.*, 2026), and two statistically independent fields are superposed to represent two-sided corrosion on the plate faces. The resulting pit-depth field is converted to a residual-thickness distribution and implemented in Abaqus via a nodal discrete field to assign spatially varying shell thickness, after which the nonlinear structural analysis is executed for N samples and response statistics are compiled.

Figure 46 - Workflow for modeling of pitting corrosion.

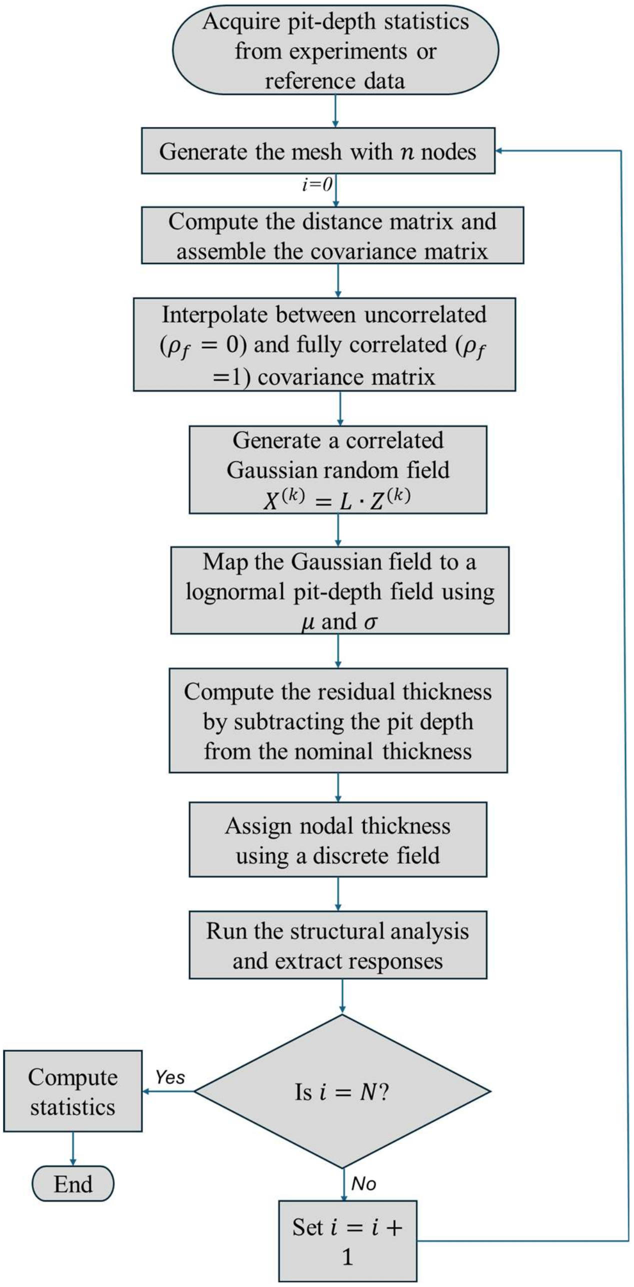

Source: The author (2026)

Figure 47 illustrates the resulting beam thickness distributions for selected correlation levels (ρ_f= 0, 0.5, and 1.0). Lower correlation levels lead to more abrupt and irregular thickness fluctuations along the beam, whereas higher correlation levels result in smoother and more gradual variations, indicating a more homogeneous thickness field

Figure 47 - Effect of spatial correlation on beam thickness distribution.

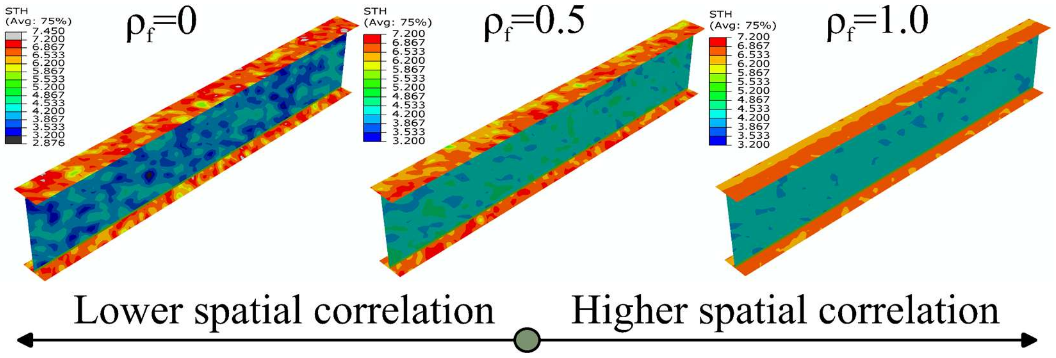

Source: The author (2026)

5.3 SPATIAL CORRELATION AND MESH

Three mesh sizes (10mm, 15mm, and 20mm) and five values of ρ_f(0, 0.25, 0.50, 0.75, and 1.0) were investigated. For each value of ρ_f, ten numerical load–displacement curves were obtained, from which the mean response and the corresponding standard deviation were calculated. The shaded band around each mean curve represents the $\mu \pm 1\sigma$ interval. Figure 48 presents the load–displacement curves for the different mesh refinements and $\rho_f$values. Figure 48a and 48b present the load–displacement curves for the 10 mm mesh in the G50 and G60 series, respectively, in which the finer discretization resulted in lower load-carrying capacity compared with the less refined meshes. This behavior is attributed to the larger number of nodes and the more detailed representation of corrosion pits, leading to greater effective cross-sectional loss and, consequently, reduced beam strength and stiffness. In contrast, as shown in Figure 48e and 48f, the 20 mm mesh consistently exhibited the highest load-carrying capacity, indicating that coarser representations tend to capture less pronounced sectional degradation and, therefore, predict higher structural resistance. In addition, all simulations considering $\rho_f = 0$ exhibited the lowest stiffness, since the assumption of fully random and independent pit formation leads to significantly higher probabilities of extreme pit depths, resulting in less resistant structural responses (Melchers, 2005). All individual numerical simulations used to construct these curves are presented in Appendix B.

Figure 48 - Load–displacement curves for the different mesh refinements and ρ_f values.

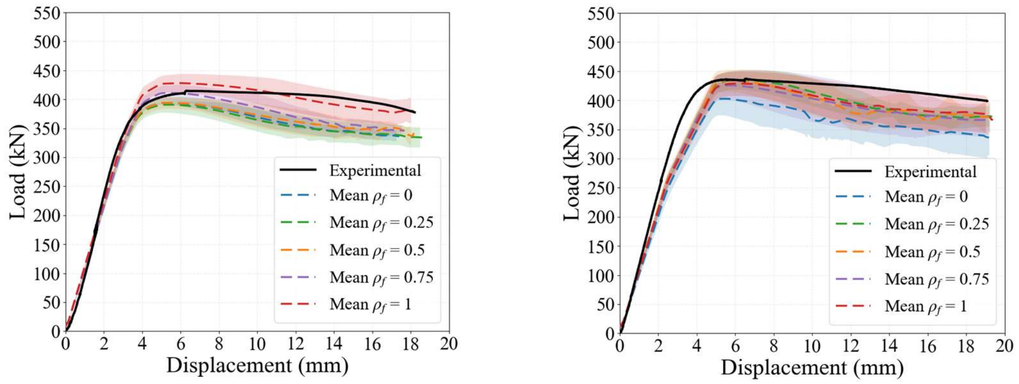

a) G50-C mesh=10mm. b) G60-C mesh=10mm.

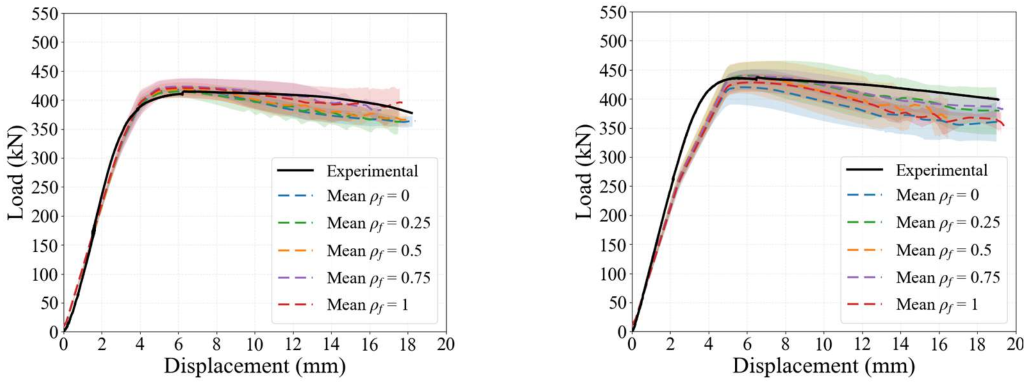

c) G50-C mesh=15mm. d) G60-C mesh=15mm.

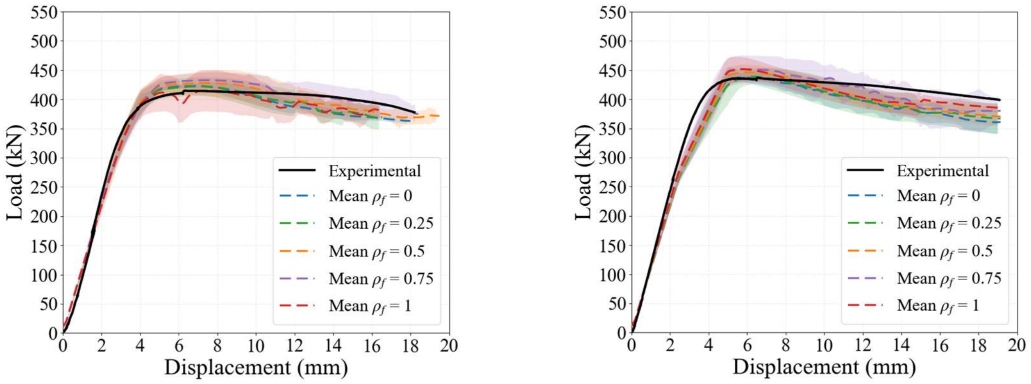

e) G50-C mesh=20mm. f) G60-C mesh=20mm.

Source: The author (2026)

To quantitatively evaluate the agreement between the experimental and numerical responses, the mean absolute error (MAE) was adopted as a performance indicator, as defined by Equation (30)

$$MAE = \frac{100}{n}\sum_{i=1}^{n}\left|\frac{F_i^{exp} - F_i^{num}}{F_i^{exp}}\right| \tag{30}$$

where F_i^{exp} is the experimental load, F_i^{num} is the numerical load at the same displacement level, and $n$is the total number of points considered in the comparison. The MAE was calculated by comparing the load values of the corresponding curves at displacement intervals of 0.5 mm for all simulated responses, enabling a systematic point-by-point assessment of the prediction accuracy along the loading path (Costa; Krahl; De Santana Gomes, 2025). Table 5 shows that a correlation factor of $\rho_f = 0.75$ provides the best agreement with the experimental results, indicating that highly correlated corrosion patterns lead to more accurate predictions of the structural response. This trend is consistent with the findings of (Woloszyk; Garbatov, 2020) and (Melchers, 2005).

Table 5 - MAE results for different mesh sizes and correlation factors.

	MAE G50-C (%)	MAE G50-C (%)
Mesh 10 - $\rho_f = 0$	7.28	7.10
Mesh 10 - $\rho_f = 0.25$	8.19	5.42
Mesh 10 - $\rho_f = 0.50$	7.16	8.59
Mesh 10 - $\rho_f = 0.75$	5.75	9.65
Mesh 10 - $\rho_f = 1.0$	4.64	6.35
Mesh 15 - $\rho_f = 0$	3.99	7.45
Mesh 15 - $\rho_f = 0.25$	4.07	6.18
Mesh 15 - $\rho_f = 0.50$	3.84	6.65
Mesh 15 - $\rho_f = 0.75$	3.70	3.92
Mesh 15 - $\rho_f = 1.0$	4.74	5.41
Mesh 20 - $\rho_f = 0$	3.85	8.63
Mesh 20 - $\rho_f = 0.25$	4.03	6.12
Mesh 20 - $\rho_f = 0.50$	4.12	5.91
Mesh 20 - $\rho_f = 0.75$	4.26	6.74
Mesh 20 - $\rho_f = 1.0$	5.05	6.12

Source: The author (2026)

Figure 49 shows the comparison between ST01 and ST05 for the experimental results and a numerical simulation with Mesh 15 and $\rho_f = 0.75$. Based on the strain responses, the numerical model reproduces this corrosion-driven shift by showing that reduced flange thickness promotes earlier out-of-plane instability and strain reversal before the tensile flange reaches the yield strain, leading to a buckling-governed response rather than full section yielding.

Figure 49 - Experimental and numerical comparison for ST01 and ST05.

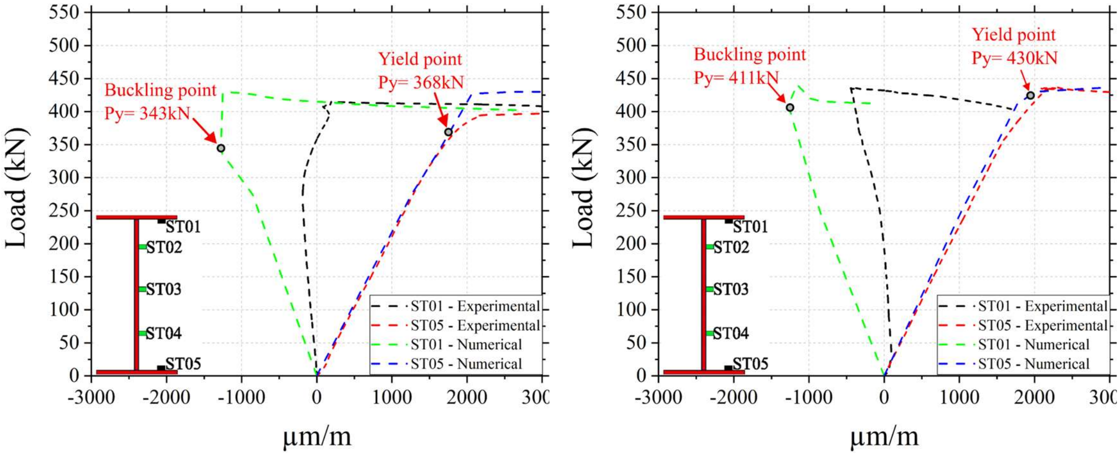

a) Strain G50-C numerical and experimental.

b) Strain G60-C numerical and experimental.

Source: The author (2026)

Figure 50 demonstrates that the numerical model captures the same failure mechanism reported experimentally in Figure 29 for the corroded beams G50-C and G60-C, local buckling of the upper flange. In agreement with Figure 29c and 29d corrosion modifies the buckling morphology, resulting in a distinct half-wavelength and a diminished post-buckling deformation capacity, consequently, upper-flange buckling initiates prior to full cross-sectional yielding, indicating a shift toward a buckling-governed response.

Figure 50 – Numerical failure for G50-C and G60-C.

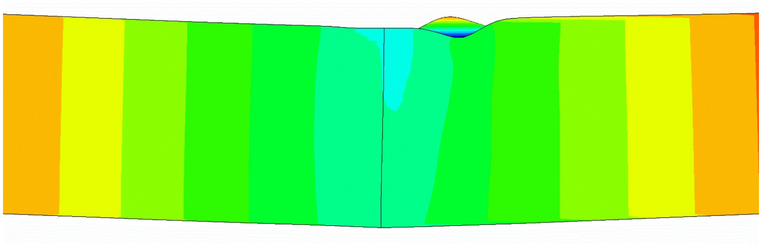

a) Numerical failure G50-C

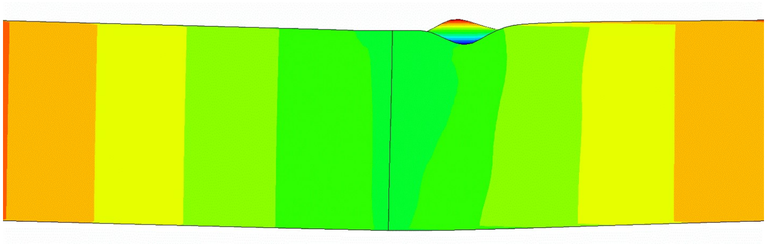

b) Numerical failure G60-C

Source: The author (2026)

Figure 51 illustrates the load–displacement curves for non-corroded beams of the two steel grades, with a 15 mm mesh used in the simulations. Figure 51a and 51b show a similar match between the numerical and experimental results for both grades. Figure 51c and 51d present the corresponding load–strain curves from the numerical model and the experiments, indicating that in the simulations section yielding developed prior to the onset of instability, consistent with the experimental observations.

Figure 51 - Load–displacement curves for non-corroded beams.

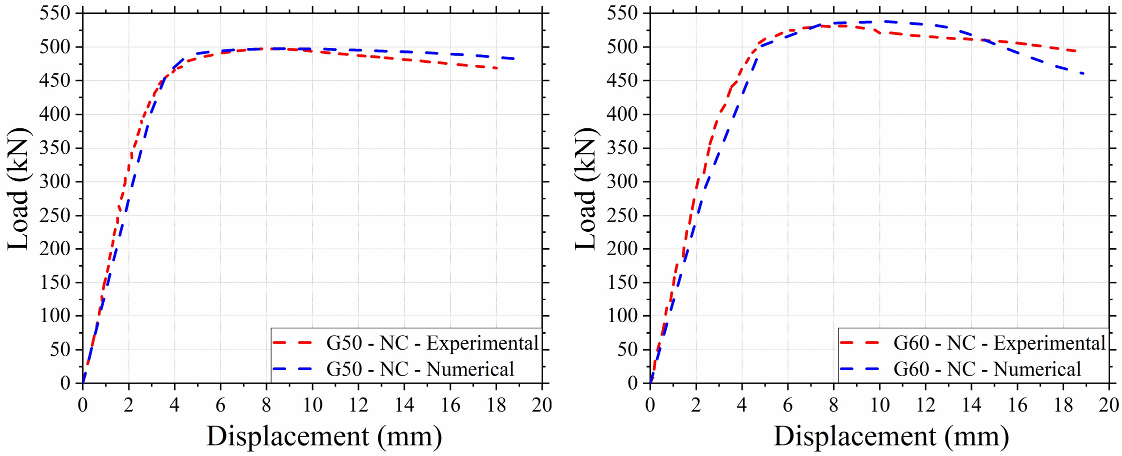

a) Numerical and experimental Curves load–displacement of G50-NC.

b) Numerical and experimental Curves load–displacement of G50-NC.

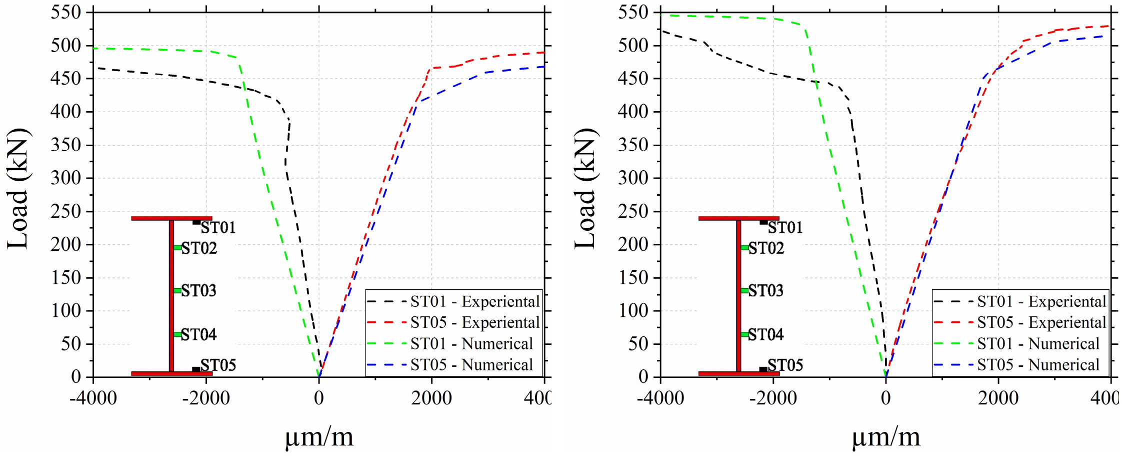

c) Strain G50-NC numerical and experimental.

d) Strain G60-NC numerical and experimental.

Source: The author (2026)

5.4 MODEL VALIDATION

The accuracy of the finite element model was validated, with the experimental study from the literature that reports the mean and standard deviation of pit depths (Xiao *et al.*, 2023). First, the non-corroded model was simulated. Figure 52a presents the load–

displacement curve, showing good agreement between the experimental and numerical responses. In addition, the flange buckling pattern observed experimentally was well reproduced by the numerical model, as illustrated in Figure 52b and 52c.

Figure 52- Load–displacement curve and numerical and experimental failure.

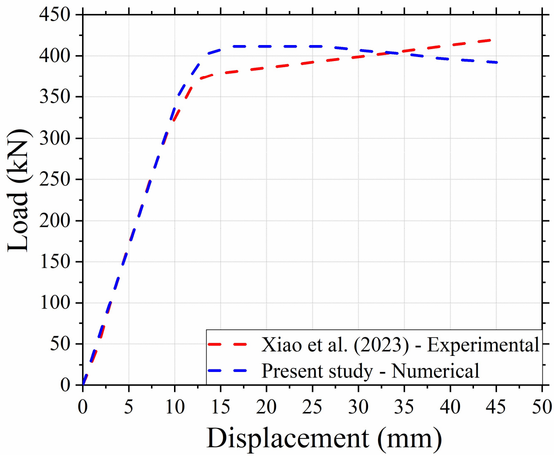

a) Numerical and experimental curve load x displacement.

b) Experimental result Xiao et al.

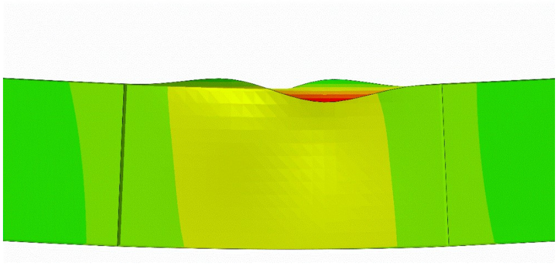

c) Numerical result.

Source: The author (2026) and (Xiao *et al.*, 2023)

Figure 53 compares the experimental and numerical load–longitudinal strain responses for the non-corroded beam reported by Xiao et al. (Xiao *et al.*, 2023) at locations P3, P6, and P9 on the upper flange and T3, T6, and T9 on the lower flange. Overall, the numerical model reproduces the measured stiffness and strain evolution with increasing load, capturing the expected bending-induced compression in the upper flange and tension in the lower flange, as well as the redistribution of strains as the response becomes nonlinear. Minor discrepancies close to the peak load are attributed to strain localization associated with the onset of instability and to the sensitivity of the post-peak response to initial imperfections and modelling idealizations.

Figure 53 - Non-corroded beam Xiao et al (Xiao *et al.*, 2023) experimental vs numerical load–strain.

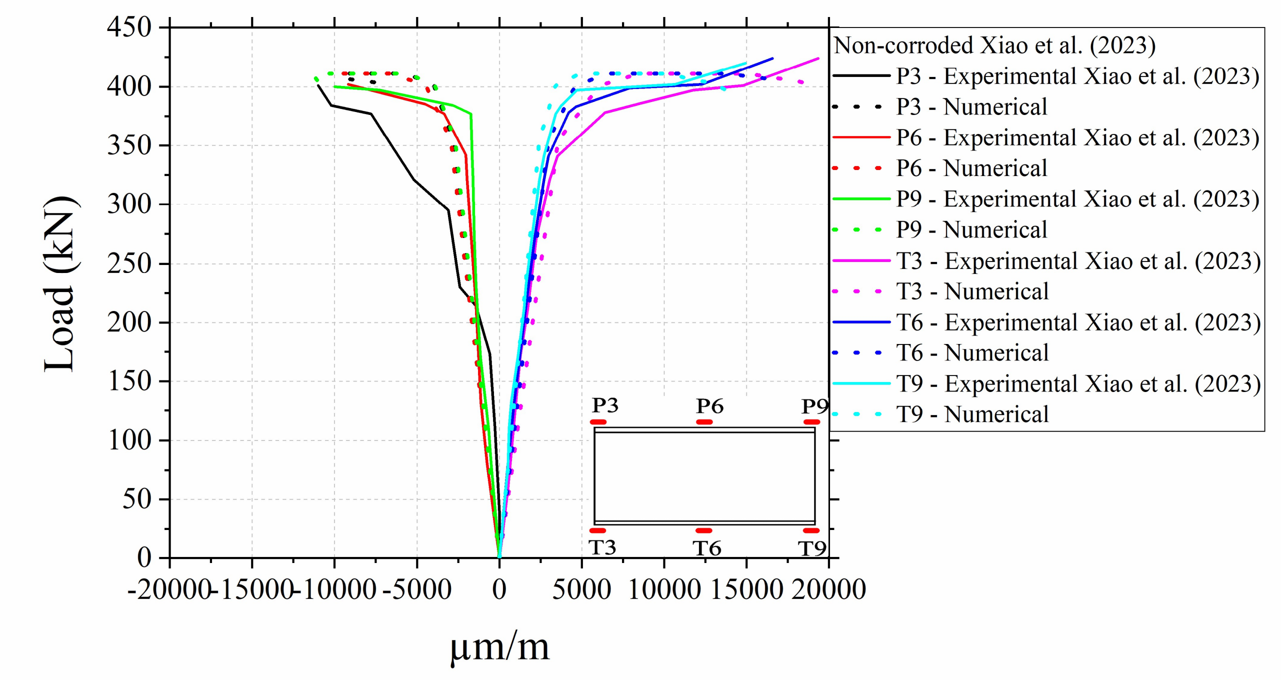

Source: The author (2026) and (Xiao *et al.*, 2023)

For the corroded simulations, the same parameters calibrated for the beams in the present study were adopted, namely a 15 mm mesh and ρf=0.75. Based on the experimental results of Xiao et al. (Xiao *et al.*, 2023) for beams with 10% and 12% mass loss due to corrosion, a comparative analysis was performed using the numerical model developed herein, considering the mean and standard deviation of pit depths reported in their study. Figure 54a and 54b presents the comparison between the experimental and numerical load–displacement curves, based on ten numerical simulations for each case.

Figure 54 - Load–displacement curves of numerical and experimental (Xiao *et al.*, 2023).

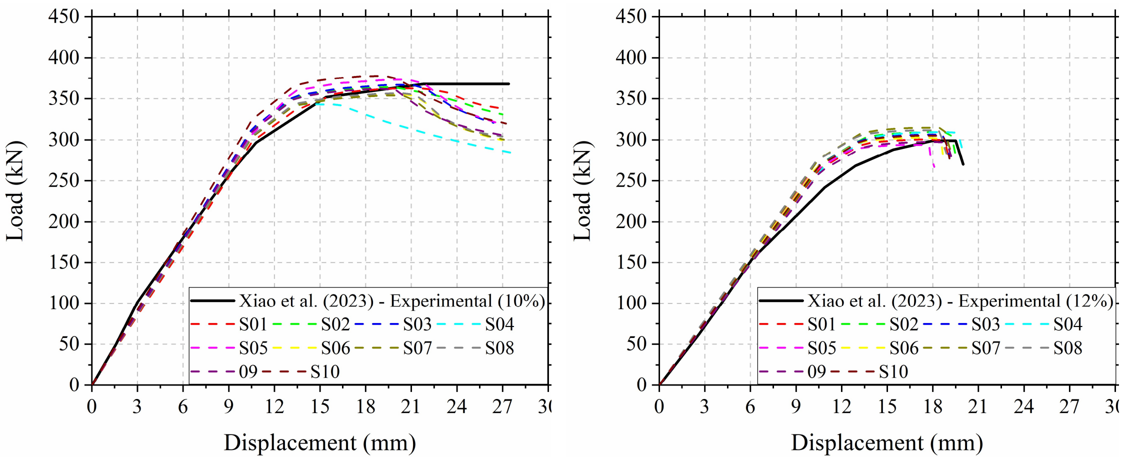

a) Curve load – displacement numerial and experimental 10% corroded.

b) Curve load – displacement numerial and experimental 10% corroded.

Source: The author (2026) and (Xiao *et al.*, 2023)

Figure 55 shows that the failure modes of the numerical model and the experimental beam with 10% and 12% corrosion level are in good agreement. The load–displacement curves and the observed failure patterns indicate that the numerical model developed under the above conditions can accurately reproduce the mechanical behavior of the test beam.

Figure 55 –Failure behavior of the numerical and experimental of the corroded.

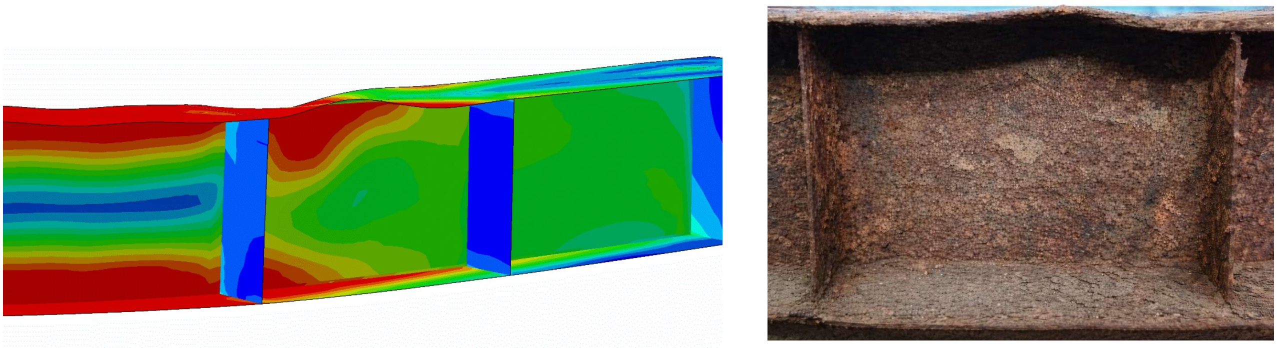

a) Failure mode of the numerical model with 10% corrosion.

b) Failure mode of the beam with 10% corrosion (adapted from (Xiao *et al.*, 2023)).

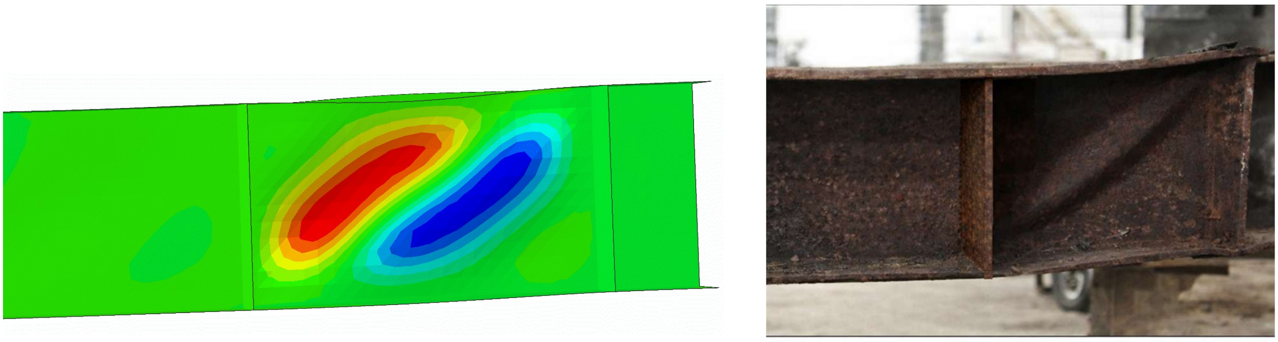

c) Failure mode of the numerical model with 12% corrosion.

d) Failure mode of the beam with 12% corrosion (adapted from (Xiao *et al.*, 2023)).

Source: The author (2026) and (Xiao *et al.*, 2023)

Figure 56a and 56b compare the experimental and numerical load–longitudinal strain responses for beams with 10% and 12% mass loss due to corrosion, respectively. For the 10% corroded beam (Figure 56a), significant disparities are observed between the experimental and numerical strains, which may be partly attributed to experimental uncertainties, particularly possible issues in the installation or bonding quality of the strain gauges, leading to local measurement scatter.

In contrast, the 12% corroded beam (Figure 56b) shows a much closer agreement between experimental and numerical results, indicating that the numerical model captures the dominant strain distribution and corrosion-induced effects more consistently.

Figure 56 - Comparison of experimental (Xiao *et al.*, 2023) and numerical load–strain.

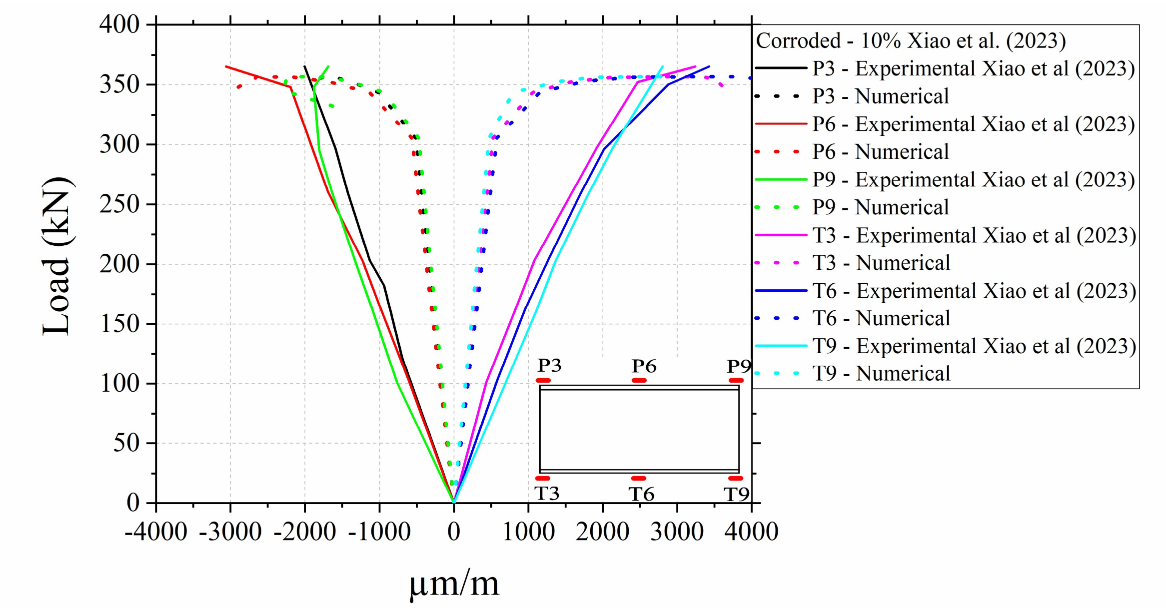

a) 10% corroded experimental and numerical load–strain.

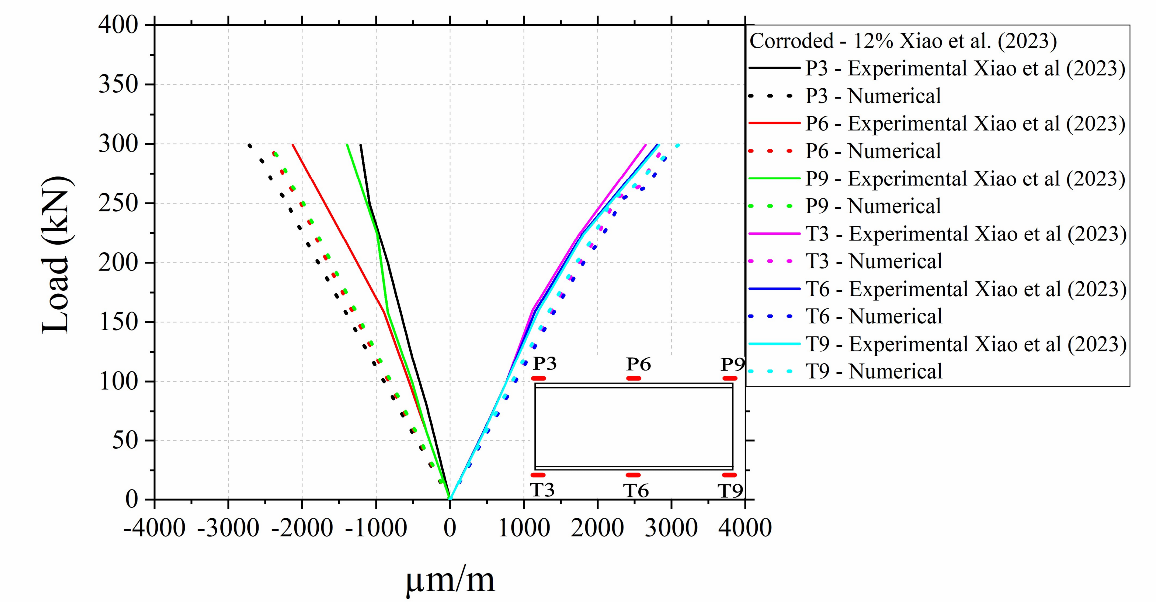

b) 12% corroded experimental and numerical load–strain.

Source: The author (2026) and (Xiao *et al.*, 2023)

CHAPTER 06 - CONCLUSION

This study investigated the flexural behavior of corroded steel beams with and without web openings through an integrated experimental, analytical, and numerical approach, with emphasis on the effects of corrosion on stiffness, load-carrying capacity, strain development, and failure modes. In particular, the research addressed an important gap in the literature by examining not only solid-web beams, but also castellated beams, for which the influence of corrosion on instability-sensitive mechanisms, especially web-post buckling, remains insufficiently understood. By combining experimental observations, analytical formulations, and finite element simulations, the study provided a comprehensive assessment of the structural response of corroded members and advanced the understanding of how localized thickness loss and material degradation modify the flexural and stability performance of steel beams. The main conclusions drawn from this investigation are summarized in the following topics.

- Corrosion significantly reduced the ultimate load and deformation capacity of the beams, leading to peak loads at smaller displacements and promoting a clear shift in failure behavior from yielding-dominated response to instability failure, governed by premature local buckling of the compressed flange

- The correlation length and spatial correlation level strongly influenced the structural response, with higher spatial correlation providing more realistic predictions of strength and stiffness; in particular, a correlation level of $\rho_f = 0.75$ provided the best agreement with experimental results, with MAE values of about 3.7% for Grade 50 and 3.9% for Grade 60 beams.

- The numerical results were sensitive to mesh refinement, as finer meshes captured corrosion-induced sectional losses more accurately and led to lower predicted capacities, a mesh size of 15 mm combined with $\rho_f = 0.75$ was found to provide an optimal balance between numerical stability and fidelity in representing localized corrosion effects.

- The numerical model successfully reproduced the experimentally observed transition from section yielding to local buckling in corroded beams.

- This study advances the assessment of corrosion effects on thin-walled steel beams by reproducing independent experimental results with a calibrated stochastic framework, helping address the scarcity of instability-focused tests and supporting future assessment methods in the absence of explicit design code provisions.

- Pit corrosion reduced the web thickness, which highly favored WPB, resulting in reductions of 39.47% in beam capacity for Grade 50 steel and 35.85% for Grade 60 steel in the investigated beams. The decrease in load capacity is attributed to geometrical changes resulting from corrosion and is not related to steel strength.

- The post-buckling behavior evidenced that the tie formed at the web reached the steel yield stress. The pits promote stress concentration and early failure, substantially reducing the ductility of the beam.

- The proposed non-empirical model demonstrated an average deviation of approximately 10% compared to the non-corroded experimental results and around 7% for corroded beams, indicating robust predictive accuracy and good representativeness for both scenarios.

- From Pearson correlation analysis, it was evident that the shear load resulting from the proposed equation is mainly correlated with pit depth, web thickness, and steel elastic modulus. Eurocode presents a positive correlation with web thickness and a negative correlation with the web opening height. The Steel Design Guide presented a positive correlation with yield strength and opening height. The experiments showed that web thickness governed the WPB.

- The interaction between corrosion and geometric discontinuities, such as web openings, amplified the structural vulnerability, demonstrating that regions already prone to stress concentration become critical points for failure when affected by pitting corrosion.

- Corrosion significantly altered the strain distribution along the beam, with earlier strain reversals observed in the compressed flange, indicating that localized section degradation modifies the classical flexural response and anticipates instability phenomena.

REFERENCES

ABNT (Brazilian Association of Technical Norms). ABNT NBR 8800:2024 - Design of steel and composite steel and concrete building structures. Rio de Janeiro, 2024.

AGLAN, A.; REDWOOD, R. Web Buckling in Castellated Beams. *In*: PROCEEDINGS OF THE DEPARTMENT OF CIVIL ENGINEERING AND APPLIED MECHANICS 1974, McGill University, Montreal, Canada.

APOSTOLOPOULOS, C. A.; MICHALOPOULOS, D. Effect of Corrosion on Mass Loss, and High and Low Cycle Fatigue of Reinforcing Steel. **Journal of Materials Engineering and Performance**. vol. 15, 6, p. 742–749. 2006

AYODEJI, A. I.; FAYOMI, O. S. I.; DANIYAN, A. A.; BABAREMU, K. O.; ABIOYE, P. O.; AGBOOLA, O. Corrosion Phenomena and the Occurrences; A comment. **IOP Conference Series: Materials Science and Engineering**. vol. 1107, 1, p. 012101. 2021

BAO, A.; GUILLAUME, C.; SATTER, C.; MORAES, A.; WILLIAMS, P.; KELLY, T.; GUO, Y. Testing and evaluation of web bearing capacity of corroded steel bridge girders. **Engineering Structures**. vol. 238, p. 112276. 2021

BENEDITO, A. V.; BENEDETTY TORRES, C. A.; SILVA, R. M. de C.; KRAHL, P. A.; CARDOSO, D. C. T.; SILVA, F. de A.; MARTINS, C. H. Effects of Niobium Addition on the Mechanical Properties and Corrosion Resistance of Microalloyed Steels: A Review. **Buildings**. vol. 14, 5, p. 1462. 2024

BENEDITO, A. V.; KRAHL, P. A.; DOS SANTOS, V. B.; DE OLIVEIRA, V. M.; ROSSI, A.; SILVA, F. de A.; CARDOSO, D. C. T.; MARTINS, C. H. Experimental analysis and a new model to predict web-post buckling of corroded Anglo-Saxon castellated beams. **Thin-Walled Structures**. vol. 221, p. 114417. 2026

BENEDITO, A. V.; MILANI, M. F. P.; KRAHL, P. A.; MARQUES, B. B.; DE NARDIN, S.; MARTINS, C. H. Nonlinear finite element analysis of partially encased composite columns under non-uniform moments. **Structures**. vol. 58, p. 105519. 2023

BHANDARI, J.; KHAN, F.; ABBASSI, R.; GARANIYA, V.; OJEDA, R. Modelling of pitting corrosion in marine and offshore steel structures – A technical review. **Journal of Loss Prevention in the Process Industries**. vol. 37, p. 39–62. 2015

BOYER, J. P. Castellated Beams - New Developments. **Engineering Journal**. vol. 1, 3, p. 104–108. 1964

BS5950. **Structural use of steel work in building Part 1:code of practice for design—rolled and welded sections.** 2000

CHEN, J.; JIANG, A.; JIN, W. Behavior of Steel–Concrete Composite Beams with Corroded Shear Studs Under Negative Bending Moment. *In*: PROCEEDINGS OF THE 4TH INTERNATIONAL CONFERENCE ON THE DURABILITY OF CONCRETE STRUCTURES 2014, . ISBN: 9781626710184. DOI: 10.5703/1288284315393. Available at: http://docs.lib.purdue.edu/icdcs/2014/corrosion/8/

CHEN, J.; ZHANG, H.; YU, Q.-Q. Monotonic and fatigue behavior of steel-concrete composite beams subjected to corrosion. **Structures**. vol. 34, p. 1973–1984. 2021

CIMADEVILA, FRANCISCO JAVIER ESTÉVEZ; GUTIÉRREZ, EMILIO MARTÍN; RODRÍGUEZ, J.; VÁZQUEZ., A. **Vigas alveoladas**. 2000

COELHO, L. B.; TORRES, D.; BERNAL, M.; PALDINO, G. M.; BONTEMPI, G.; USTARROZ, J. Probing the randomness of the local current distributions of 316 L stainless steel corrosion in NaCl solution. **Corrosion Science**. vol. 217, p. 111104. 2023

COSTA, L. O.; KRAHL, P. A.; DE SANTANA GOMES, W. J. Numerical investigation of heterogeneous behavior in prestressed and reinforced UHPC beams via Gaussian random fields. **Structures**. vol. 80, p. 110145. 2025

DE OLIVEIRA, J. P.; CARDOSO, D. C. T.; SOTELINO, E. D. Elastic flexural local buckling of Litzka castellated beams: Explicit equations and FE parametric study. **Engineering Structures**. vol. 186, p. 436–445. 2019

DE OLIVEIRA, V. M.; DOS SANTOS, V. B.; ROSSI, A.; BENEDITO, A. V.; KRAHL, P. A.; MARTINS, C. H.; DE ANDRADE SILVA, F.; CARDOSO, D. C. T. Steel-UHPC composite castellated beams under hogging bending: Experimental and numerical investigation. **Engineering Structures**. vol. 331, p. 120012. 2025

DRAẐIĆ, D. M.; VAŜĈIẐ, V. The correlation between accelerated laboratory corrosion tests and atmospheric corrosion station tests on steels. **Corrosion Science**. vol. 29, 10, p. 1197–1204. 1989

DU, Y. G.; CLARK, L. A.; CHAN, A. H. C. Effect of corrosion on ductility of reinforcing bars. **Magazine of Concrete Research**. vol. 57, 7, p. 407–419. 2005

DU, Y. G.; CLARK, L. A.; CHAN, A. H. C. Residual capacity of corroded reinforcing bars. **Magazine of Concrete Research**. vol. 57, 3, p. 135–147. 2005

DWIVEDI, D.; LEPKOVÁ, K.; BECKER, T. Carbon steel corrosion: a review of key surface properties and characterization methods. **RSC Advances**. vol. 7, 8, p. 4580–4610. 2017

EARLS, C. . On the inelastic failure of high strength steel I-shaped beams. **Journal of Constructional Steel Research**. vol. 49, 1, p. 1–24. 1999

EARLS, C. J. Effects of material property stratification and residual stresses on single angle flexural ductility. **Journal of Constructional Steel Research**. vol. 51, 2, p. 147–175. 1999

ECCS EUROPEAN CONVENTION FOR CONSTRUCTIONAL STEELWORK. **Ultimate Limit State Calculations of Sway Frames with Rigid Joints.** 1984

EUROCODE 3. **Design of steel structures — Part 1-13: Beams with large web openings**. 2024

EUROCODE 3. **Design of steel structures Part 1-1, General rules and rules for buildings.** 2005

GALAMBOS, A. R.; HOSAIN, M. U.; SPEIRS, W. G. OPTIMUM EXPANSION RATIO OF CASTELLATED STEEL BEAMS. **Engineering Optimization**. vol. 1, 4, p. 213–225. 1975

GALLEGUILLOS MADRID, F. M.; SOLIZ, A.; CÁCERES, L.; BERGENDAHL, M.; LEIVA-GUAJARDO, S.; PORTILLO, C.; OLIVARES, D.; TORO, N.; JIMENEZ-AREVALO, V.; PÁEZ, M. Green Corrosion Inhibitors for Metal and Alloys Protection in Contact with Aqueous Saline. **Materials**. vol. 17, 16, p. 3996. 2024

GARBATOV, Y.; TEKGOZ, M.; SOARES, C. G. Experimental and numerical strength assessment of stiffened plates subjected to severe non-uniform corrosion degradation and compressive load. **Ships and Offshore Structures**. vol. 12, 4, p. 461–473. 2017

GIBSON, J. E.; JENKINS, W. M. **An investigation of the stress and deflections in castellated beams**. 1957

GRILO, L. F.; FAKURY, R. H.; CASTRO E SILVA, A. L. R. De; VERÍSSIMO, G. de S. Design procedure for the web-post buckling of steel cellular beams. **Journal of Constructional Steel Research**. vol. 148, p. 525–541. 2018

GRILO, L. F.; FAKURY, R. H.; CASTRO E SILVA, A. L. R. De; VERÍSSIMO, G. de S. Design procedure for the web-post buckling of steel cellular beams. **Journal of Constructional Steel Research**. vol. 148, p. 525–541. 2018

GRÜNBAUER BV. Accessed on 02/30/2026. Web page https://www.grunbauer.nl/. 2026

GUO, Z.; MA, Y.; WANG, L.; ZHANG, J.; HARIK, I. E. Corrosion Fatigue Crack Propagation Mechanism of High-Strength Steel Bar in Various Environments. **Journal of Materials in Civil Engineering**. vol. 32, 6. 2020

HOSSEINZADEH, L.; KONTONI, D.-P. N.; BABAEI, B. Investigation of the Behavior of Steel Plate Shear Walls Considering Double Corrugated Low-Yield-Point Steel Infill Plate. **International Journal of Civil Engineering**. vol. 21, 10, p. 1631–1642. 2023

IMPERATORE, S.; RINALDI, Z.; DRAGO, C. Degradation relationships for the mechanical properties of corroded steel rebars. **Construction and Building Materials**. vol. 148, p. 219–230. 2017

ISO 9223. Corrosion of Metals and Alloys, Corrosivity of Atmospheres, Classification, Determination and Estimation. 2012

JAFAR MAZUMDER, M. A. Global Impact of Corrosion: Occurrence, Cost and Mitigation. **Global Journal of Engineering Sciences**, v. 5, n. 4, jun. 2020.

JIA, Z. J.; LI, X. G.; DONG, C. F.; CHENG, Y. F. Analysis of corrosion of hot-rolled X70 steel plate during storage. **Engineering Failure Analysis**. vol. 16, 7, p. 2342–2347. 2009

JOINT COMMITTEE ON STRUCTURAL SAFETY. **Probabilistic model code - Part 3: Resistance models**. 2001

KATONA, R. M.; KNIGHT, A. W.; SCHINDELHOLZ, E. J.; BRYAN, C. R.; SCHALLER, R. F.; KELLY, R. G. Quantitative assessment of environmental phenomena on maximum pit size predictions in marine environments. **Electrochimica Acta**. vol. 370, p. 137696. 2021

KERDAL, D.; NETHERCOT, D. A. Failure modes for castellated beams. **Journal of Constructional Steel Research**. vol. 4, 4, p. 295–315. 1984

KRAHL, P. A.; CARRAZEDO, R.; EL DEBS, M. K. Analytical solutions for rollover instability of concrete beams on elastomeric bearing pads. **Engineering Structures**. vol. 174, p. 154–164. 2018

KUANG, Y. C.; FENG, J. R.; YU, Z. W.; LIU, X. J. Experimental Study and Analysis of the Structural Behavior of Steel-Concrete Composite Beam after Shear Connector Corrosion. **Applied Mechanics and Materials**. vols. 578–579, p. 1522–1530. 2014

KUHLMANN, U.; SCHMIDT-RASCHE, C.; JÖRG, F.; POUROSTAD, V.; SPIEGLER, J.; EULER, M. Update on the revision of Eurocode 3. **Steel Construction**. vol. 14, 1, p. 2–13. 2021

LAWSON, R. M.; LIM, J.; HICKS, S. J.; SIMMS, W. I. Design of composite asymmetric cellular beams and beams with large web openings. **Journal of Constructional Steel Research**. vol. 62, 6, p. 614–629. 2006

LUNT, T. T.; PRIDE, S. T.; SCULLY, J. R.; HUDSON, J. L.; MIKHAILOV, A. S. Cooperative Stochastic Behavior in Localized Corrosion: II. Experiments. **Journal of The Electrochemical Society**. vol. 144, 5, p. 1620–1629. 1997

LUO, L.; FU, H.; ZHANG, Y.; XIE, X. Experimental Study on the Overall Stability of Corroded H-Shaped Steel Beams. **Buildings**. vol. 12, 11, p. 1923. 2022

LUO, L.; FU, H.; ZHANG, Y.; XIE, X. Experimental Study on the Overall Stability of Corroded H-Shaped Steel Beams. **Buildings**. vol. 12, 11, p. 1923. 2022

LUO, L.; XU, C.; ZHANG, Y.; PAN, C.; CHEN, B. Global buckling bearing capacity of corroded H-section steel beams. **Structures**. vol. 69, p. 107552. 2024

MA, Y.; GUO, Z.; WANG, L.; ZHANG, J. Probabilistic Life Prediction for Reinforced Concrete Structures Subjected to Seasonal Corrosion-Fatigue Damage. **Journal of Structural Engineering**. vol. 146, 7. 2020

MA, Y.; GUO, Z.; WANG, L.; ZHANG, J. Experimental investigation of corrosion effect on bond behavior between reinforcing bar and concrete. **Construction and Building Materials**. vol. 152, p. 240–249. 2017

MA, Y.; PENG, A.; SU, X.; WANG, L.; ZHANG, J. Modeling Constitutive Relationship of Steel Bar Removed from Corroded PC Beams after Fatigue Considering Spatial Location Effect. **Journal of Materials in Civil Engineering**. vol. 33, 4. 2021

MA, Y.; PENG, A.; WANG, L.; ZHANG, C.; LI, J.; ZHANG, J. Fatigue performance of an innovative shallow-buried modular bridge expansion joint. **Engineering Structures**. vol. 221, p. 111107. 2020

MA, Y.; YANG, J.; SU, X.; PENG, A.; WANG, L.; HUANG, K. Crack propagation characterization of concrete under non-uniform corrosion of steel strand using digital image correlation. **Construction and Building Materials**. vol. 455, p. 139166. 2024

MAHDAVIPOUR, M. A.; THEOFANOUS, M.; DIRAR, S.; FARAMARZI, A. Lateral-torsional buckling of high-strength steel beams under stochastic corrosion-induced mass loss. **Mechanics Based Design of Structures and Machines**. p. 1–25. 2026

MELCHERS, R. A Review of Trends for Corrosion Loss and Pit Depth in Longer-Term Exposures. **Corrosion and Materials Degradation**. vol. 1, 1, p. 42–58. 2018

MELCHERS, R. E. Statistical Characterization of Pitting Corrosion—Part 2: Probabilistic Modeling for Maximum Pit Depth. **Corrosion**. vol. 61, 8, p. 766–777. 2005

MORCILLO, M.; CHICO, B.; DÍAZ, I.; CANO, H.; DE LA FUENTE, D. Atmospheric corrosion data of weathering steels. A review. **Corrosion Science**. vol. 77, p. 6–24. 2013

NAKAI, T.; MATSUSHITA, H.; YAMAMOTO, N. Effect of pitting corrosion on strength of web plates subjected to patch loading. **Thin-Walled Structures**. vol. 44, 1, p. 10–19. 2006

NAKAI, T.; MATSUSHITA, H.; YAMAMOTO, N. Effect of pitting corrosion on local strength of hold frames of bulk carriers (2nd Report)—Lateral-distortional buckling and local face buckling. **Marine Structures**. vol. 17, 8, p. 612–641. 2004

NAKAI, T.; MATSUSHITA, H.; YAMAMOTO, N.; ARAI, H. Effect of pitting corrosion on local strength of hold frames of bulk carriers (1st report). **Marine Structures**. vol. 17, 5, p. 403–432. 2004

NAM, N. D.; KIM, J. G. Effect of niobium on the corrosion behaviour of low alloy steel in sulfuric acid solution. **Corrosion Science**. vol. 52, 10, p. 3377–3384. 2010

NIE, B.; XU, S.; ZHANG, Z.; GU, R. Experimental investigation on corroded cold-formed steel beam-columns under compression and major axis bending. **Journal of Constructional Steel Research**. vol. 169, p. 106026. 2020

NYBY, C.; GUO, X.; SAAL, J. E.; CHIEN, S.-C.; GERARD, A. Y.; KE, H.; LI, T.; LU, P.; OBERDORFER, C.; SAHU, S.; LI, S.; TAYLOR, C. D.; WINDL, W.; SCULLY, J. R.; FRANKEL, G. S. Electrochemical metrics for corrosion resistant alloys. **Scientific Data**. vol. 8, 1, p. 58. 2021

OBEYESEKERE, N. U. Pitting corrosion. Elsevier, 2017. p. 215–248

OU, Y.-C.; SUSANTO, Y. T. T.; ROH, H. Tensile behavior of naturally and artificially corroded steel bars. **Construction and Building Materials**. vol. 103, p. 93–104. 2016

PALSSON, R.; MIRZA, M. S. Mechanical Response of Corroded Steel Reinforcement of Abandoned Concrete Bridge. **ACI Structural Journal**. vol. 99, 2. 2002

PEDEFERRI, P. Pitting Corrosion. 2018. p. 207–230

PENG, J.; XIAO, L.; ZHANG, J.; CAI, C. S.; WANG, L. Flexural behavior of corroded HPS beams. **Engineering Structures**. vol. 195, p. 274–287. 2019

RANJI, A. R.; ZAKERI, S. A. H. **Mechanical Properties And Corrosion Resistance of Normal Strength And High Strength Steels In Chloride Solution**. 2011

REDWOOD, R.; DEMIRDJIAN, S. Castellated Beam Web Buckling in Shear. **Journal of Structural Engineering**. vol. 124, 10, p. 1202–1207. 1998

SAMEER S. FARES; COULSON, J.; DAVID W. DINEHART. Castellated and Cellular Beam Design 31. **American Institute of Steel Construction**. p. 1–116. 2016

SHENG, J.; XIA, J.; MA, R. Experimental study on the coupling effect of sulfate corrosion and loading on the mechanical behavior of steel and H-section beam. **Construction and Building Materials**. vol. 189, p. 711–718. 2018

SHENG, J.; XIA, J.; MA, R. Experimental study on the coupling effect of sulfate corrosion and loading on the mechanical behavior of steel and H-section beam. **Construction and Building Materials**. vol. 189, p. 711–718. 2018

SILVA, J.; GARBATOV, Y.; SOARES, C. Ultimate strength assessment of ageing steel plates subjected to random non-uniform corrosion wastage. CRC Press, 2011. p. 213–220

SOUTHWELL, R. V. On the analysis of experimental observations in problems of elastic stability. **Proceedings of the Royal Society of London. Series A, Containing Papers of a Mathematical and Physical Character**. vol. 135, 828, p. 601–616. 1932

TEIXEIRA, Â. P.; SOARES, C. G. Ultimate strength of plates with random fields of corrosion. **Structure and Infrastructure Engineering**. vol. 4, 5, p. 363–370. 2008

TOPRAC, A. A.; COOKE, B. R. **An experimental investigation of open-web beams.** 1959

TZORTZINIS, G.; AI, C.; BREÑA, S. F.; GERASIMIDIS, S. Using 3D laser scanning for estimating the capacity of corroded steel bridge girders: Experiments, computations and analytical solutions. **Engineering Structures**. vol. 265, p. 114407. 2022

TZORTZINIS, G.; KNICKLE, B. T.; BARDOW, A.; BREÑA, S. F.; GERASIMIDIS, S. Strength evaluation of deteriorated girder ends. I: Experimental study on naturally corroded I-beams. **Thin-Walled Structures**. vol. 159, p. 107220. 2021

VAN ORDEN, A. C. Corrosion mechanisms relevant to high-level waste repositories. **Engineering Geology**. vol. 26, 4, p. 331–349. 1989

VANMARCKE, E.; SHINOZUKA, M.; NAKAGIRI, S.; SCHUËLLER, G. I.; GRIGORIU, M. Random fields and stochastic finite elements. **Structural Safety**. vol. 3, 3–4, p. 143–166. 1986

VIEIRA, W. B. **Numerical-experimental study of web buckling in castellated steel beams**. Federal University of Viçosa. 2015

WANG, B.; HUANG, W.; ZHENG, S. Study on Restoring Force Performance of Corrosion Damage Steel Frame Beams under Acid Atmosphere. **Applied Sciences**. vol. 9, 1, p. 103. 2018

WANG, H.; WANG, Y.; ZHANG, Z.; LIU, X.; XU, S. Cyclic behavior and hysteresis model of beam-column joint under salt spray corrosion environment. **Journal of Constructional Steel Research**. vol. 183, p. 106737. 2021

WANG, L.; DAI, L.; BIAN, H.; MA, Y.; ZHANG, J. Concrete cracking prediction under combined prestress and strand corrosion. **Structure and Infrastructure Engineering**. vol. 15, 3, p. 285–295. 2019

WANG, P.; GUO, K.; LIU, M.; ZHANG, L. Shear buckling strengths of web-posts in a castellated steel beam with hexagonal web openings. **Journal of Constructional Steel Research**. vol. 121, p. 173–184. 2016

WANG, Y.; CHANG, C.; XU, S.; GUEDES SOARES, C. Probabilistic constitutive model for corroded structural steel with stochastic pits under monotonic tension. **Engineering Structures**. vol. 304, p. 117599. 2024

WANG, Y.; KONG, Z.; XU, S. Hysteresis performance of steel beam-column welded T-joints corroded in steel industrial atmosphere. **Engineering Failure Analysis**. vol. 159, p. 108118. 2024

WANG, Y.; WHARTON, J. A.; SHENOI, R. A. Ultimate strength analysis of aged steel-plated structures exposed to marine corrosion damage: A review. **Corrosion Science**. vol. 86, p. 42–60. 2014

WANG, Y.; XU, S.; LI, A. Flexural performance evaluation of corroded steel beams based on 3D corrosion morphology. **Structure and Infrastructure Engineering**. vol. 16, 11, p. 1562–1577. 2020

WOLOSZYK, K.; GARBATOV, Y. Random field modelling of mechanical behaviour of corroded thin steel plate specimens. **Engineering Structures**. vol. 212, p. 110544. 2020

WU, B.; SCULLY, J. R.; HUDSON, J. L.; MIKHAILOV, A. S. Cooperative Stochastic Behavior in Localized Corrosion: I. Model. **Journal of The Electrochemical Society**. vol. 144, 5, p. 1614–1620. 1997

XIA, M.; XU, S.; WANG, Y.; LI, H.; ZHAO, B. Experimental study on bearing capacity of corroded Q345 H-shaped steel column under axial compression load. **Journal of Building Engineering**. vol. 52, p. 104354. 2022

XIAO, L.; CHEN, H.; PENG, J. Experimental study on flexural behavior and bending capacity prediction of Q550E steel beams within corroded shear span. **Structures**. vol. 63, p. 106443. 2024

XIAO, L.; CHEN, H.; PENG, J. Experimental study on flexural behavior and bending capacity prediction of Q550E steel beams within corroded shear span. **Structures**. vol. 63, p. 106443. 2024

XIAO, L.; PENG, J.; CAI, C. S.; CHEN, H. Experimental and numerical investigations on the mechanical behavior of coastal high performance steel beams with local corrosion within the shear-span. **Applied Ocean Research**. vol. 136, p. 103581. 2023

XIAO, L.; PENG, J.; ZHANG, J.; CAI, C. S. Experimental Investigation and Numerical Analysis on Stiffness Degradation of High-Performance Steel Beams with Local Shear-Span Corrosion. *In*: EARTH AND SPACE 2021 2021, Reston, VA. . ISBN: 9780784483381. DOI: 10.1061/9780784483381.049. Available at: https://ascelibrary.org/doi/10.1061/9780784483381.049

XIE, X.; GUO, Z.; ZHAO, Z.; LIANG, Z.; WU, J.; LIU, X.; XIAO, J. Salt-Fog Corrosion Behavior of GCr15 Steels Treated by Ultrasonic Strengthening Grinding Process. **Applied Sciences**. vol. 12, 15, p. 7360. 2022

XIN, J.; WANG, J.; LIU, Z.; YOU, X.; ZHOU, J. Experimental Study on Bearing Capacity of Corroded Reinforced Concrete Arch Considering Material Degradation. **Frontiers in Materials**. vol. 9. 2022

YAMAMOTO, N.; IKEGAMI, K. A Study on the Degradation of Coating and Corrosion of Ship's Hull Based on the Probabilistic Approach. **Journal of Offshore Mechanics and Arctic Engineering**. vol. 120, 3, p. 121–128. 1998

ZAAROUR, W.; REDWOOD, R. Web Buckling in Thin Webbed Castellated Beams.

Journal of Structural Engineering. vol. 122, 8, p. 860–866. 1996

ZAKOWSKI, K.; NAROZNY, M.; SZOCINSKI, M.; DAROWICKI, K. Influence of water salinity on corrosion risk—the case of the southern Baltic Sea coast. **Environmental Monitoring and Assessment**. vol. 186, 8, p. 4871–4879. 2014

ZHANG, T.; VACCARO, M.; ZAGHI, A.; BAGTZOGLOU, A. Geometric characterization of locally corroded surfaces in steel bridge girders. **Frontiers in Built Environment**. vol. 11. 2025

ZHANG, X.; ZHENG, S.; ZHAO, X. Experimental and numerical investigations into seismic behavior of corroded steel frame beams and columns in offshore atmospheric environment. **Journal of Constructional Steel Research**. vol. 201, p. 107757. 2023

ZHANG, X.; ZHENG, S.; ZHAO, X. Experimental and numerical study on seismic performance of corroded steel frames in chloride environment. **Journal of Constructional Steel Research**. vol. 171, p. 106164. 2020

ZHANG, Y.; FANG, C.; WANG, W.; WU, L.; CAO, P. Influence of corrosion on seismic performance of steel beam-to-column connections. **Engineering Structures**. vol. 312, p. 118284. 2024

ZHANG, Z.; XU, S.; WANG, H.; NIE, B.; SU, C. Flexural buckling behavior of corroded hot-rolled H-section steel beams. **Engineering Structures**. vol. 229, p. 111614. 2021

ZHANG, Z.; XU, S.; WANG, Y.; NIE, B.; WEI, T. Local and post-buckling behavior of corroded axially-compressed steel columns. **Thin-Walled Structures**. vol. 157, p. 107108. 2020

ZHU, B.; HUANG, Y.; LI, Z.; CHEN, B.; LIAO, H. Experimental study on bearing capacity of corroded angle steel members of in-service transmission towers. **MATEC Web of Conferences**. vol. 382, p. 01031. 2023

ZHU, J.; LI, D.; CHANG, W.; WANG, Z.; HU, L.; ZHANG, Y.; WANG, M.; YANG, Z.; SONG, J.; CHEN, S.; ZHANG, L.; ZHANG, L. In situ marine exposure study on corrosion behaviors of five alloys in coastal waters of western Pacific Ocean. **Journal of Materials Research and Technology**. vol. 9, 4, p. 8104–8116. 2020

APPENDIX A – TENSILE COUPONS

Figure A. 1 - Tensile Stress–Strain Curves G50 Steel after 0 Months of Corrosion

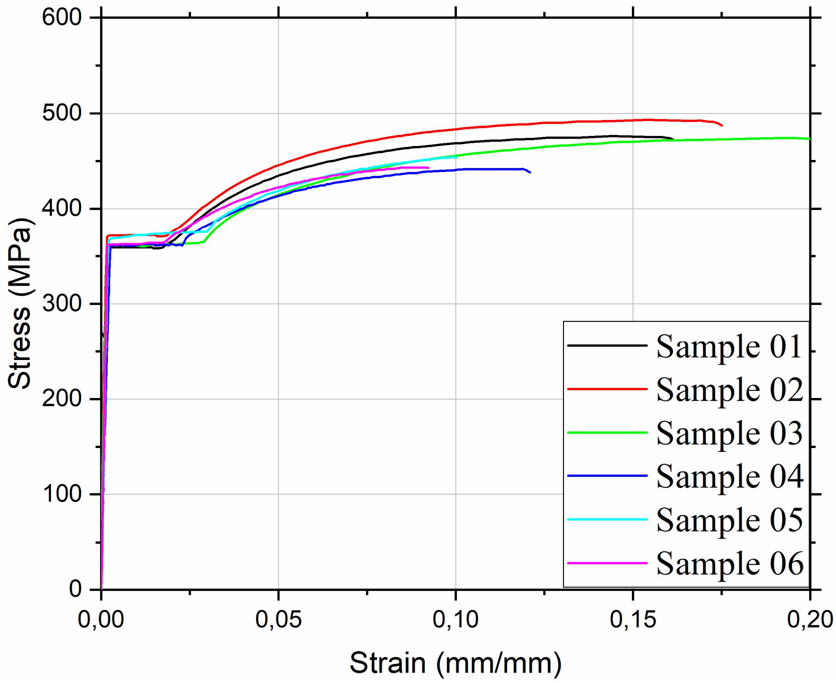

Figure A. 2 - Tensile Stress–Strain Curves G50 Steel after 1 Month of Corrosion

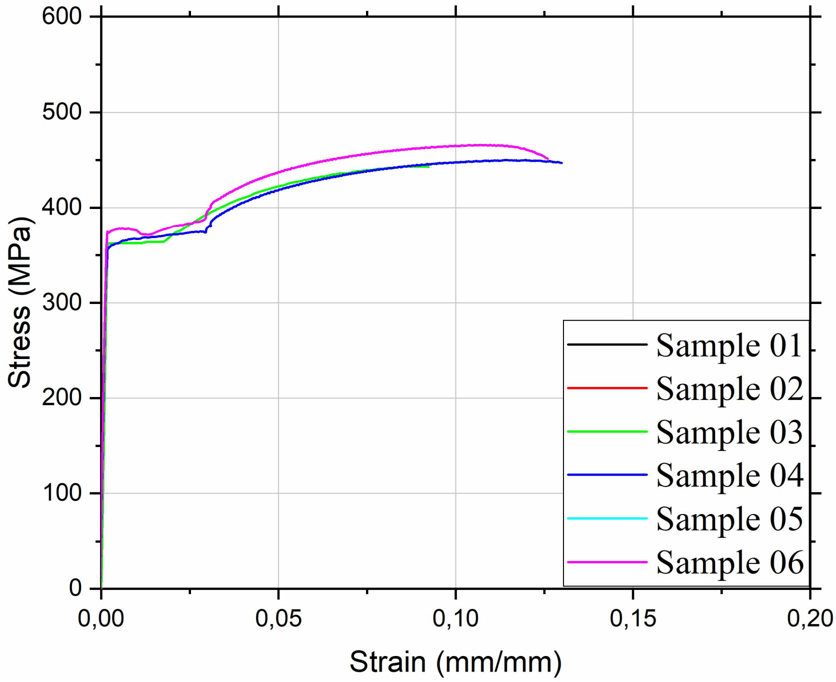

Figure A. 3 - Tensile Stress–Strain Curves G50 Steel after 2 Months of Corrosion

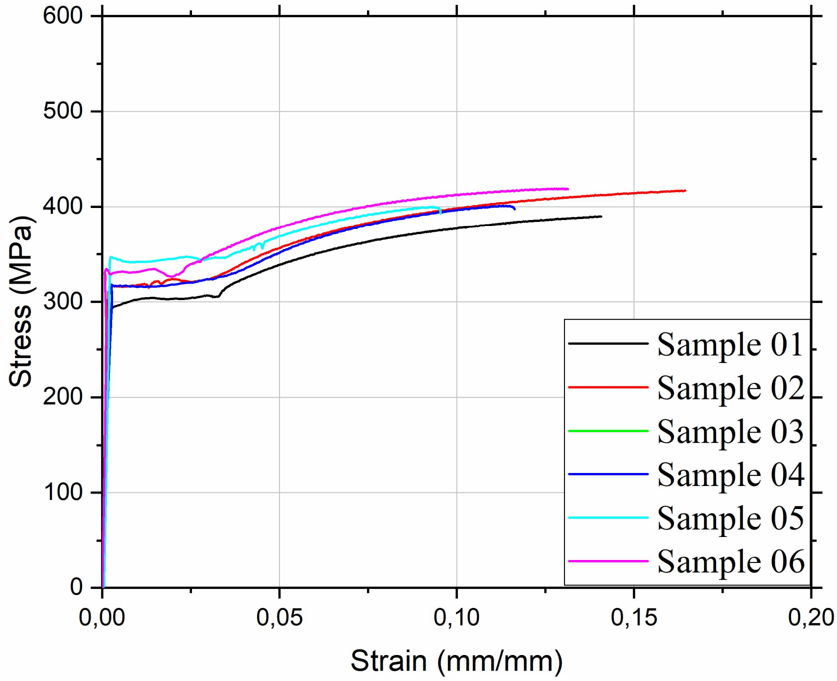

Figure A. 4 - Tensile Stress–Strain Curves G50 Steel after 3 Months of Corrosion

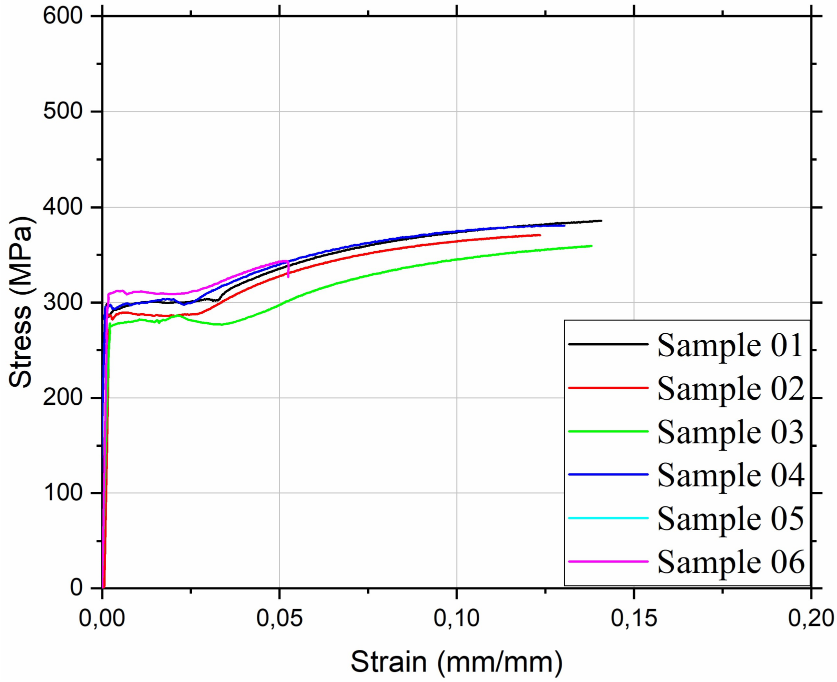

Figure A. 5 - Tensile Stress–Strain Curves G50 Steel after 4 Months of Corrosion

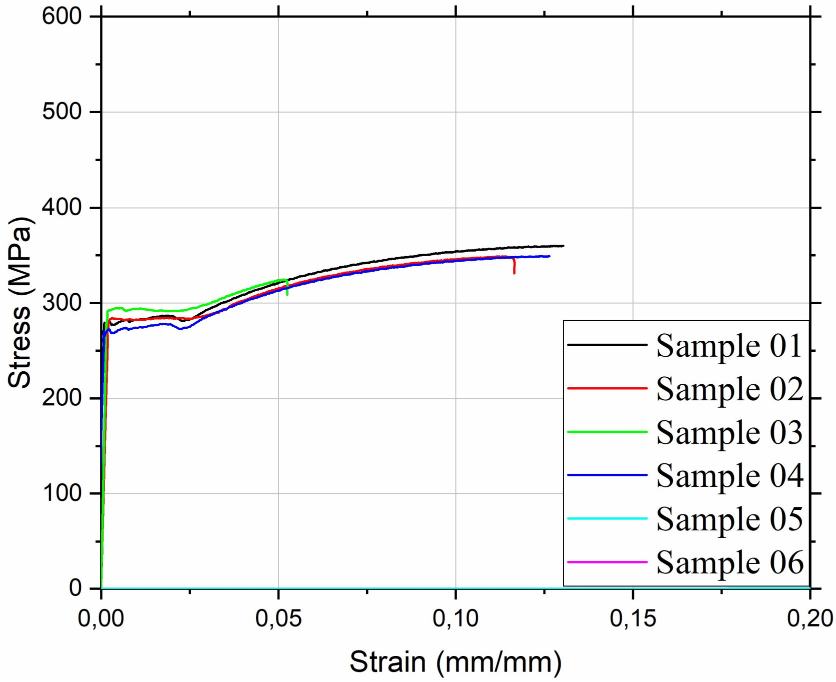

Figure A. 6 - Tensile Stress–Strain Curves G50 Steel after 5 Months of Corrosion

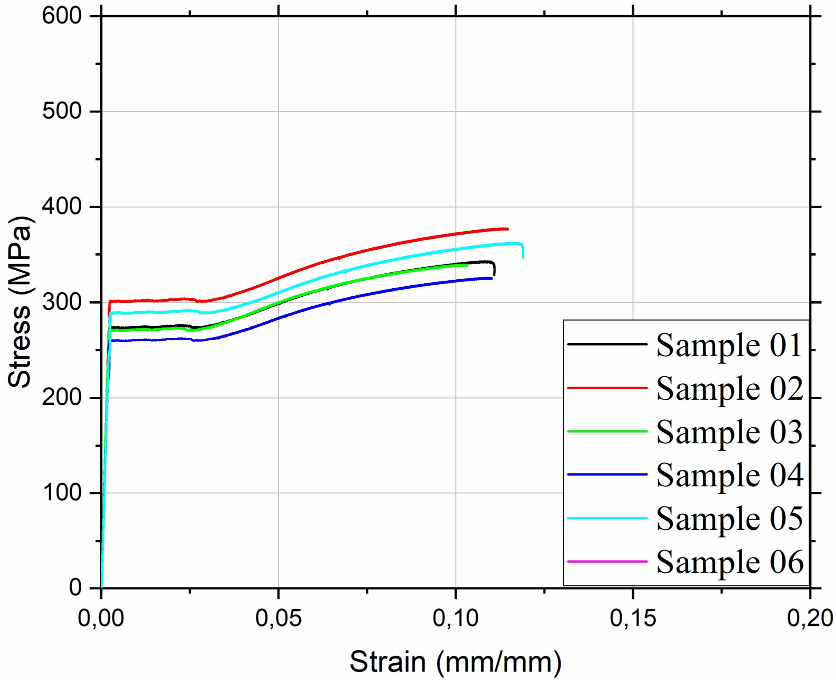

Figure A. 7 - Tensile Stress–Strain Curves G50 Steel after 6 Months of Corrosion

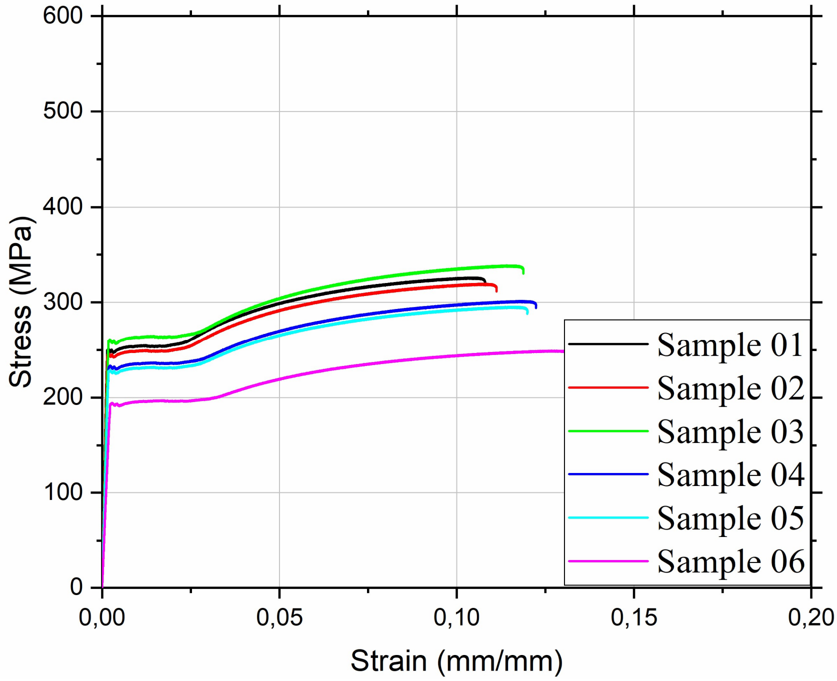

Figure A. 8 - Tensile Stress–Strain Curves G60 Steel after 0 Months of Corrosion

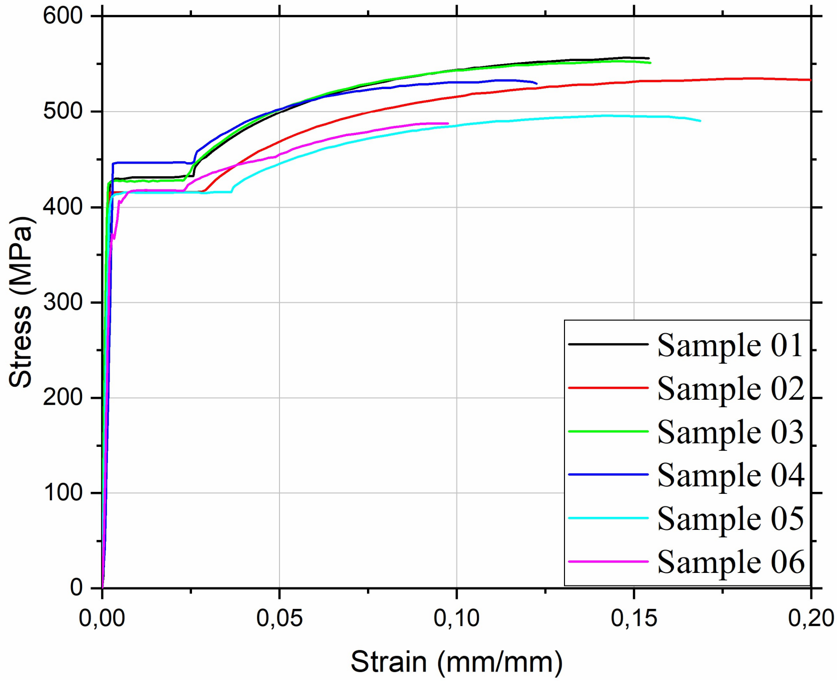

Figure A. 9 - Tensile Stress–Strain Curves G60 Steel after 1 Month of Corrosion

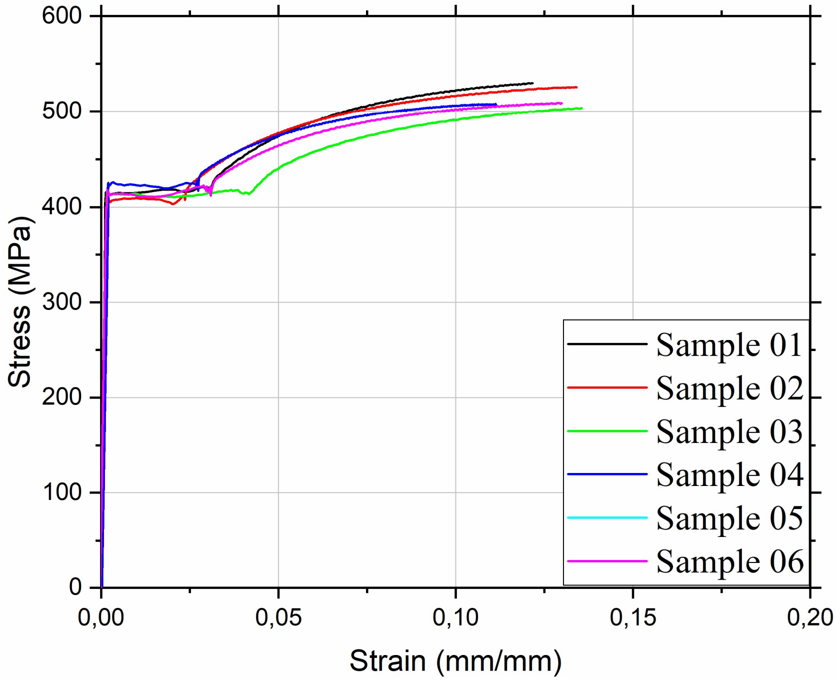

Figure A. 10 - Tensile Stress–Strain Curves G60 Steel after 2 Months of Corrosion

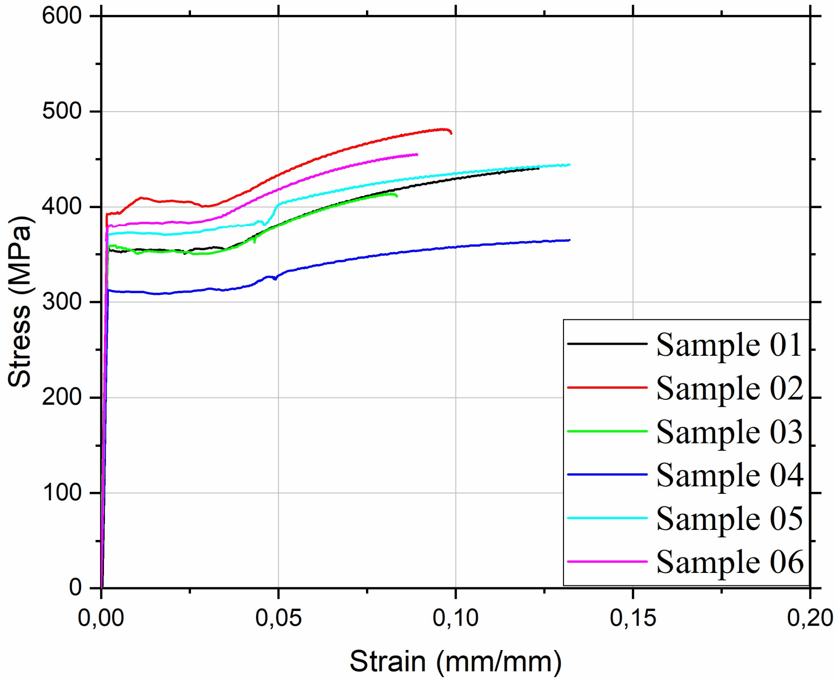

Figure A. 11 - Tensile Stress–Strain Curves G60 Steel after 3 Months of Corrosion

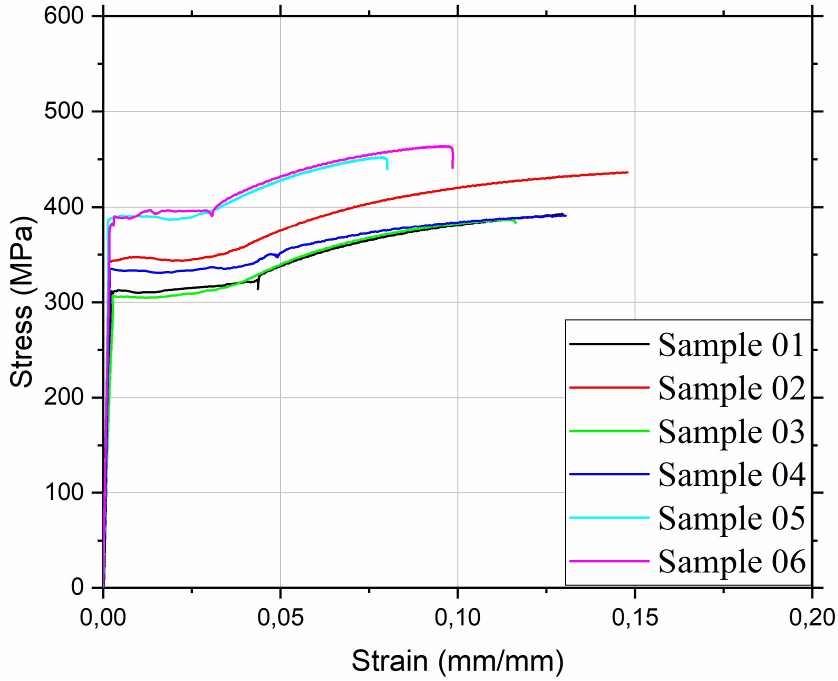

Figure A. 12 - Tensile Stress–Strain Curves G60 Steel after 4 Months of Corrosion

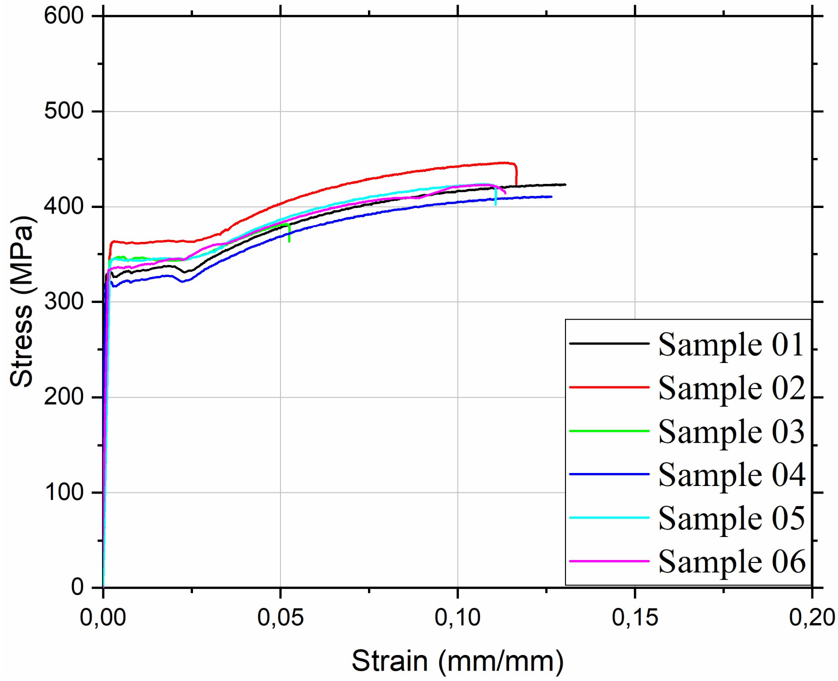

Figure A. 13 - Tensile Stress–Strain Curves G60 Steel after 5 Months of Corrosion

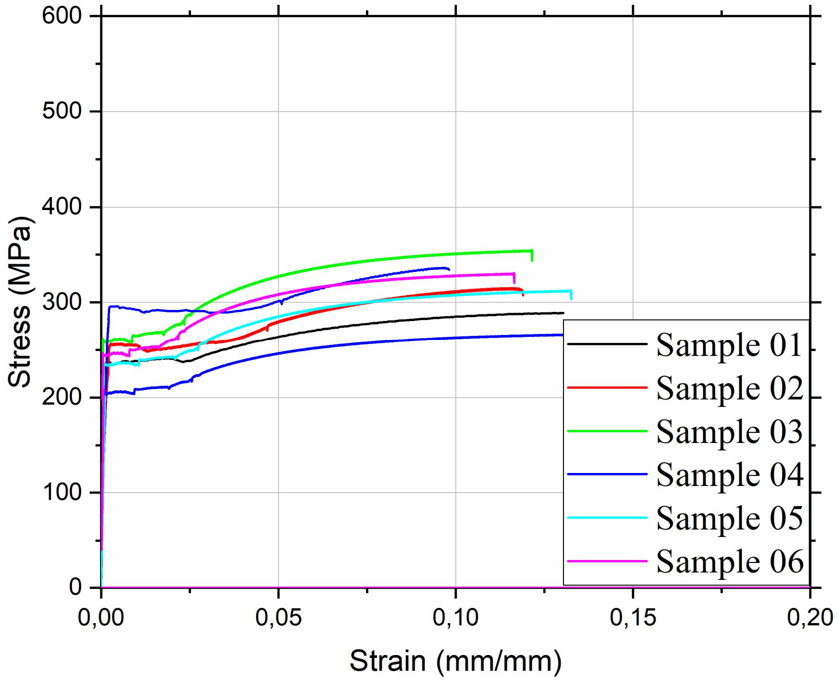

Figure A. 14 - Tensile Stress–Strain Curves G60 Steel after 6 Months of Corrosion

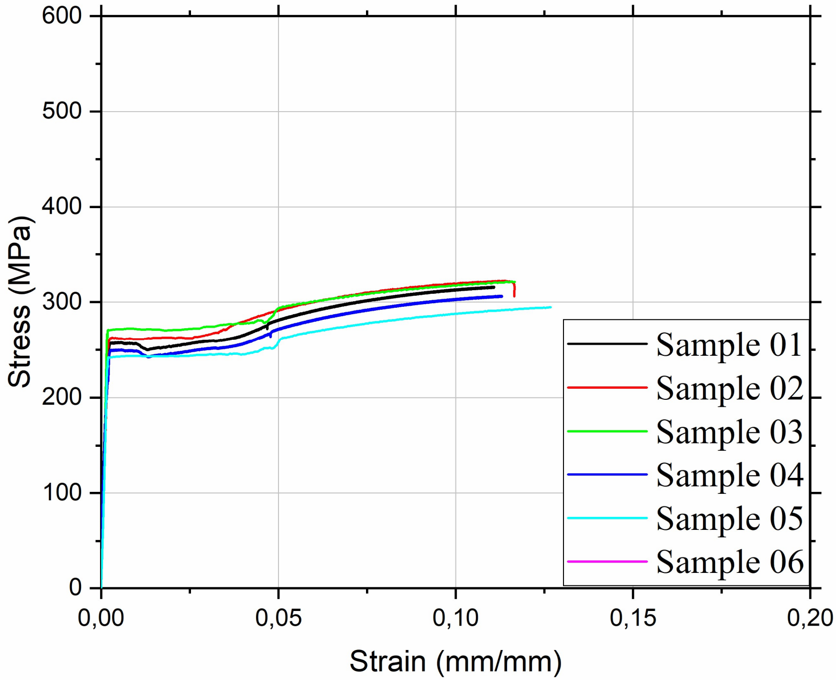

APPENDIX B – NUMERICAL RESULTS

Figure B. 1 – Corroded steel grade 50; mesh =10; $\rho_f = 0$

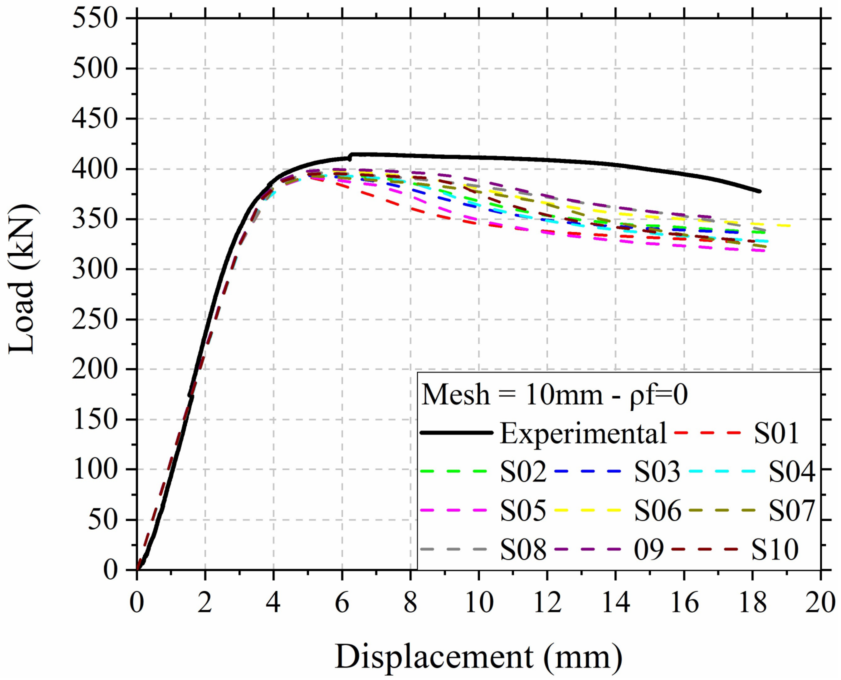

Figure B. 2 – Corroded steel grade 50; mesh =10; $\rho_f = 0.25$

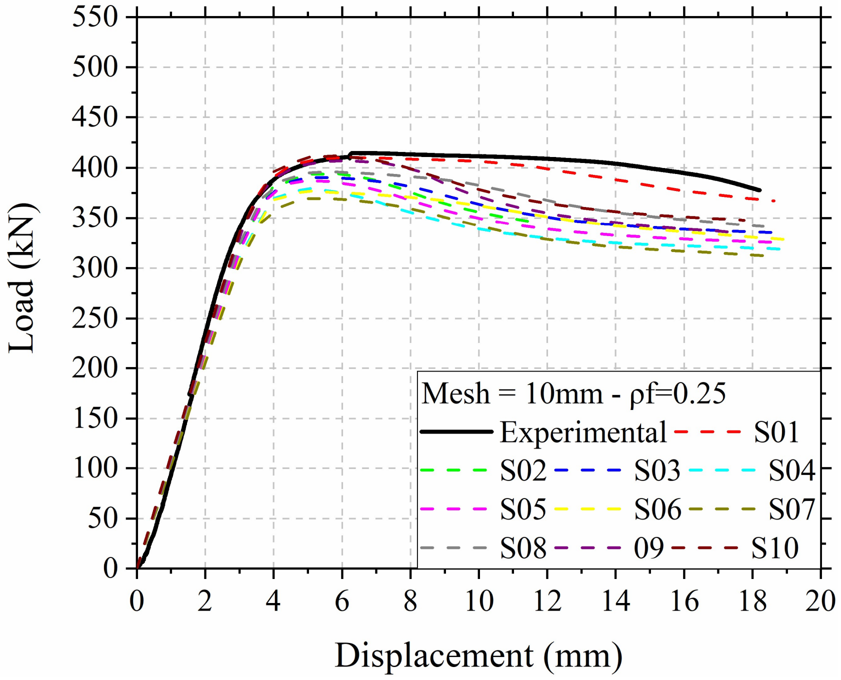

Figure B. 3 – Corroded steel grade 50; mesh =10; $\rho_f = 0.50$

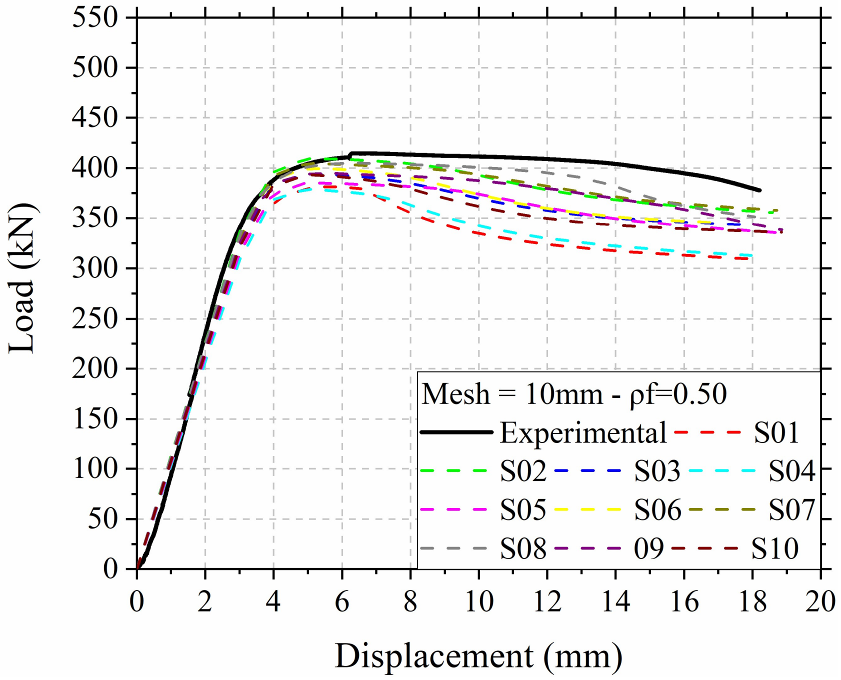

Figure B. 4 – Corroded steel grade 50; mesh =10; $\rho_f = 0.75$

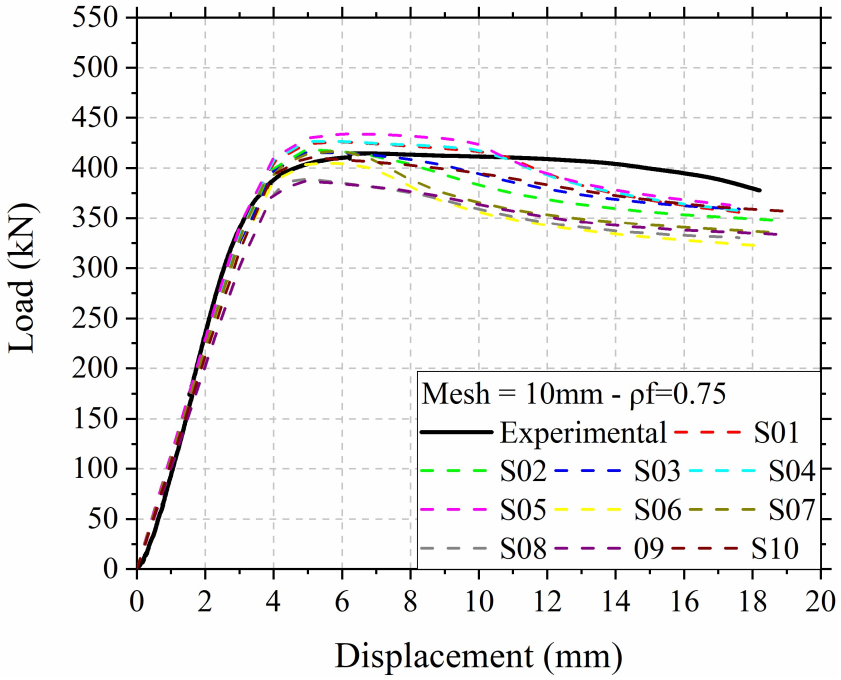

Figure B. 5– Corroded steel grade 50; mesh =10; $\rho_f = 0$

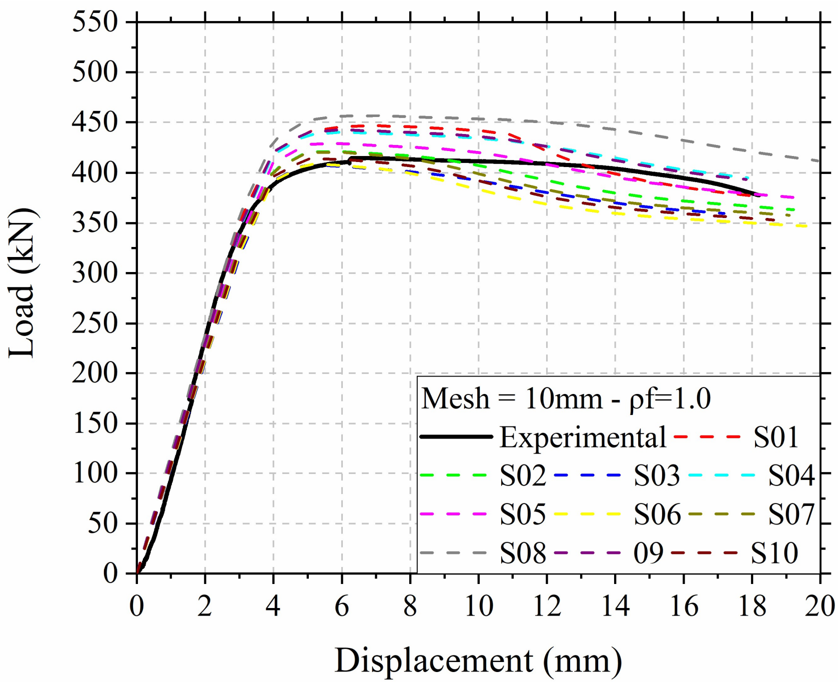

Figure B. 6– Corroded steel grade 50; mesh =10; $\rho_f = 0$

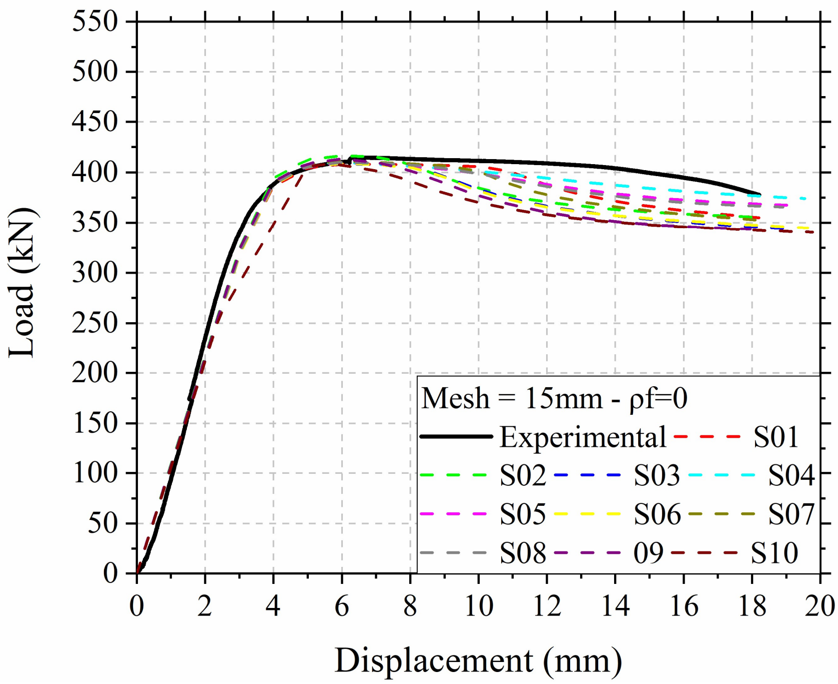

Figure B. 7– Corroded steel grade 50; mesh =10; $\rho_f = 0$

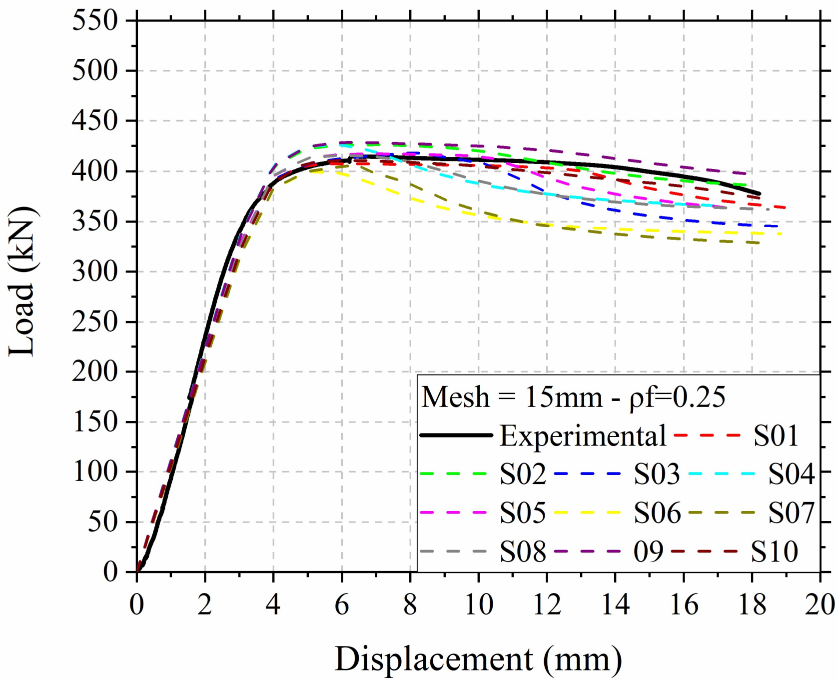

Figure B. 8– Corroded steel grade 50; mesh =10; $\rho_f = 0$

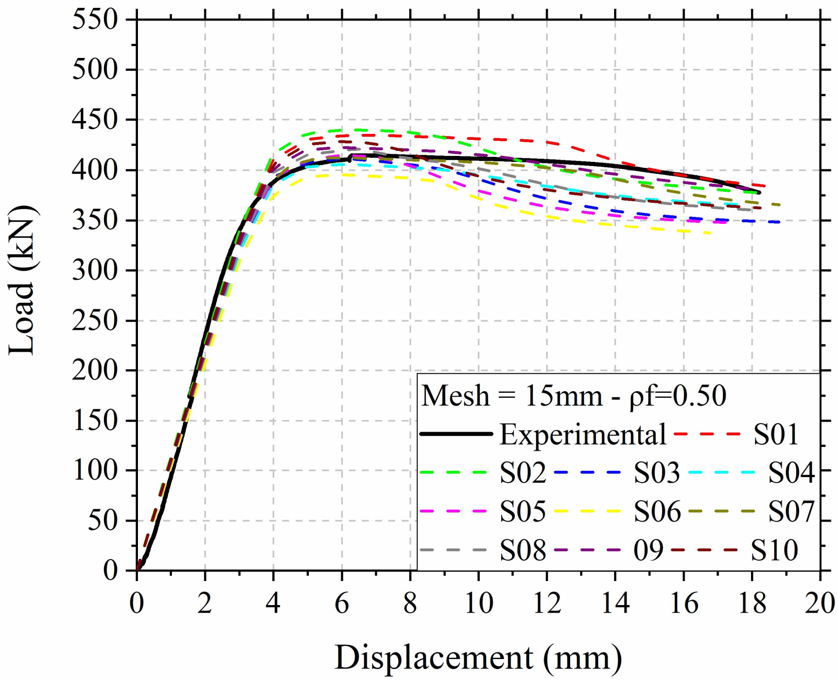

Figure B. 9– Corroded steel grade 50; mesh =10; $\rho_f = 0$

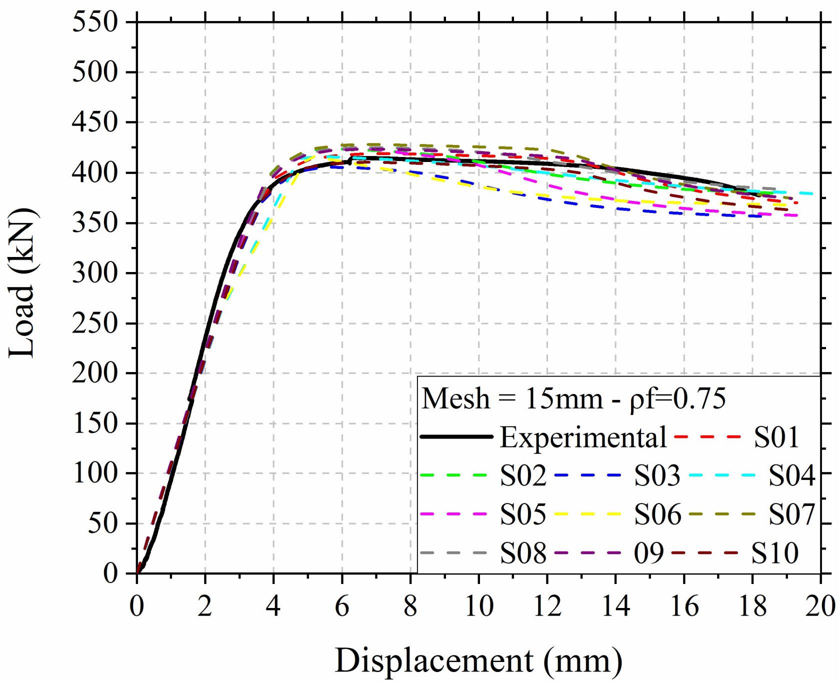

Figure B. 10– Corroded steel grade 50; mesh =15; $\rho_f = 1.0$

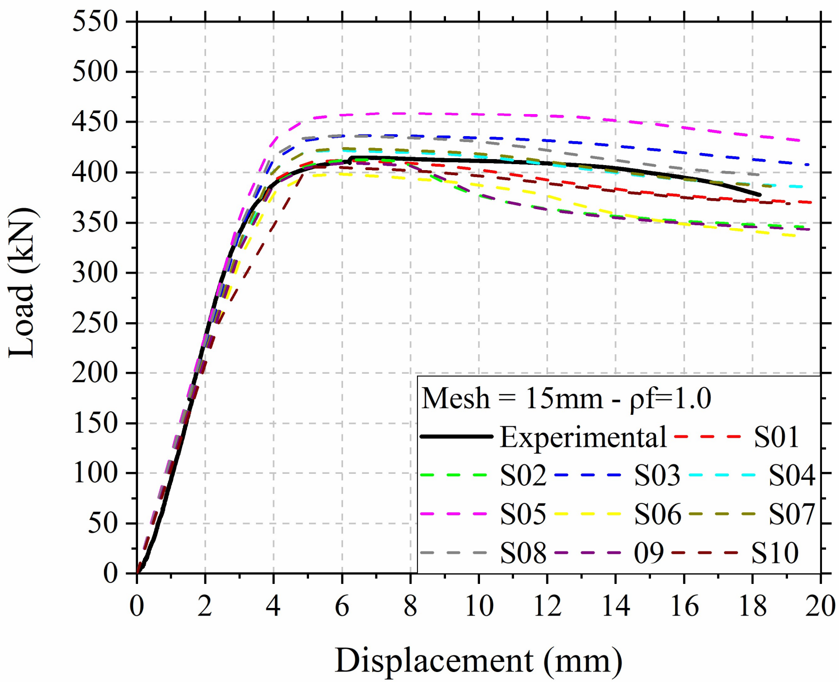

Figure B. 11– Corroded steel grade 50; mesh =20; $\rho_f = 0$

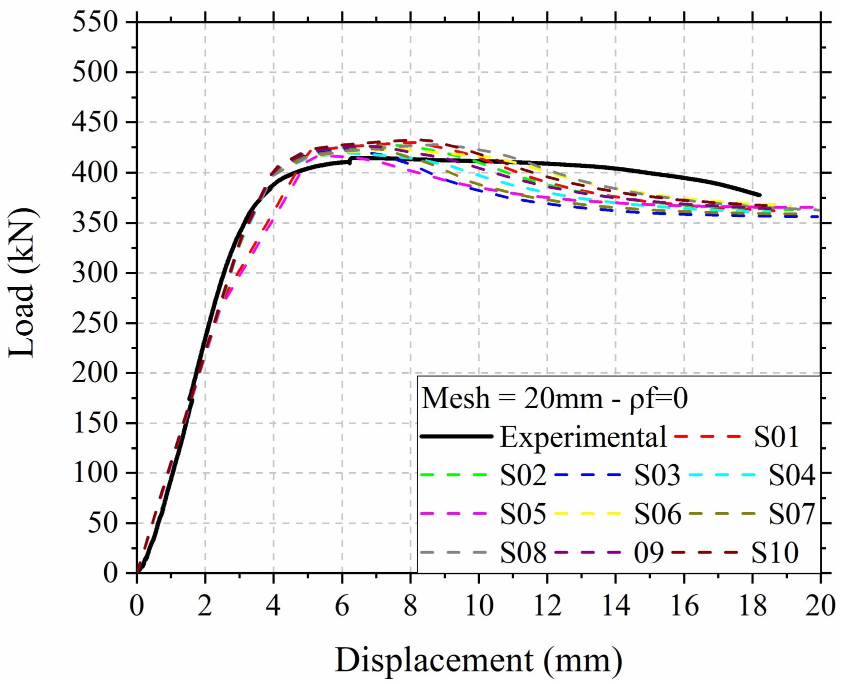

Figure B. 12– Corroded steel grade 50; mesh =20; $\rho_f = 0.25$

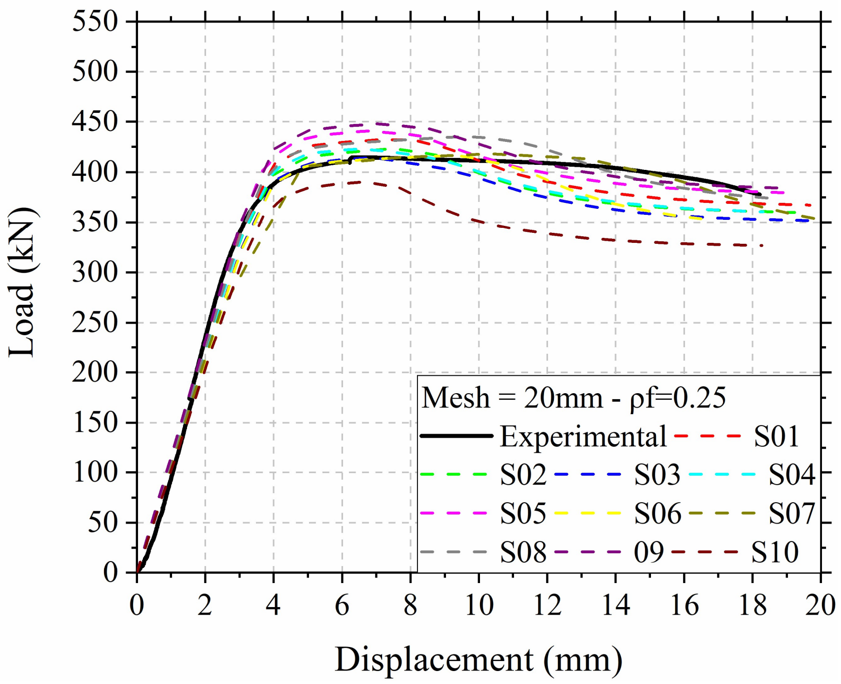

Figure B. 13 – Corroded steel grade 50; mesh =20; $\rho_f = 0.50$

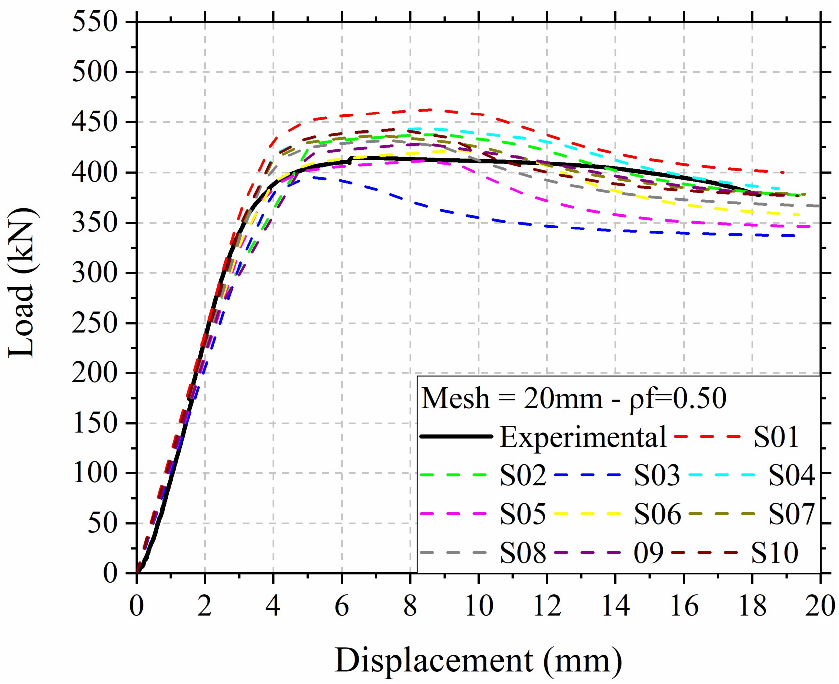

Figure B. 14 – Corroded steel grade 50; mesh =20; $\rho_f = 0.75$

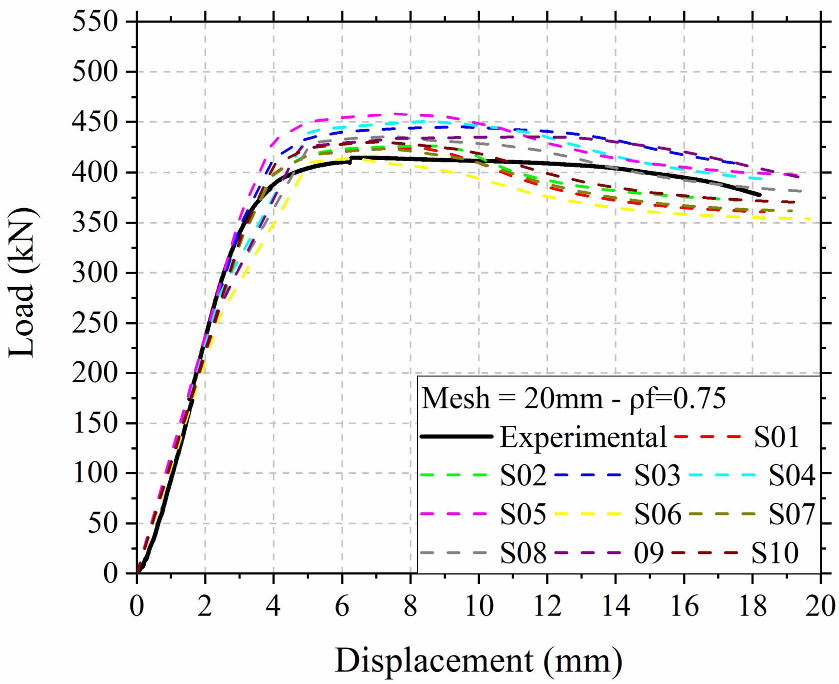

Figure B. 15 – Corroded steel grade 50; mesh =20; $\rho_f = 1.0$

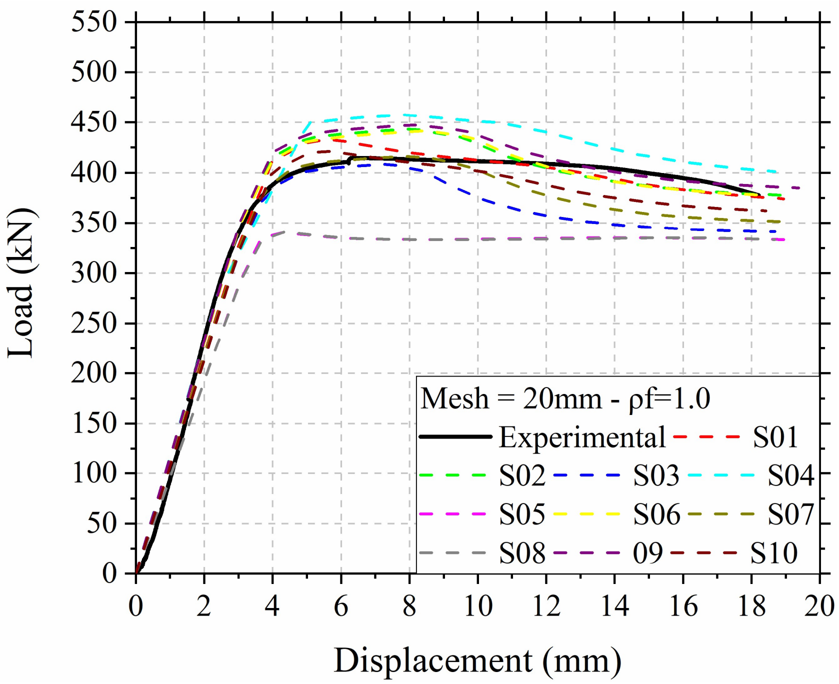

Figure B. 16 – Corroded steel grade 60; mesh =10; $\rho_f = 0.0$

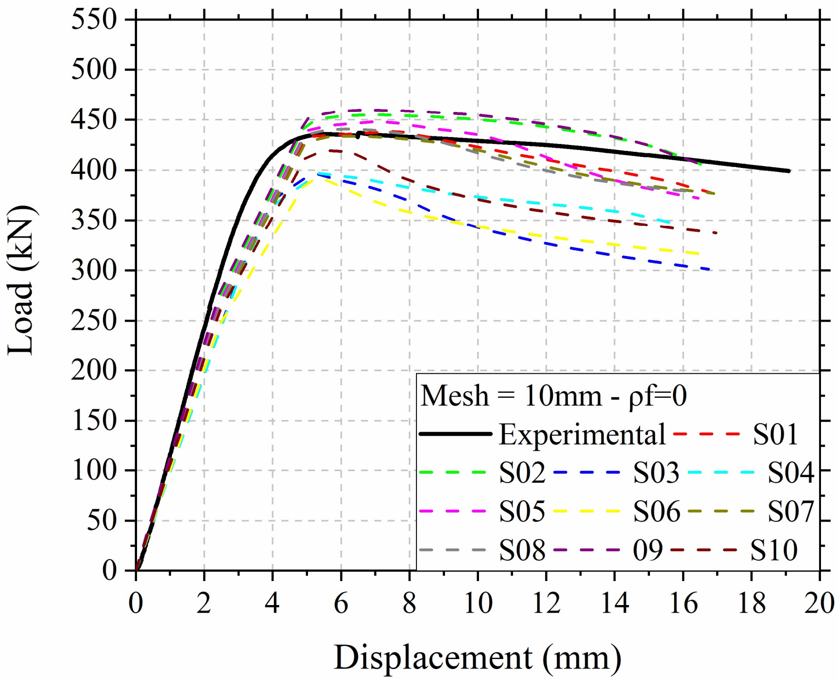

Figure B. 17 – Corroded steel grade 60; mesh =10; $\rho_f = 0.25$

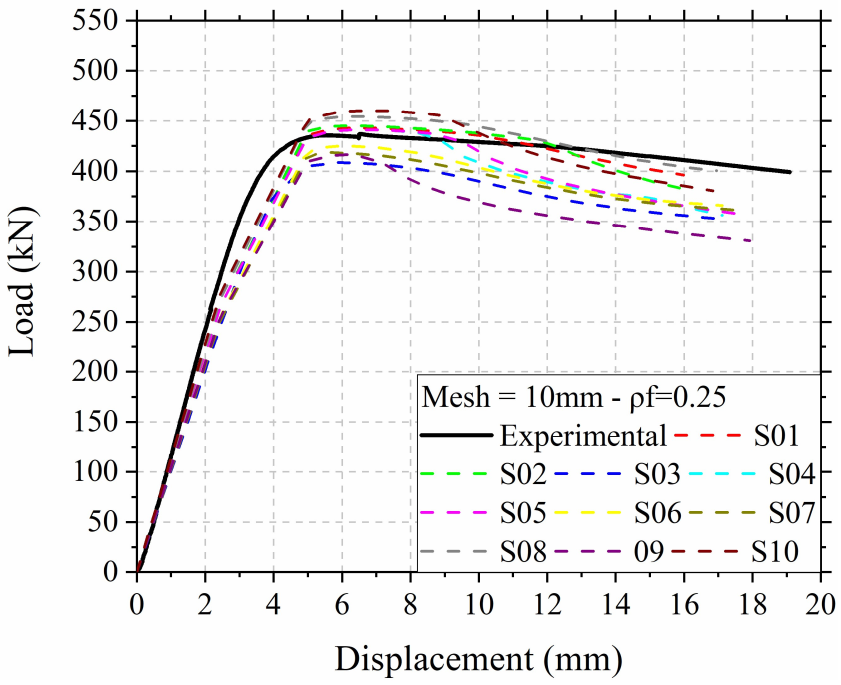

Figure B. 18 – Corroded steel grade 60; mesh =10; $\rho_f = 0.50$

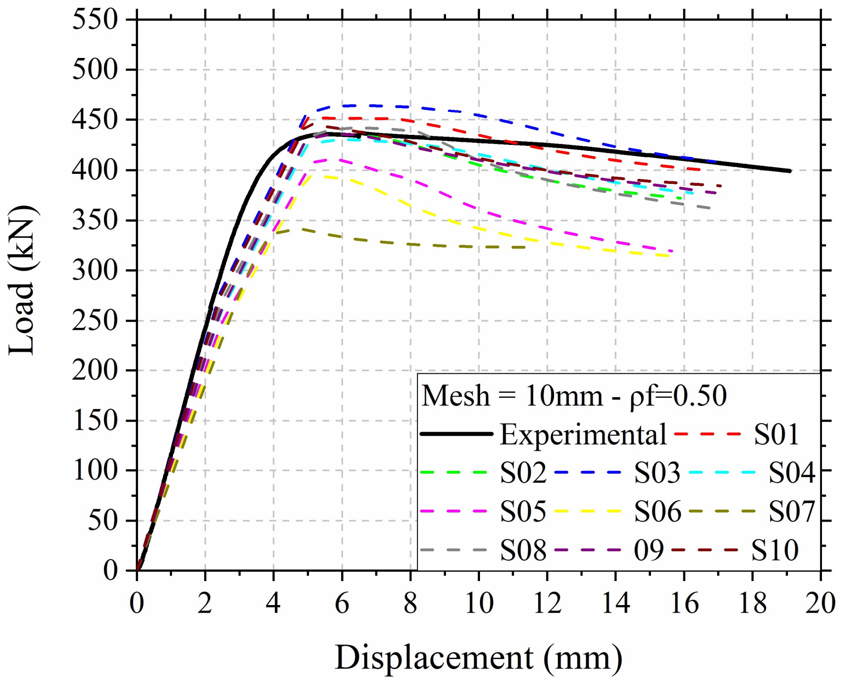

Figure B. 19 – Corroded steel grade 60; mesh =10; $\rho_f = 0.75$

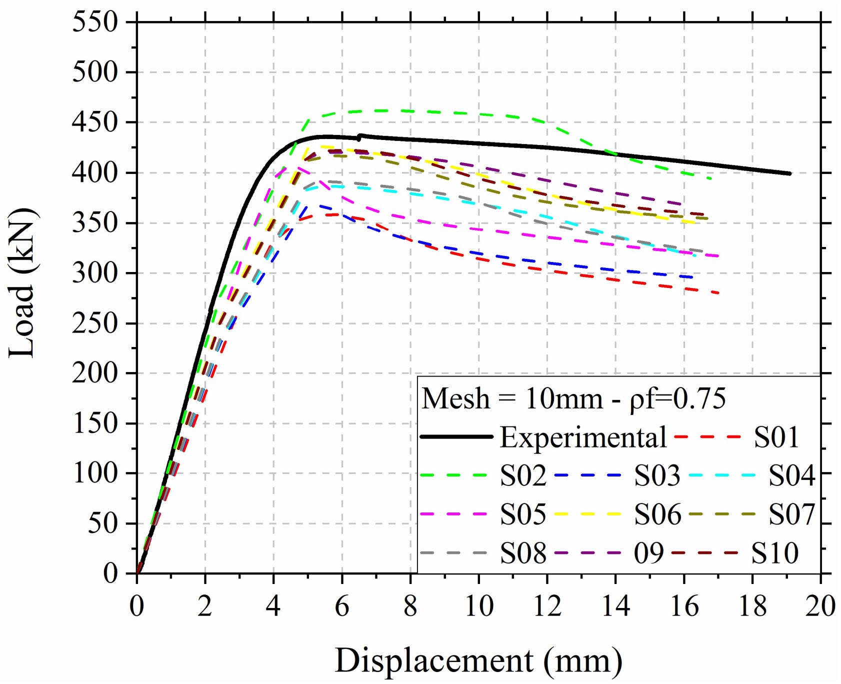

Figure B. 20 – Corroded steel grade 60; mesh =10; $\rho_f = 1.0$

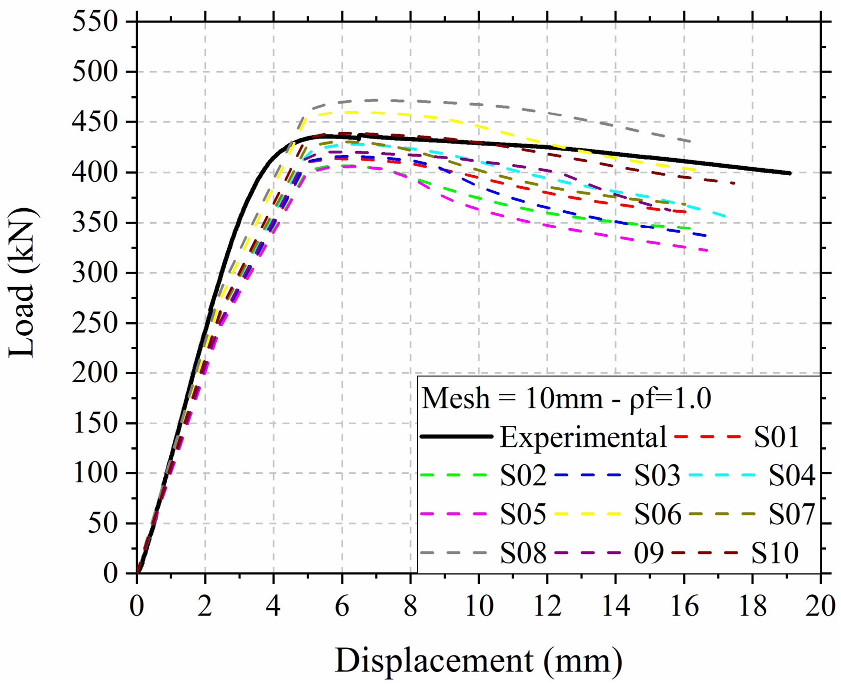

Figure B. 21 – Corroded steel grade 60; mesh =15; $\rho_f = 0.0$

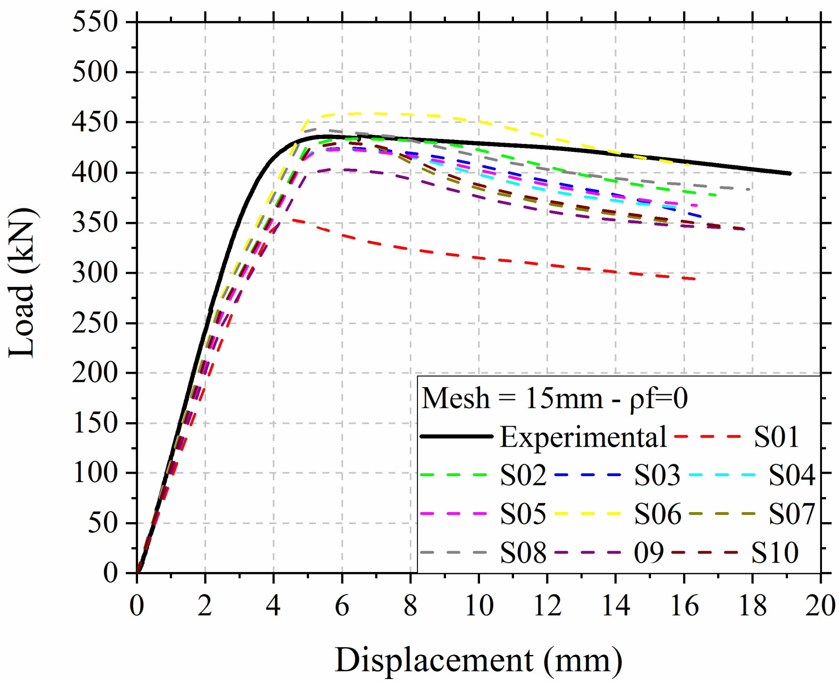

Figure B. 22 – Corroded steel grade 60; mesh =15; $\rho_f = 0.25$

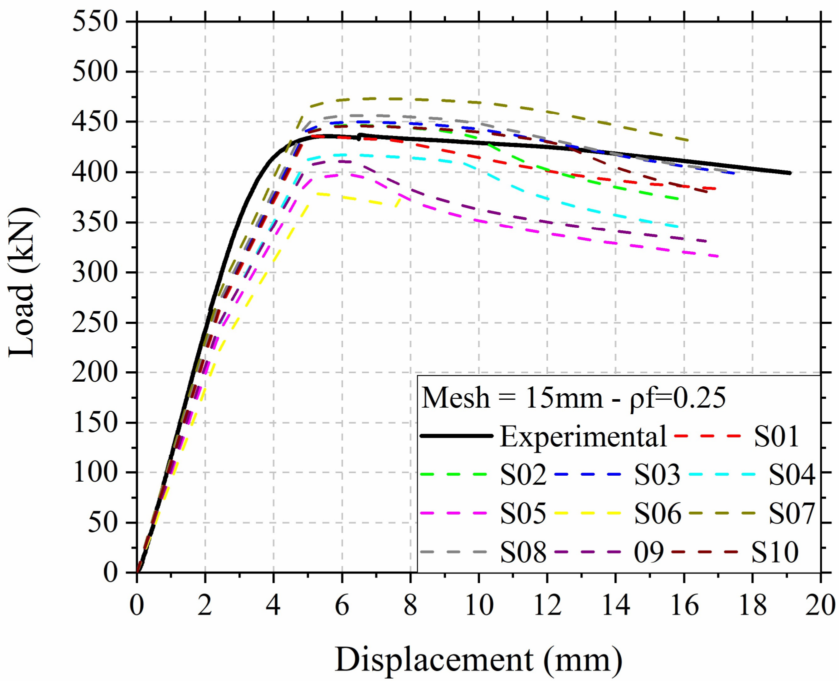

Figure B. 23 – Corroded steel grade 60; mesh =15; $\rho_f = 0.50$

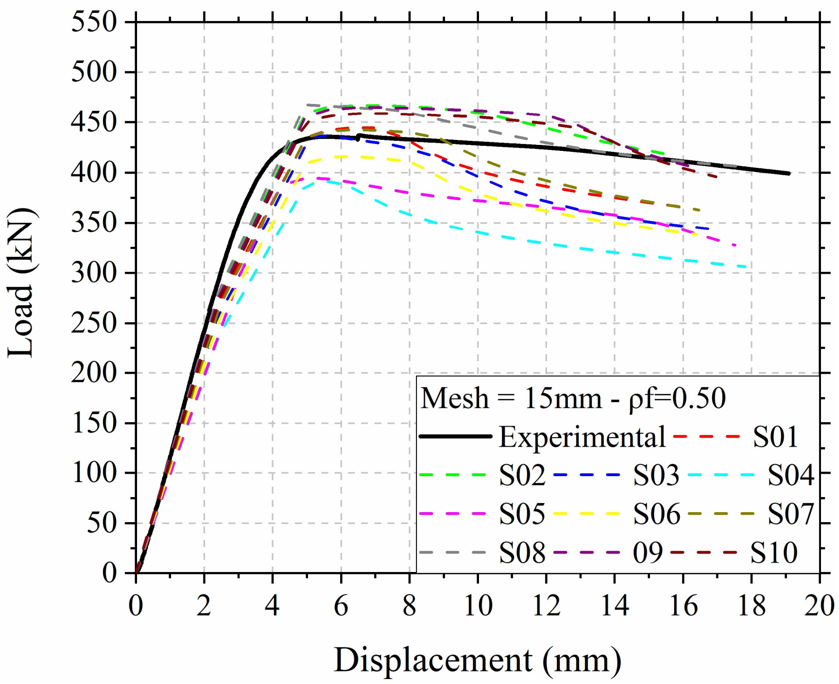

Figure B. 24 – Corroded steel grade 60; mesh =15; $\rho_f = 0.75$

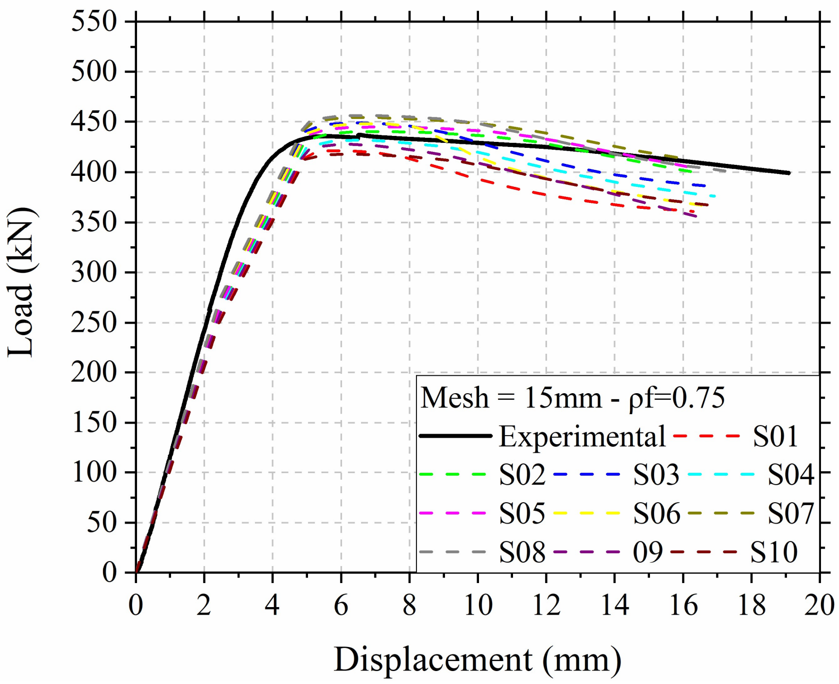

Figure B. 25 – Corroded steel grade 60; mesh =15; $\rho_f = 1.0$

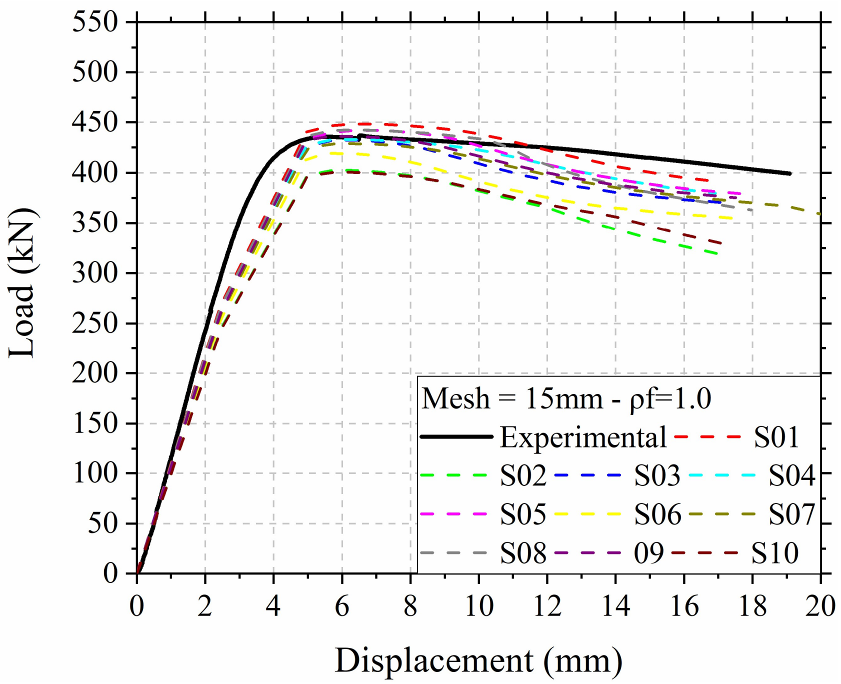

Figure B. 26 – Corroded steel grade 60; mesh =20; $\rho_f = 0.0$

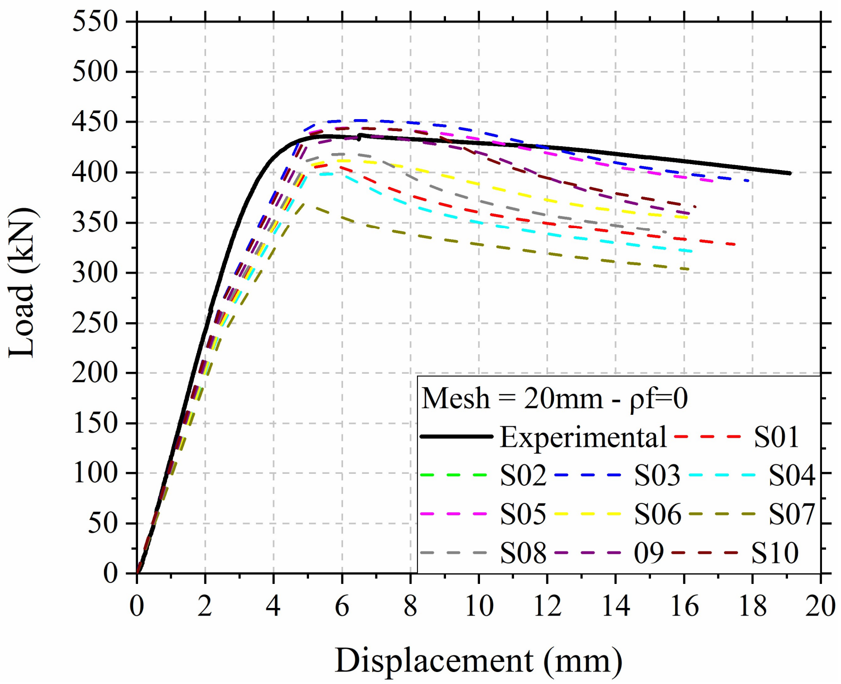

Figure B. 27 – Corroded steel grade 60; mesh =20; $\rho_f = 0.25$

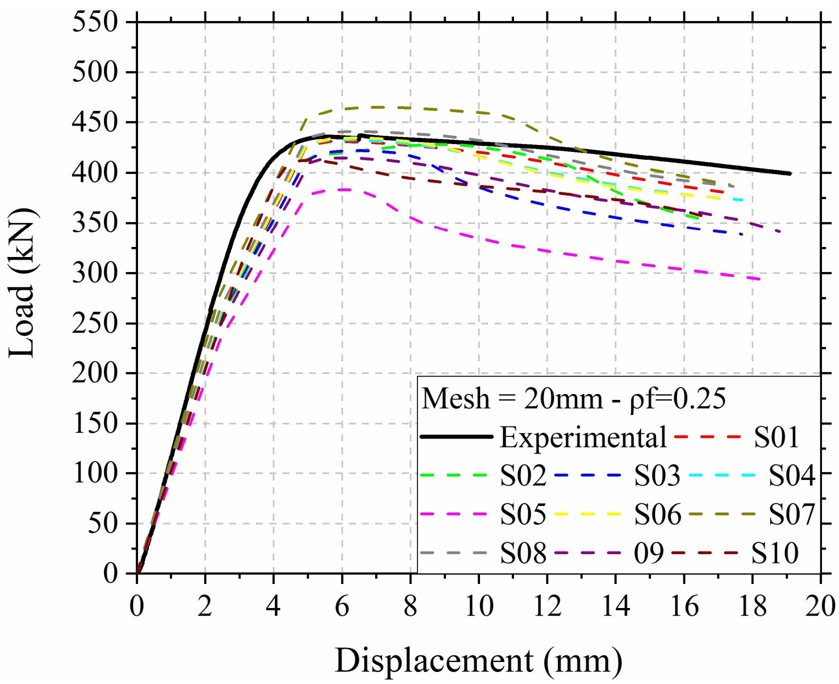

Figure B. 28 – Corroded steel grade 60; mesh =20; $\rho_f = 0.50$

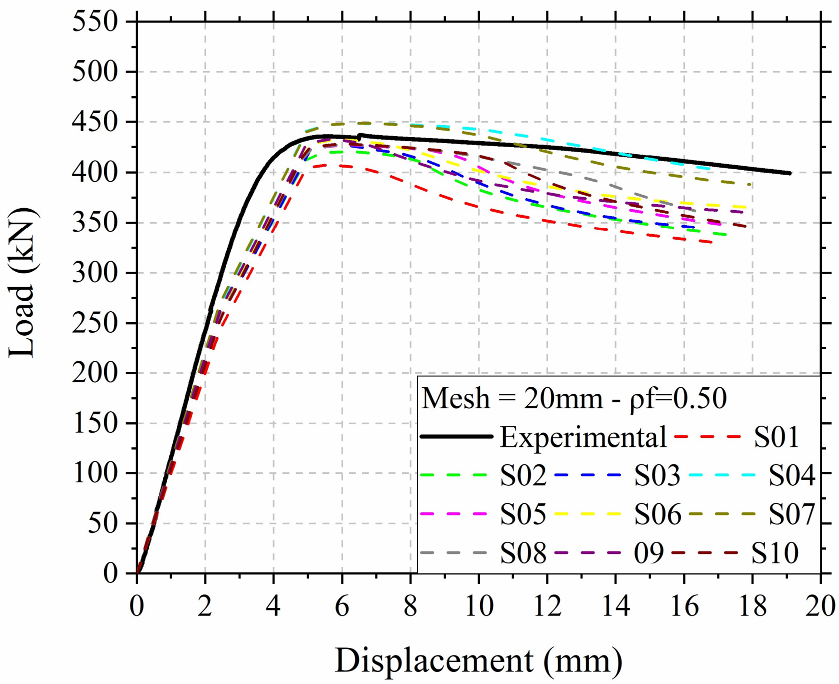

Figure B. 29 – Corroded steel grade 60; mesh =20; $\rho_f = 0.75$

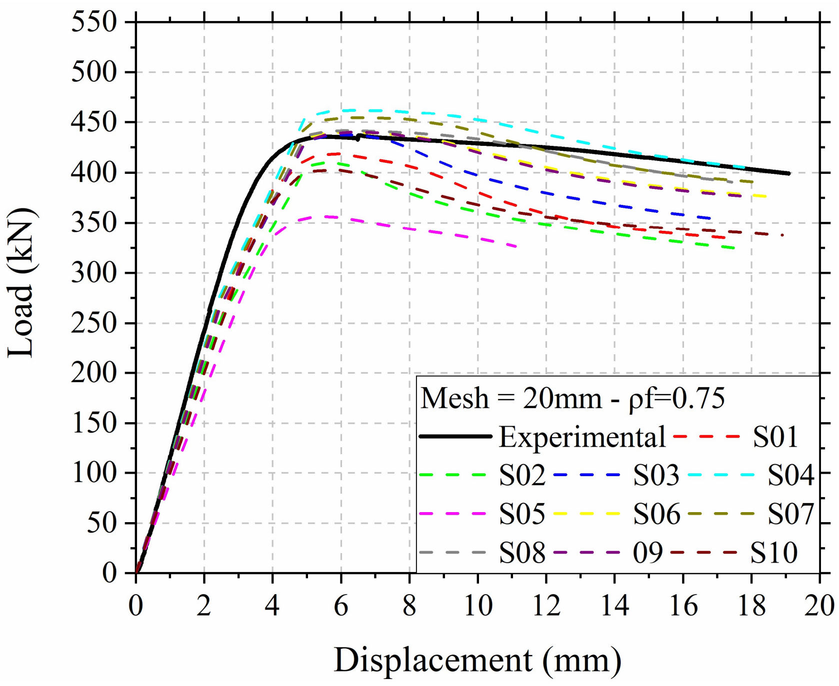

Figure B. 30 – Corroded steel grade 60; mesh =20; $\rho_f = 1.0$